UNIVERSITY OF THESSALY

POLYTECHNIC SCHOOL

DEPARTMENT OF MECHANICAL ENGINEERING

LABORATORY OF MATERIALS

Diploma Thesis

“Thermodynamic and Kinetic Study of Intercritical Annealing of DP1000 Steel”

By

Prevedas Konstadinos

Supervisor:

Dr. Helen Kamoutsi

Submitted for the Partial Fulfillment of the requirements for

the degree of Diploma in Mechanical Engineering

Certified by the members of the Thesis Committee:

First Examiner (Supervisor)
Dr. Helen Kamoutsi
Lab Teaching Staff
Department of Mechanical Engineering
University of Thessaly

Second Examiner
Dr. Gregory. N. Haidemenopoulos
Professor of Physical Metallurgy
Department of Mechanical Engineering
University of Thessaly

Third Examiner
Dr. Nikolaos Aravas
Professor of Computational Mechanics of Structures
Department of Mechanical Engineering
University of Thessaly

Table of Contents

Table of Figures

Table of Tables

Acknowledgements

This project was accomplished in the scope of the partial fulfillment of the requirements for the degree of Diploma in Mechanical Engineering at University of Thessaly.

I would first like to express my sincere appreciation to my supervisor Dr. Helen Kamoutsi, without her persistent help, the goal of this project would not have been realized.

Further, I am particularly grateful to Professor Gregory N Haidemenopoulos and professor Nikolaos Aravas for accepting to take part in the three-member evaluation committee of my Diploma Thesis.

I would also like to express my gratitude to my parents, Nikolaos and Katerina, for their continuous support throughout the course of my studies.

Abstract

The purpose of the present study was the development and implementation of a model, combining a thermodynamic and kinetics computational framework, in order to determine the most desirable processing path for the production of Dual-phase steels with advanced mechanical properties. In order to validate the developed model, results from experiments of intercritical annealing and quenching for DP1000 steel performed by G. C. Nanas and presented in his Undergraduate Thesis [1].To that end, two different models were applied. The use of ThermoCalc software resulted in the phase diagram and in the percentages of alloy elements, that were then introduced into the DICTRA software to simulate the intercritical annealing process. Thus, the results for the austenite volume fraction and the concentration profiles of the alloying elements were obtained. The volume fraction of martensite and retained austenite, as well as the element's concentration in martensite, were calculated as a function of heat treatment time and temperature. In order to perform this simulation, the appropriate code was used in the MATLAB software, incorporating the Barbier and Koistinen-Marburger models. Finally, processing maps were developed in terms of Intercritical annealing temperature and time. These maps make it possible to select the most appropriate heat treatment conditions, in order to achieve the required microstructure (phase fractions) and strength (martensite carbon content).

Chapter 1 Introduction

Description of the problem

In the last few decades, the automotive industry has been developing the materials used to optimize the combination of cost and safety. This involves the use of materials that are characterized by high mechanical properties - they have both high durability and high plasticity capacity and can be easily manufactured to keep costs low. The combination of these needs has led automakers to use high-strength steels (AHSS - Advanced High Strength Steels). The most common material in this industry is DP - Dual Phase. This class of steels also includes DP1000 steels, whose microstructure consists of ferrite and martensite, thus achieving the desired properties. Ferrite is the factor that determines the plasticity of the material and martensite is the factor that determines the durability of the material. Bearing in mind the features of this steel, it is an ideal material for use in car impact zones as it contains high absorption energy. The challenge, therefore, is to develop industrially relevant processing routes that will lead to the desired properties with a minimum of variation. The processing routes for cold-rolled and annealed dual phase involve reheating the steel into the intercritical region, where an austenite/ferrite mixture is formed. For dual-phase steels, cooling to room temperature produces a microstructure consisting of ferrite and martensite. The cooling path and composition of these steels must be carefully optimized to minimize transformation back to ferrite or the pearlite and bainite reactions. This is usually facilitated by alloy additions such as Mn, Mo, or Cr and by employing the optimum heat treatment. In the present work, two different models were developed combining a thermodynamic and kinetics computational framework, in order to determine the most desirable processing path for the production of Dual-phase steels with advanced mechanical properties. The experimental results from G. C. Nanas [1] were used for the validation of the two models. For the 1st Model (γ-α Model) a planar cell, with the size of 5 μm, was initially comprised of a ferrite region with a smaller region of austenite attached to it, that was allowed to grow during the annealing process. The initial size of each region resulted from the equilibrium calculation. For the 2nd Model ($\gamma_{\gamma+cem}$-α Model) that was used to describe the microstructural evolution during IA and subsequent quenching of DP 1000 steel, the conditions calculating the initial microstructure of the model were chosen in the three-phase area. The initial microstructure consisted of mostly ferrite, cementite and a small amount of austenite. The region of austenite in this model incorporates both the volume fraction, as well as, the chemical composition of the newly formed austenite and remaining cementite. For the 2nd Model ($\gamma_{\gamma+cem}$-α Model) a planar cell, with the size of 40 μm was considered for the kinetics simulation. The output of each kinetic simulation is a series of concentration profiles, as well as the position of interface at frequent time intervals, which are then implemented in a MATLAB routine consisting of the Barbier and the Koistinen-Marburger [35] semi empirical models in order to determine the M_S profile and the transformation fraction profiles. The results that were obtained were calculated as a function of heat treatment time and temperature. In order to achieve the required microstructure and strength, processing maps that make it possible to select the most appropriate heat treatment conditions were developed.

Thesis objective

In view of the above considerations, present study was the development and implementation of a model, combining a thermodynamic and kinetics computational framework, in order to determine the

most desirable processing path for the production of Dual-phase steels with advanced mechanical properties. For the purpose of this study two different models applied.

The thesis objectives are therefore the following:

1. To establish a link between the experimental results performed G.C. Nanas [1] and the thermodynamic and kinetic calculations that were produced in the current study.

2. to select the most appropriate heat treatment conditions, in order to achieve the required microstructure (phase fractions) and strength (martensite carbon content) with the help of processing maps.

Thesis methodology

Research was focused on Cold Rolled (CR) Dual Phase (DP) steel with grade 700Y980T. The simulation procedures involved the following actions:

1) Analysis

2) Simulation

3) Validation

4) Mapping

5) Optimization

Thesis outline

The thesis outline is as follows

Chapter 1 - Introduction

Chapter 2 - Bibliographic Review

Chapter 3 - Methodology

Chapter 4 - Validation of modeling process

Chapter 5 - Results

Chapter 6 - conclusions

Chapter 2 Bibliographic Review

Nowadays, automotive industry is accelerating towards a new era, where it must keep up with societal demands. This can be translated as a demand for transportation vehicles and transportation equipment in general to be lighter, which will lead to less fuel consumptions and smaller contribution to greenhouse effect, as well as the manufacture of vehicles that will provide a greater degree of safety. DP steels are low-alloy steels composed of ferritic matrix containing 10-25 % volume of martensite. Ferrite makes them ductile and martensite, which is built in pockets, gives very high tensile strength, in the case of DP1000 steels the σ_{uts} can reach a value of 1000 MPa [2, 3]. Another typical feature of DP1000 steels is their low yield point. Thus, the combination of the advantages mentioned above and the low yield point leads to good dynamic performance, good weldability and cold formability. For these reasons, DP steels are suitable for side member parts, cross members and other complex structural parts. Additionally, one of the most important characteristics of DP steels is their high energy absorbing ability that renders them suitable for crash related parts. This is a result of their binary (ferrite-martensite) microstructure. More specifically, a continuous annealing process is typically applied in order to take a homogeneous dual phase (DP) steel microstructure with well-dispersed martensite islands and fine primary recrystallized ferrite. This process comprises reheating of the first ferrite-bainite or cold-rolled ferrite-pearlite microstructure into the range of IA (intercritical annealing) or fast austenitic annealing. The next step is quenching below the martensite start temperature. Cold rolling, hot rolling and heat treatment are very critical steps that strongly affect the evolution of the microstructure. Recrystallization, recovery, and phase transformations are the mechanisms that complete the IA treatment in Dual Phase steels. The annealing time and temperature, the heating rate and the cooling rate are factors that affect the degree of interaction among the aforementioned phenomena [4-17].

The creation of a ferrite matrix with martensite islands consists the final annealing procedure for DP steels and can be achieved through two different processes. The first process which will lead to transformation of austenite fraction into martensite, consists of holding the material in an austenite-ferrite region. After that, quenching and holding at temperatures slightly below the martensite start temperature follows [18, 19].

Another way to obtain martensite is to quench from fully austenitic region, so that most of the undercooled austenite forms ferrite and the remaining transforms into martensite. Elimination of pearlite and bainite is possible by small additions of Chromium (Cr) and Manganese (Mn). The most common mechanism is phase transformation or recrystallization, depending on the annealing temperature, time, and the preceding cold-rolling reduction [4, 7, 9, 13].

A study conducted by Peranio et al. [5] about the effect of heating rate for a Dual Phase steel (DP steel) alloyed with 0.147-wt% C, 0.403-wt% Si, and 1.868-wt% Mn. A significant increase in hardness was observed for the case of cold-rolled sheets that were rapidly heated. On the other hand, a flat decrease in hardness was the result of longer annealing times [4, 5, 7, 9, 12, 13]. What is more, heat treatments performed near the Ac3 temperature lead to recrystallization and phase transformation at the same time. [4, 5, 20-22]. Additionally, the resulting mechanical properties, the texture and the developments of microstructure prevail by phase transformation over recrystallization effects. New equal ferrite grains, with slight in-grain orientation gradients, and martensite are formatted by Phase transformation. Moreover, high annealing temperatures affect the inherited through-thickness texture inhomogeneity. The combination of high annealing temperatures and short annealing times results in large reduction of the inherited through-thickness texture inhomogeneity, or even in complete elimination of it. An important difference between high and low IA temperatures is that in

the first case the ferrite-martensite band structure in the center of the sheet discloses stronger percolation. Microstructure, when submitted to annealing temperatures in the austenitic zone has a more homogeneous distribution of ferrite-martensite. On the other hand, when specimens are subjected to heat treatment at lower temperatures ferrite recrystallization predominates, while the inherited through-thickness texture, microstructure heterogeneity and resulting mechanical gradients, are maintained to some extent. Depending on time, rate, heating temperature and composition, the above phenomena can happen successively or simultaneously. Particularly, at intermediate heating rates, complex interactions between the following, nucleation, diffusion, growth, and transformation phenomena can take place.[12, 23, 24]

What is more, it has been reported that for various types of cold-rolled steels and subsequently for intercritical annealed Dual-Phase steels, there is a relation among recrystallization and phase transformation.[4, 5, 9, 13]. The impact of the driving force, heating rate, temperature, and holding time on the microstructure of the Dual-Phase steel and hardness for a steel with the following alloy: 0.147-wt% C, 0.403-wt% Si, and 1.868-wt% Mn, was studied by Peranio et al [4, 5]. At relatively low IA temperatures up to 740^{o}C and for annealing at temperatures within the range of ferritic zone recovery and recrystallization predominated. At this range of temperature, with increasing annealing temperature and heating rate, the recrystallization time was reduced. Smaller times were observed for the incubation and recrystallization at the surface, rather than at the center of the sheets. This is a result of the larger deformation in the near-surface regions and the strong ferrite-fiber texture components in the sheet center. Furthermore, partial recrystallization occurred in the center and recrystallization at the surface at 740◦C annealing temperatures. With an increase at heating rates, the volume fraction of recrystallized ferrite increases. In most Dual-Phase steels, temperatures above (700–710) ◦C are the starting point for phase transformation and above (840–860) ◦C pure austenite prevails. These temperatures vary depending on the content of Mn and C. [4, 5]

An increase in annealing temperature will lead to smaller incubation time for phase transformation. While at low IA temperatures, in the preceding cold-rolled material, Martensite and ferrite exhibit equal special distribution like ferrite and pearlite, at austenitic temperatures, new ferrite grains with difference in texture and low orientation gradients form. This observation results from a microstructure memory effect due to pearlite regions undergoing phase transformation before ferrite.

As far as austenite nucleation during intercritical annealing is concerned, two different scenarios are typically discussed.[24]

The former concerns the austenite formation at interfaces of ferrite-cementite within the pearlite colonies. The latter pertains to the nucleation at ferrite-ferrite grain boundaries. Pearlite, due to the availability of carbon from cementite, is often the starting area of nucleation of austenite. Thus, at the expanse of the pearlite and afterwards the surrounding ferrite grows, with a very fast rate, the newly formed austenite. Carbon diffusion inside the austenite is usually the main factor that limits the growth of austenite during this process. Pearlitic regions, due to their surplus of C (carbon) leads to a faster transformation for the austenite zones that nucleate at the pearlite than for those formed at ferrite grain boundaries. For ferritic-pearlitic microstructures, in the case of austenite nuclei that form at boundaries lacking direct contact with a source of carbon, such as ferrite-ferrite grain boundaries, austenite nuclei, in order to support the austenite formation at the moving austenite-ferrite inter-face, requires carbon diffusion from the carbon-rich areas through the ferrite matrix. If the initial microstructure is ferritic-bainitic, faster austenite formation is taking place due to higher dispersion of carbon sources that typically appear. At high intercritical annealing temperatures, the austenite transformation that takes place is critically dependent on the following two factors. The first one is the annealing temperature and the second is the dispersion of the carbon sources. On the other hand, as

mentioned earlier, at low temperatures recrystallization and the recovery of ferrite prevail. Another way to reflect this process is the observation of the mechanical properties of the material after quenching. More explicitly, carbon content increases the hardness of the martensite. Diffusion in sheets that have been annealed at high temperatures leads to a carbon distribution that is more homogeneous and thus, the average carbon content within the martensite reduces.

Cellular automata (CA), Monte Carlo (MC), and phase field methods are microstructure-based transformation models that were used in different studies in an attempt to separate the individual metallurgical processes such as recrystallization, diffusion, recovery and phase transformation occurring during heat treatment of DP steels [25]. During annealing of a cold-rolled Dual-Phase steel, the austenite formation from a ferrite-pearlite starting microstructure was described by a phase field model developed by Rudnizki et al. [12]. This approach neglected the interaction between recrystallization and phase transformation since the microstructure that was used for the simulation was already recrystallized. Another study from Zhu & Militzer [26] focused on the interaction between ferrite recrystallization and austenite formation. High heating rates and cold-rolled pearlite-ferrite microstructure were the starting parameters of that study where, during IA of a DP steel, a phase field model for the simulation of the microstructure evolution was introduced [26]. It should be noted that, for the purposes of Zhu & Militzer's study [26], it was assumed that the phase transformation of austenite-ferrite happens under conditions in which only carbon partitions between the phases through long-range diffusion. A solute drag model was implemented to describe the effect of substitutional alloying elements on the migration of the ferrite-austenite interface during the transformation. Moreover, a 3D CA model was used by Bos et al. [10, 11] during the processing of DP steels in order to describe the through-process microstructure evolution. Simultaneously austenite formation and ferrite recrystallization were considered by both researchers. On the Dual-Phase microstructure, they focused on the influence of individual transformation processes. Okuda et al. [17] developed an MC model to simulate the competition between recrystallization and transformation in several DP microstructures, although the model lacked detailed thermodynamic criteria for the specific driving forces associated with either recrystallization or phase transformation.

The combination of alloy elements, as in all steels, plays an important role in the formation of microstructure and the properties. The effect of each element on the microstructure is not independent but it is affected from the presence of other alloying elements. Both kinetics of phase transformation and thermodynamics are affected by the interaction between the alloy elements and their combining action. Thus, below is presented a sort description as far as the effects for every alloying element is concerned.

Carbon (C): Strength is significantly affected by carbon which is the most important element in steels. An increase in hardness, durability and hardenability can be achieved by increasing the weight percent in C. On the other hand, this will lead to a decrease in weldability and toughness.

Manganese (Mn): Mn creates sulfides (MnS) and has a contribution to the desulphurization of steel, whereas weldability and workability of steels with manganese is also improved. Mn stabilizes the austenite and affects how fast the decomposition is proceeding. Studies have shown that manganese decreases the growth rate of ferrite. This is happening because an increase of Mn affects the thermodynamic stability of austenite to ferrite transformation. Additionally, the separation of Mn atoms on the α/γ phase boundary, caused by an increase in Mn content, leads to a lower Ac3 and Ac1 temperature. As a result, we obtain a steel with enhanced hardenability as the manganese content increases [27].

Silicon (Si): Silicon, along with aluminum, is one of the two elements that are used to deoxidate steels. At the same time Si in the IA (intercritical annealing) temperature quickens the ferrite recrystallization. With the absence of Si in steels, recrystallization and austenitization are proceeding concurrently. On the other hand, in steels that contain Si, ferrite recrystallization appears earlier, and thus the nucleation process constitutes the preferable road for austenite formation. This leads to evenly distributed small islands of martensite within the refined ferrite matrix. Also, after annealing and slow cooling Si cause the formation of a high volume of homogeneous austenite of high hardenability, which leads to an increase in strength of DP steels and to a final structure with high martensite volume [28].

Chapter 3 Methodology

3.1 Material Studied

The material used for this project is a DP steel (Dual Phase Steel) produced by ThyssenKrupp during the RFCS project TOOLKIT [29]. The steel grade that was provided in sheet form, is CR700Y980T-DP commonly known as DP 1000 steel. The chemical composition of the material is displayed below in Table 3.1.

Table 3.1:Chemical composition (%wt) of DP 1000 Steel (CR700Y980T-DP) [29].

Materials	*Fe*	*C*	*Si*	*Mn*	*Cr*	*Mo*	*Cu*	*Al*	*Ti*	*V*	*Nb*	*W*	*Co*
DP1000	95.9	0.07	0.298	2.54	0.682	0.116	0.109	0.036	0.071	0.006	0.07	0.016	0.004

The processing route for DP steels is depicted in Figure 3.1. The starting material is thin cold-rolled sheets with ferrite-pearlite or bainite microstructure Figure 3.2. The material is coiled after hot rolling at temperatures between 530-580°C. After pickling, the hot strip is cold rolled to a degree of 50-60% in order to achieve the targeted grain size after the following annealing stage (average grain size <2μm). The hot dip coated cold strip steel is then processed in a continuous annealing line. The heating rate is in the range between 50 to 70 °C/s. The annealing temperature is bounded between Ac_1 and Ac_3 and the desired amount of austenite during annealing is 50% γ. Typically, the temperatures are between 700°C and 850°C for times in the range of 50-100s.

Martensite is formed through the intercritical annealing (to obtain ferrite-austenite microstructure) and subsequent fast cooling. It is either quenched to room temperature or the quenching is interrupted to galvanize the sheet in hot dip galvanizing lines. The cooling rate in the upper temperature region has to exceed 10°C /s in order to avoid unwanted diffusional transformations. Due to the hot dip process, where the steel strip passes through a pot of liquid Zn, there is a stop of the cooling at about 460°C for about 20s [30, 31]. In Table 3.2 below the bounds for industrial thermal treatment of DP1000 steels are presented, which were provided by TKSE.

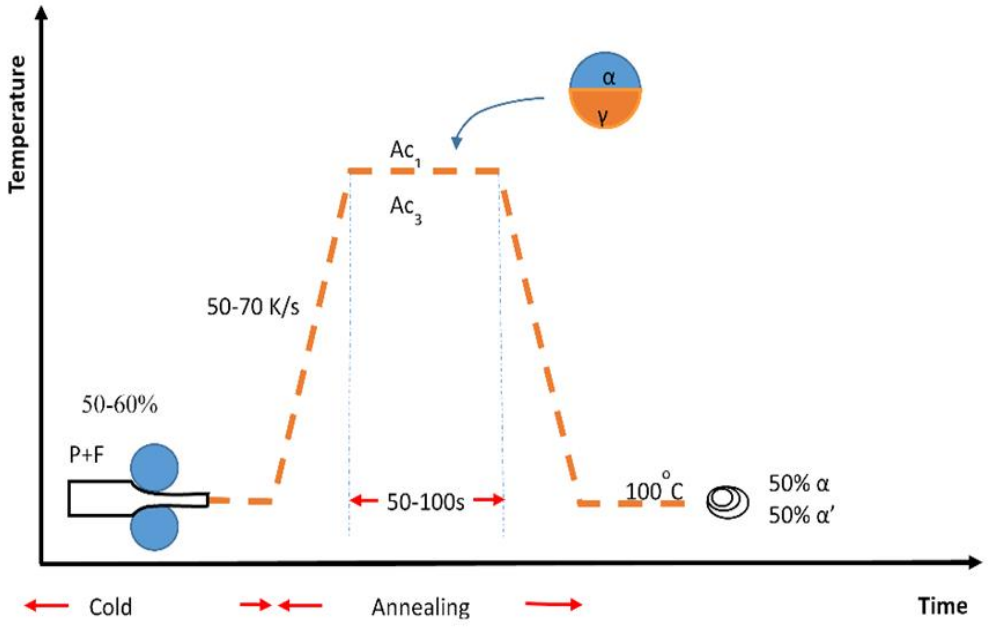

Figure 3.1: Schematic diagram of heat treatment of DP1000 steels.

Table 3.2: Bounds of industrial thermal treatment of DP1000 steels [29].

Process Parameters	Mean Values	Lower Bound	Upper Bound
Hot rolling Temperature [°C]	555	530	580
IA Temperature [°C]	775	700	850
IA Time [sec]	175	50	300
Finishing Temperature [°C]	100	100	100
Heating Rates [$°Cs^{-1}$]	60	50	70
Accelerated Cooling Rates [$°Cs^{-1}$]	55	10	100

The initial microstructure of the as received material is illustrated in Figure 3.2. It consists of 55% ferrite with grain size less than 2μm and 45% martensite with grain size less than 0.5μm.

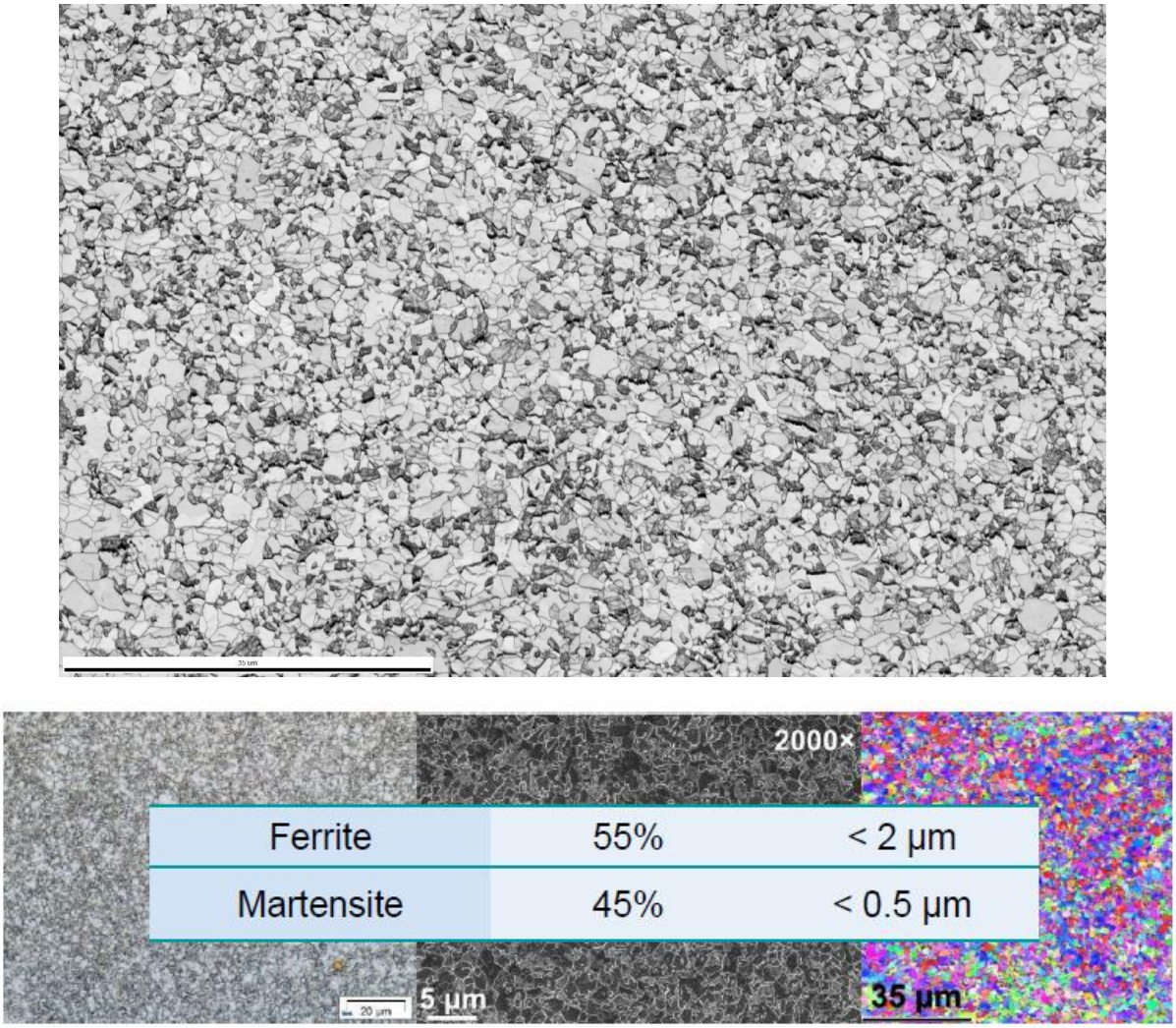

Figure 3.2: Initial microstructure of the as received material (DP1000) [29].

3.2 Simulation tools and methodology

3.2.1 Description of appropriate models for heat treatment simulations

The development of new metallic alloys is traditionally a very tedious process, which involves extensive experimental investigations. The properties of metallic alloys depend on the phases present, their composition and how they are geometrically arranged in the microstructure. Therefore, detailed information about temperature, composition and stability of the different phases as well as phase transformations and phase equilibria are indispensable, not only for modeling and simulation but, more importantly, for the computational design of metallic alloys and their processing.

The process chain model requires preliminary knowledge of the phenomena which take place during the processing routes of DP steels, as well as the process key parameters controlling the microstructural evolution. Several software packages, which allow calculation of phase equilibria as well as other thermodynamic quantities are now commercially available. A more ambitious approach is to combine the thermodynamic calculations with kinetic models, e.g. diffusion calculations and thereby predict the rate of reactions and phase transformations. When computational alloy thermodynamics and kinetics tools are combined with other software packages in the area of mechanics of materials, such as Finite Element codes, inverse analysis programs, or more general multipurpose computational tools such as MATLAB, then it is possible to apply these tools towards the design of alloy compositions and processing [32].

The alloy design process is in general performed in five stages Analysis, Simulation, Validation, Mapping and Optimization

Analysis. It is the first stage in alloy or process design. The aim is to set up the alloy design criteria, including property requirements, on which the design will be based, that can be translated into microstructural requirements. For example, defining appropriate ranges of austenitizing and tempering temperatures.

Simulation. The aim of this stage is to perform a simulation of the microstructural evolution of the alloy and compute microstructure elements and properties. Simulations were performed with computational thermodynamics and kinetics software.

Validation. All simulations involve certain assumptions. It is, therefore, necessary to compare simulation results with available experimental data.

Mapping. The design involves the mapping of the composition space or the process space. Mapping generates a volume of data connecting the microstructural requirements to the alloy composition or process conditions. The alloy design criteria, established in the Analysis stage, are then applied to screen alloy process conditions.

Optimization. In most alloy and process design cases, multiple alloy design criteria are defined. In this case a single optimum solution might not be feasible, since the improvement in one criterion might cause the deterioration of another criterion.

As discussed above, the second stage in the alloy design process is simulation. The relevant simulation toolbox is described in Table 3.3. It involves computational thermodynamics and computational kinetics. A short description of these items is presented below [32].

Table 3.3: Simulation framework for alloy design [32].

Toolbox	**Description**
Computational thermodynamics	CALPHAD approach
	Thermodynamic databases
	Thermo-Calc
Computational kinetics	Multicomponent diffusion
	Mobility databases
	DICTRA

3.2.2 Computational thermodynamics

Computational thermodynamics is based on the CALPHAD approach [33], which involves the development of models for the free energy of the various phases in multiphase and multicomponent alloys. In this way thermodynamic properties in multicomponent systems can be calculated from those of binary or ternary systems. The approach involves critical assessment of thermochemical data and their incorporation into self-consistent databases.

The free energy of a substitutional solid solution is

$$G = G^{o} + G^{id} + G^{xs} + G^{mag} \tag{3-1}$$

where G^{o} is the free energy of the pure components, G^{id} is the ideal or entropic term, G^{xs} is the excess term and G^{mag} is the magnetic term, which is important in systems exhibiting magnetic ordering. For a binary solid solution, the free energy is given by equation

$$G = \sum_i X_i G_i^o + RT \sum_i X_i \ln X_i + \sum_i \sum_{j>i} X_i X_j \Omega_{ij} + G^{mag} \tag{3-2}$$

The above descriptions are implemented in the thermodynamics software Thermo-Calc, which is linked to relevant thermochemical databases to retrieve the required data for the calculations.

3.2.3 Computational kinetics

Computational kinetics is a computational framework for solving problems related to phase transformations in metals and alloys. The discussion will be limited to diffusional transformations, where the transformation is entirely controlled by the diffusion and partition of the alloying elements between the transforming phases [33].

The diffusive flux of an element is proportional to the chemical potential gradient

$$J_i = -M_i c_i \frac{\partial \mu_i}{\partial x}$$

where *M*i is the mobility and *ci* the concentration of component *i*. The above equation can be written as

$$J_i = -M_i c_i \frac{\partial \mu_i}{\partial c_i} \frac{\partial c_i}{\partial x}$$

Comparing with Fick's first law, the diffusion coefficient becomes

$$D_i = M_i c_i \frac{\partial \mu_i}{\partial c_i}$$

and finally takes the form

$$D_i = M_i RT \left(1 + \frac{\partial \ln \gamma_i}{\partial \ln X_i} \right) \quad (3\text{-}3)$$

where γi is the activity coefficient and Xi the atomic fraction of component i. The term in parentheses is the thermodynamic factor.

3.2.4 Martensite formation

During cooling, the austenite-martensite transformation in carbon steels begins at a certain temperature designated as the M_S, temperature and proceeds only upon continuous cooling below this temperature. For the cooling part of the DP control process, a semi empirical MATLAB model is employed. In order to determine the M_S temperature in austenite and the transformation fraction profiles of the final microstructure, the Barbier equation and the Koistinen-Marburger model are incorporated into the MATLAB code.

The raw data produced by Thermo-Calc and DICTRA are processed to determine the fraction of austenite and its stability, as a function of annealing temperature.

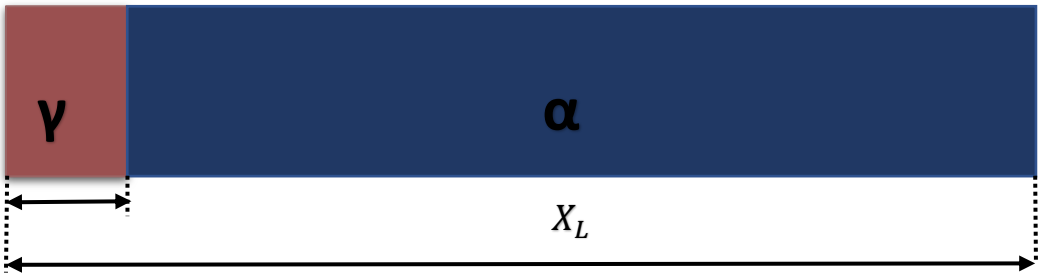

Figure 3.3: Single cell, dual region, planar geometry DICTRA simulation. The cell has a total length of $\boldsymbol{x_L}$ and initially consists of a martensitic region ($\boldsymbol{\alpha}$), with a small austenite region ($\boldsymbol{\gamma}$) of length $\boldsymbol{x_I}$, attached to it.

The output of each simulation is a series of concentration profiles as well as the position of the interface at frequent time intervals. To determine the M_S temperature of the austenite at a given time, as a function of distance in the simulation cell, the Barbier [34] Equation was employed, resulting in an M_S profile.

$$M_s(x,t) = 545 - 601.2\ (1 - \exp(-0.868\ C)) - 34.4\ Mn - 13.7\ Si - 1.4\ Al$$

Then using the Koistinen-Marburger model [35] it is possible to calculate the profile of the transformation fraction, which describes the austenite to martensite transformation kinetics.

$$f_T(x,t) = 1 - \exp\big(-0.011(M_s(x,t) - T_R)\big), \qquad M_S \geq T_R$$

where T_R indicates the ambient temperature of 25°C.

The total volume fraction of martensite $f_M(t)$ at a given time interval is then given by

$$f_M(t) = \frac{f_\gamma(t)}{x_I(t)} \int_0^{x_I(t)} f_T(x,t)\, dx$$

where $f_\gamma(t) = \frac{x_I(t)}{x_L}$ is the total austenite volume fraction, $x_I(t)$ is the position of the interface at a given time and x_L is the total simulation cell length. Finally, the total volume fraction of retained austenite is given by subtracting the fraction of martensite from that of the austenite as

$$f_{\gamma R}(t) = f_\gamma(t) - f_M(t)$$

It is also important to calculate the mean concentration ($\bar{X}_i$) of the elements in ferrite, martensite and retained austenite, as a function of the heat treatment time. The following relation can be used to obtain the mean concentration values from a profile at a given time.

$$\bar{X}_i^{bcc}(t) = \frac{\int_{x_I(t)}^{x_L} X_i(x,t)\, dx}{x_L - x_I(t)}$$

$$\bar{X}_i^{fccR}(t) = \frac{\int_0^{x_I(t)} \big(1 - f_T(x,t)\big)\, X_i(x,t)\, dx}{\int_0^{x_I(t)} \big(1 - f_T(x,t)\big)\, dx}$$

$$\bar{X}_i^{Mart}(t) = \frac{\int_0^{x_I(t)} f_T(x,t)\, X_i(x,t)\, dx}{\int_0^{x_I(t)} f_T(x,t)\, dx}$$

3.2.5 Implementation

For the case of DP steel, the initial microstructure of the alloy before heating in the intercritical annealing (IA) range is an important parameter. The microstructure is either ferrite-perlite or bainite and the initial grain size controls the refinement of the final microstructure. Other controlling parameters are the IA temperature, the holding time of IA as well as the heating and cooling rates of the treatment (Figure 3.4).

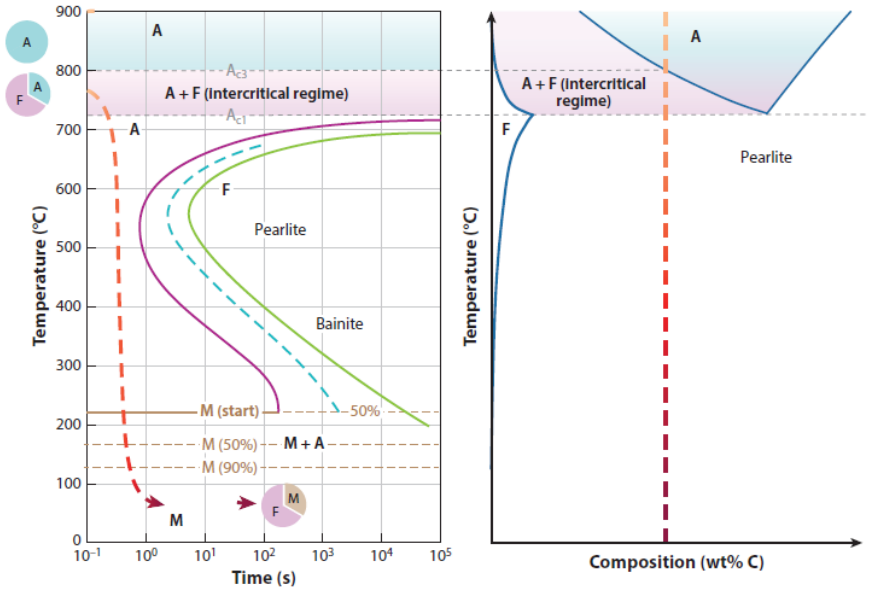

Figure 3.4: Schematic indicating the heat treatment methods used to obtain a DP ferrite-martensite microstructure.

The modelling approach is a combination of thermodynamic and kinetic calculations as well as semi empirical models. The heating part and the intercritical annealing of the control process of the DP steels, were simulated using computational thermodynamics and kinetics. Specifically, thermodynamic calculations were performed using the CHALPAD method with the commercial software Thermo-Calc and the TCFE6 database. Kinetic simulations were carried out using the multi component diffusion module DICTRA, coupled with the TCFE6 thermodynamic and the MOBFE2 kinetic database of Thermo-Calc [33]. For the cooling part of the DP control process, a semi empirical MATLAB model was employed. In order to determine the M_S temperature in austenite and the transformation fraction profiles of the final microstructure, the Barbier equation and the Koistinen-Marburger model were incorporated into the MATLAB code.

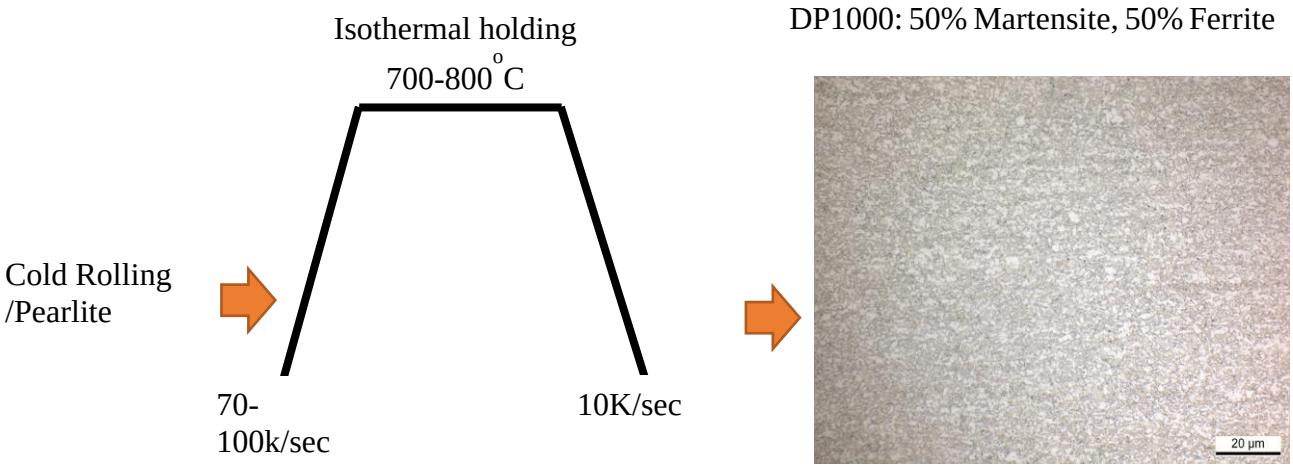

Figure 3.5: Schematic illustration of Heat Treatment of Dual Phase steel and example of resulting microstructure of DP1000 consisting of 50% martensite and 50% ferrite.

For the case of DP 1000 steel studied in the present work, two separate models were used. These models are described in the sections that follow.

3.2.5.1 1st Model: Initial microstructure austenite-ferrite (γ-α Model)

For DP 1000, the evaluation of intercritical annealing bounds as well as the initial microstructure were calculated with Thermo-Calc. The temperature of cementite dissolution and the volume fraction of the equilibrium phases of austenite and ferrite, along with their chemical composition were rendered as the initial conditions for the model (Figure 3.6).

Concerning the kinetic simulations, a single cell, dual region planar diffusion calculation was considered. The material was taken to be ferritic initially, with an initial amount of austenite resulting from the equilibrium conditions mentioned above, that is allowed to grow during isothermal intercritical annealing. Thus, the planar cell was initially comprised of a ferrite region with a smaller region of austenite attached to it, that was allowed to grow during the annealing process, as illustrated in Figure 3.7.

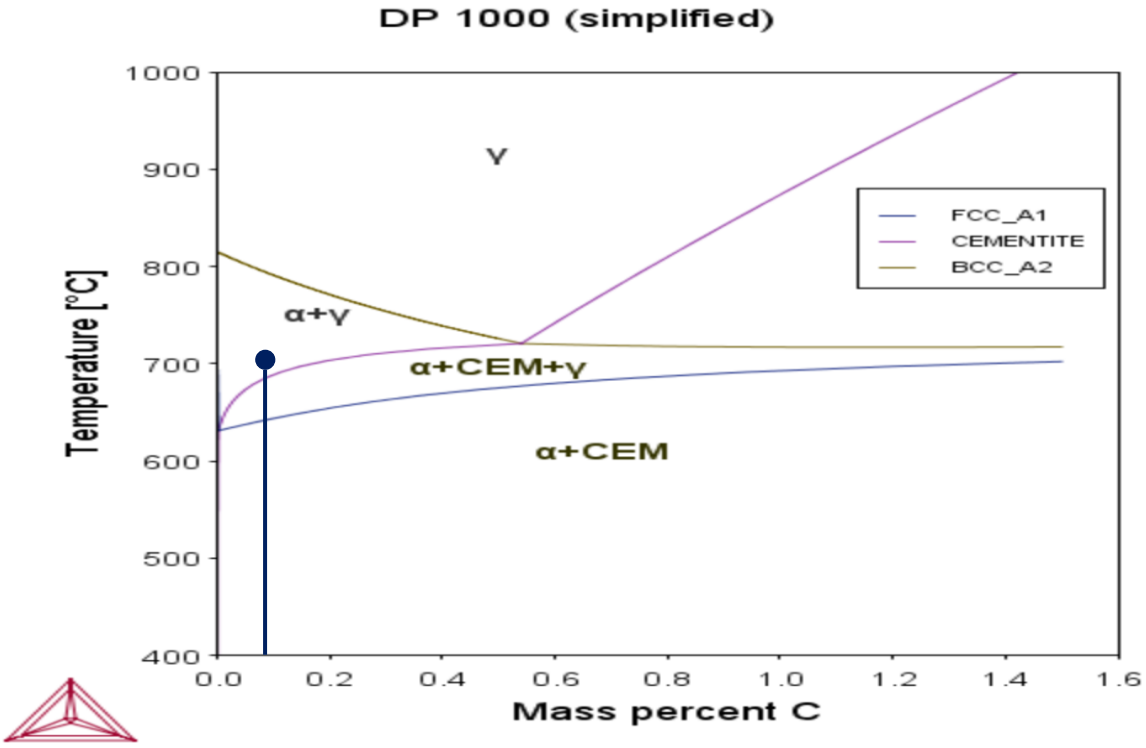

Figure 3.6: Isopleth diagram of DP1000 steel Calculated with THERMOCALC software and TCFE-6 data-base.

The total cell size, the length of the initial austenite region, as well as four parameters regarding the reduction of the activation energy for diffusion, caused by dislocation and grain boundary assisted diffusion, were determined by fitting the DICTRA model to experimental data. In the present study, the initial cell size was assumed 5 μm (Figure 3.7) and the austenite and ferrite regions were evaluated after initial thermodynamic calculations. Next, kinetic simulations were performed for varying IA temperatures 700-800°C.

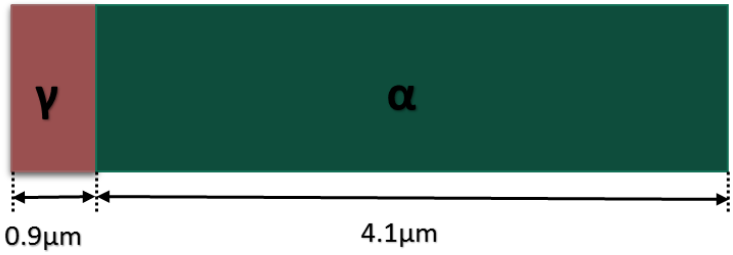

Figure 3.7: Schematic illustration of the DICTRA *γ-α Model* simulation, cell geometry. It consists of a single cell, dual region, and planar geometry. The cell has a total length of $\boldsymbol{x_L}$=5 μm and initially consists of a ferite region ($\boldsymbol{\alpha}$), with a small austenite region ($\boldsymbol{\gamma}$) of length $\boldsymbol{x_l}$ =0.9 μm, attached to the right.

The output of each kinetic simulation is a series of concentration profiles, as well as the position of interface at frequent time intervals, which are then implemented in a MATLAB routine consisting of the Barbier and the Koistinen-Marburger [35] semi empirical models in order to determine the M_S profile and the transformation fraction profiles. The final output are the total volume fraction of martensite $f_M(t)$, the total volume fraction of retained austenite $f_{\gamma R}(t)$ with respect to the interval time, as well as the mean concentration of the elements in ferrite $\bar{X}_i^{bcc}(t)$, martensite $\bar{X}_i^{Mart}(t)$ and retained austenite $\bar{X}_i^{fccR}(t)$ as a function of the heat treatment time.

3.2.5.2 2nd Model: Initial microstructure austenite$_{(\gamma+cem)}$-ferrite ($\gamma_{\gamma+cem}$-α Model)

For the second model used to describe the microstructural evolution during IA and subsequent quenching of DP 1000 steel the conditions calculating the initial microstructure of the model were chosen in the three-phase area of the material's Phase Diagram (Figure 3.8). More specifically the initial microstructure consisted of mostly ferrite, cementite and a small amount of austenite.

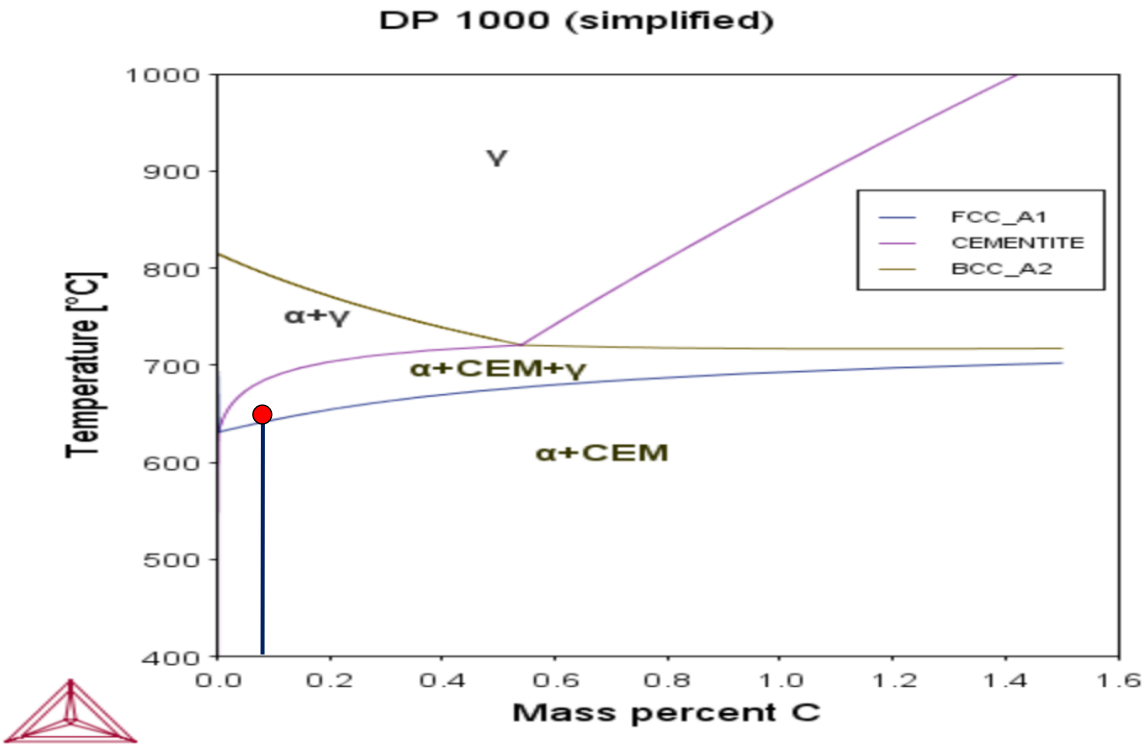

Figure 3.8: Isopleth diagram of DP1000 steel Calculated with THERMOCALC software and TCFE-6 data-base.

The evaluation of the initial microstructure was calculated with Thermo-Calc (Figure 3.8). The temperature of austenite formation, as well as, the volume fraction of the equilibrium phases of austenite, cementite and ferrite, along with their chemical composition were rendered as the initial conditions for the model.

Concerning the kinetic simulations, a single cell, dual region planar diffusion calculation was considered. The material was taken to be ferritic initially, with an initial amount of austenite resulting from the equilibrium conditions mentioned above, that is allowed to grow during isothermal intercritical annealing. Thus, the planar cell was initially comprised of a ferrite region with a very small region of austenite attached to the right. The region of austenite in the model incorporates both the volume fraction, as well as, the chemical composition of the newly formed austenite and remaining cementite Figure 3.9.

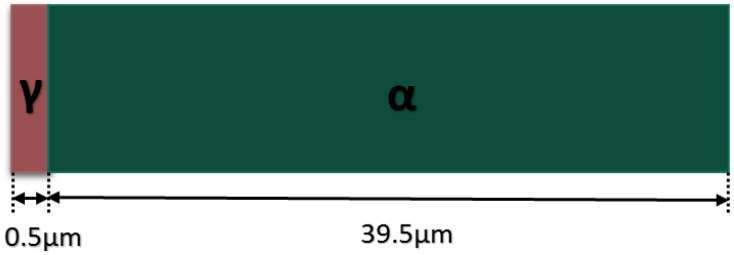

Figure 3.9: Schematic illustration of the DICTRA $\gamma_{\gamma+cem}$-α *Model* simulation, cell geometry. It consists of a single cell, dual region, and planar geometry. The cell has a total length of $\boldsymbol{x_L}$=40 μm and it initially consists of a ferrite region $(\boldsymbol{\alpha})$, with a small austenite region $(\boldsymbol{\gamma})$ of length $\boldsymbol{x_l}$ =0.5 μm, attached to the right.

As mentioned above for the 1st Model, the output of each kinetic simulation is a series of concentration profiles, as well as the position of interface at frequent time intervals, which are then implemented in a MATLAB routine consisting of the Barbier and the Koistinen-Marburger [35] semi empirical models in order to determine the M_S profile and the transformation fraction profiles. The final output are the total volume fraction of martensite $f_M(t)$, the total volume fraction of retained austenite $f_{\gamma R}(t)$ with respect to the interval time, as well as the mean concentration of the elements in ferrite $\bar{X}_i^{bcc}(t)$, martensite $\bar{X}_i^{Mart}(t)$ and retained austenite $\bar{X}_i^{fccR}(t)$ as a function of the heat treatment time.

The total cell size, the length of the initial austenite region, as well as four parameters regarding the reduction of the activation energy for diffusion, caused by dislocation and grain boundary assisted diffusion, were determined by fitting the DICTRA model to published experimental data. In the present study, the initial cell size was assumed 40 μm (Figure 3.9) and the austenite and ferrite regions were evaluated after initial thermodynamic calculations. Next, kinetic simulations were performed for varying IA temperatures 700-800°C.

Chapter 4 Validation of modelling process

4.1 Thermodynamics

The phase diagram that is presented in Figure 4.1 was calculated with Thermo-Calc and TCFE6 database. The chemical composition was taken from Table 3.1. Austenite formation temperature during heating was calculated at 681.87°C (A_{c1}) and the temperature at which the transformation of ferrite to austenite is completed during heating (A_{c3}) was calculated at 803.42°C.

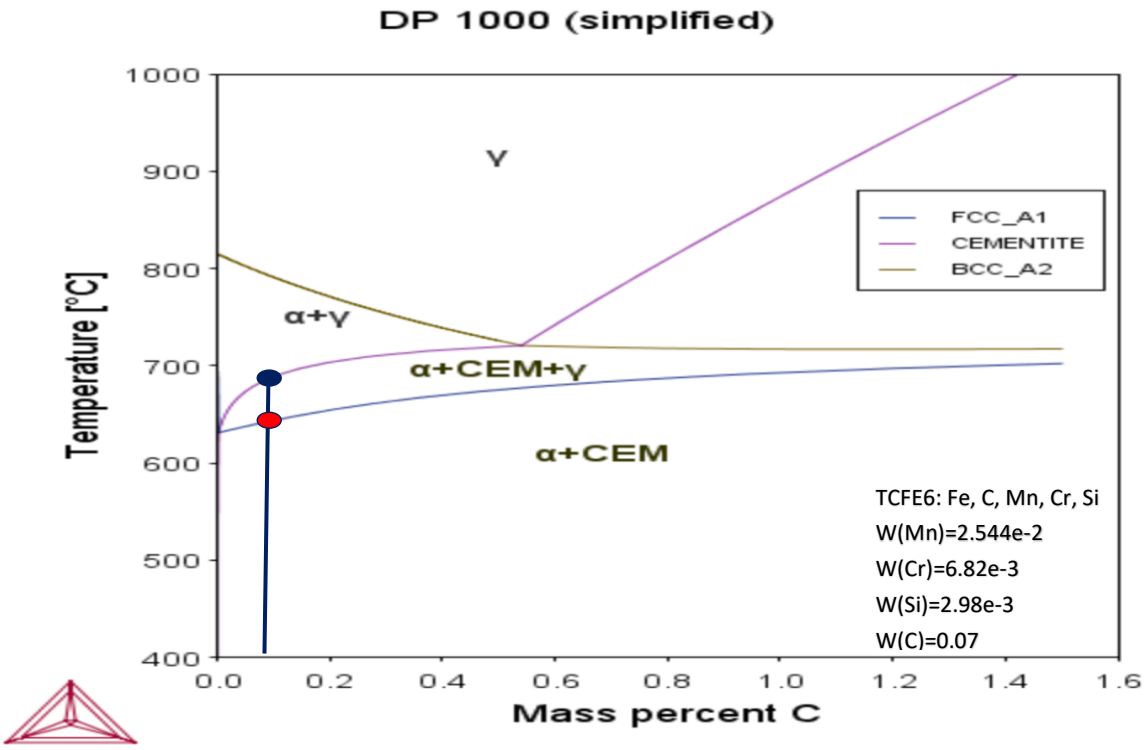

Figure 4.1: Isopleth diagram of DP1000 steel Calculated with THERMOCALC software and TCFE-6 database.

For the 1st Model (α-γ Model) simulation, the results that are illustrated in Table 4.1 were calculated with Thermocalc for a single point equilibrium. The single point equilibrium is denoted with the blue dot in Figure 4.1.

These results were used as starting points in the DICTRA simulation, in order to simulate the IA (intercritical annealing) and subsequently to obtain information about austenite growth, as well as, the partitioning of alloying elements during IA and martensite formation. The equilibrium calculation was performed at 682°C as the blue dot shows in Figure 4.1.

Table 4.1: Volume fraction and mass fraction of phases and alloying elements for 1st Model (γ-α Model)region

Stable phase	Volume fraction	Mass fraction (Fe)	Mass fraction (C)	Mass fraction (Mn)	Mass fraction (Cr)	Mass fraction (Si)
BCC_A2	0.8196	0.9730	4.5e-5	0.0174	0.0060	0.0030
FCC_A1	0.1803	0.9215	0.0036	0.0615	0.0102	0.0029

For the 2nd Model ($\gamma_{\gamma+cem}$-α Model) simulation, the results that are illustrated at Table 4.2 were calculated from a single point equilibrium, that is denoted with the red dot in Figure 4.1. These data were used as initial conditions for the DICTRA simulation. The equilibrium calculation was performed at 642°C as the red dot shows in Figure 4.1

Table 4.2: Volume fraction and mass fraction of phases and alloying elemnts for the 2nd Model ($\gamma_{\gamma+cem}$-α Model).

Stable phase	Volume fraction	Mass fraction (Fe)	Mass fraction (C)	Mass fraction (Mn)	Mass fraction (Cr)	Mass fraction (Si)
BCC_A2	0.987	0.9679	2.19e-5	0.02354	0.00515	0.003
FCC_A1	0.00275	0.8922	0.00295	0.09273	0.00866	0.00336
Cem	0.01025	0.5617	0.06797	0.19638	0.17393	4.7683e-13
FCC+Cem	1.3010	0.63168	0.054206	0.17444	0.13894	7.1146e-4

4.2 Validation of the proposed models

The initial material (in sheet form) was cut in small specimens and subjected to a two-step heat treatment. The step of the heat treatment was performed at 854°C for 30 minutes, 50°C above the beginning of the full austenitic zone, after that, isothermal holding at 550°C for 1 hour followed. Finally, all specimens were air cooled. This treatment led to a ferrite-perlite microstructure. The second step that followed was intercritical annealing. The temperatures that were applied in G. C. Nanas Thesis [1], were 700 °C, 720 °C, 750°C, 760°C, 770°C and 780°C. These temperatures are in between A_{e1} (681,87°C) and A_{e3} (803,42°C). A_{e1} is the temperature that austenite formation begins and A_{e3} is the temperature, that ferrite to austenite transformation is completed during heating. ThermoCalc and TCFE6 thermodynamic database were used to evaluate A_{e1} and A_{e3}. The last step that took place was water quenching, immediately after IA (intercritical annealing). Quenching was performed in order to transform austenite formed during IA to martensite and thus the desired DP1000 microstructure was formed. Finally, metallographic and image analysis were performed. All specimens were grinded with appropriate grinding papers, in order to remove the thermal oxidation film and to create a smoother face. After grinding, two-step polishing with diamond paste and alumina powder followed. Image J software was used for Image analysis.

4.2.1 Validation of the 1st Model (γ-α Model)

Four sets of data were used in order to validate the proposed model. In the work performed by G. C. Nanas [1], the formation of austenite during intercritical annealing of Dual Phase steels was studied by quantitative metallographic investigation.

In that work, intercritical heat treatments of plate specimens at 700°C, 720°C, 750°C and 760°C were performed for times ranging from 30 s to 3600 s. The initial microstructure was ferrite-pearlite. The results of those experiments along with the results of the simulations at 700°C, 720°C, 750°C and 760°C, are presented in Figure 4.2, Figure 4.3, Figure 4.4 and Figure 4.5. The symbols represent the experimental results from G.C. Nanas , while the continuous lines the kinetic calculations with DICTRA software that was used for the simulation of IA and MATLAB software that was used for the simulation of quenching.

About the kinetic model, the initial grain size of the material was considered in the region size used by the model, as well as the initial ferrite perlite microstructure [22]. The initial conditions (initial phase composition) were evaluated using the thermodynamic software THERMOCALC. It was assumed that the perlite fraction of the microstructure, is spontaneously converted into austenite with the exposure to the intercritical annealing temperature. The Table 4.3 depicts the intercritical annealing holding times and temperatures that were used in DICTRA software.

Table 4.3: intercritical annealing holding times and temperatures

Step 1 DICTRA	Time	Step 2 MATLAB
Heating at 700^{o}C	60 min	Quenching
Heating at 720^{o}C	60 min	Quenching
Heating at 750^{o}C	60 min	Quenching
Heating at 760^{o}C	60 min	Quenching

It is evident that simulation results are in good agreement with the experimental data, especially for the case of intercritical annealing at the higher temperatures of 760^{o}C and 750^{o}C. In the case of intercritical annealing at the lower temperatures of 720^{o}C and 700^{o}C, there is a difference for short annealing times, where the simulation predicts slower kinetics than in the case of the experimental data.

Figure 4.2 depicts the simulation and experiment results for the case of intercritical heat treatment at 760^{o}C and Figure 4.3 for 750^{o}C. The symbols represent the experimental results from G.C. Nanas [1], while the continuous lines the kinetic calculations with DICTRA software. For the case of the 1st Model (γ-α Model), we started with a large percentage of austenite as obtained from phase diagram and the model is constructed by assuming initial austenite already formed from pearlite at the onset of the simulation. The result is a deviation from the experimental values with respect to the values obtained from DICTRA, while the simulation model predicts higher amounts of final austenite volume fraction at the end of intercritical annealing the rest experimental values are in good agreement with the simulation results for both 760^{o}C and 750^{o}C.

Similarly, for the case of intercritical annealing at 720^{o}C and 700^{o}C the kinetics for the simulation results deviate from the experimental values for shorter times, while they predict almost same amounts of final austenite volume fraction at the end of inter-critical annealing. The results for 720^{o}C and 700^{o}C are illustrated at Figure 4.4 and Figure 4.5 respectively. The symbols represent the experimental results from G.C. Nanas [1], while the continuous lines the kinetic calculations with DICTRA software.

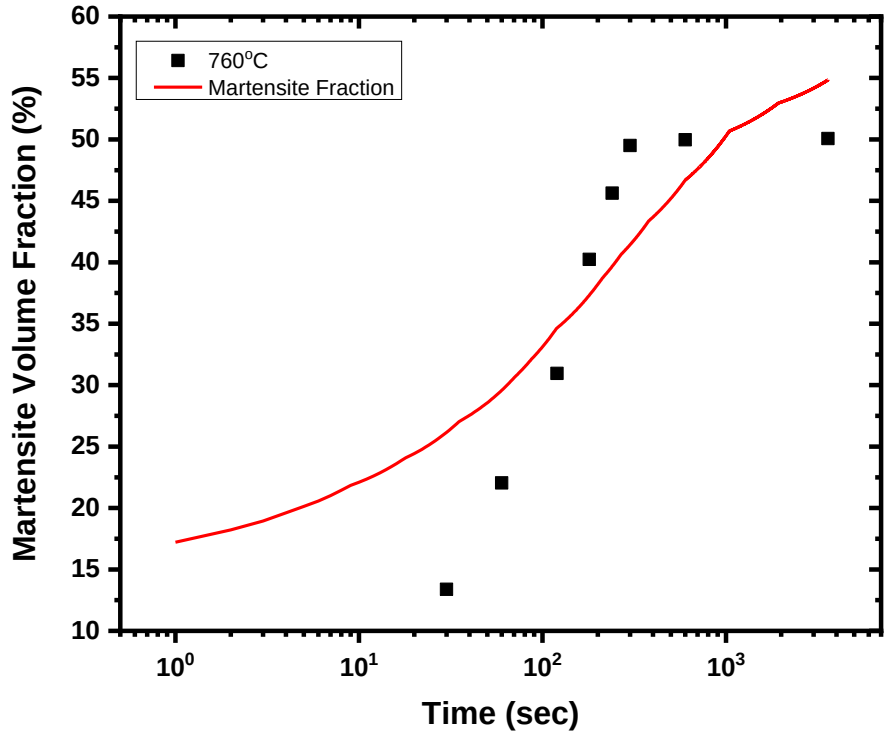

Figure 4.2: Kinetics of austenite formation for intercritical heat treatments at 760°C. Symbols represent the experimental results from G. C. Nanas [1], while the continuous red line the kinetic calculations with DICTRA software.

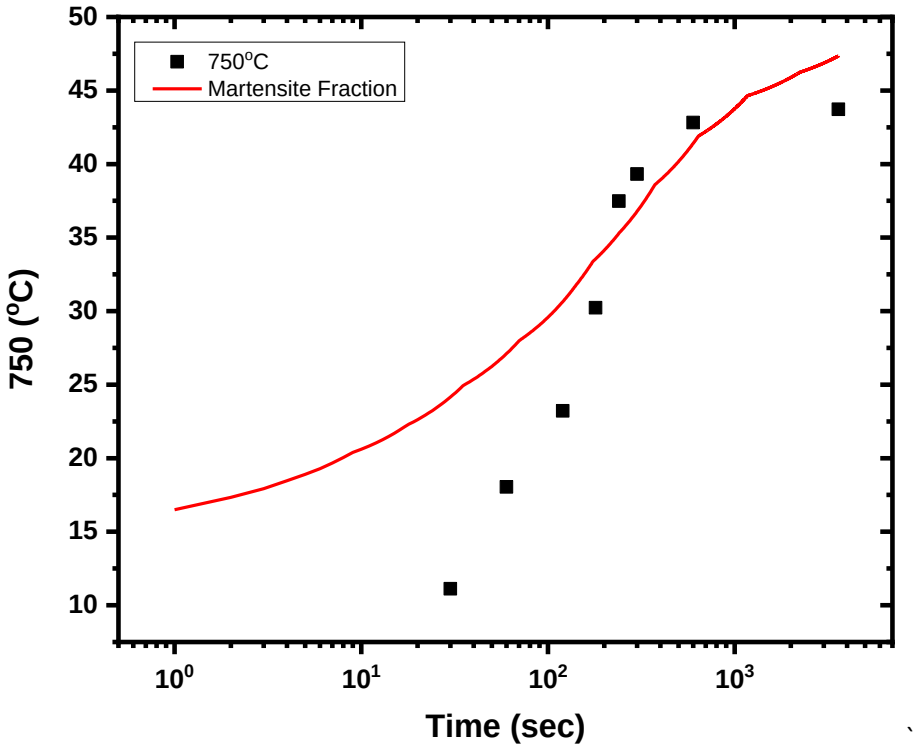

Figure 4.3: Kinetics of austenite formation for intercritical heat treatments at 750°C. Symbols represent the experimental results from G.C. Nanas [1], while the continuous red line the kinetic calculations with DICTRA software.

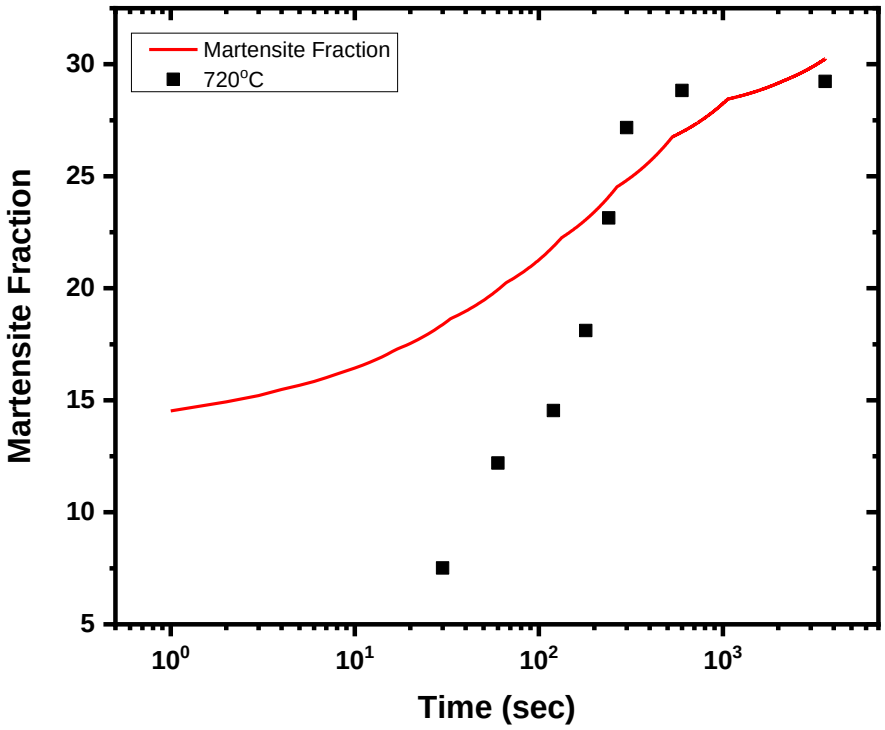

Figure 4.4: Kinetics of austenite formation for intercritical heat treatments at 720°C. Symbols represent the experimental results from G.C. Nanas [1], while the continuous red line the kinetic calculations with DICTRA software.

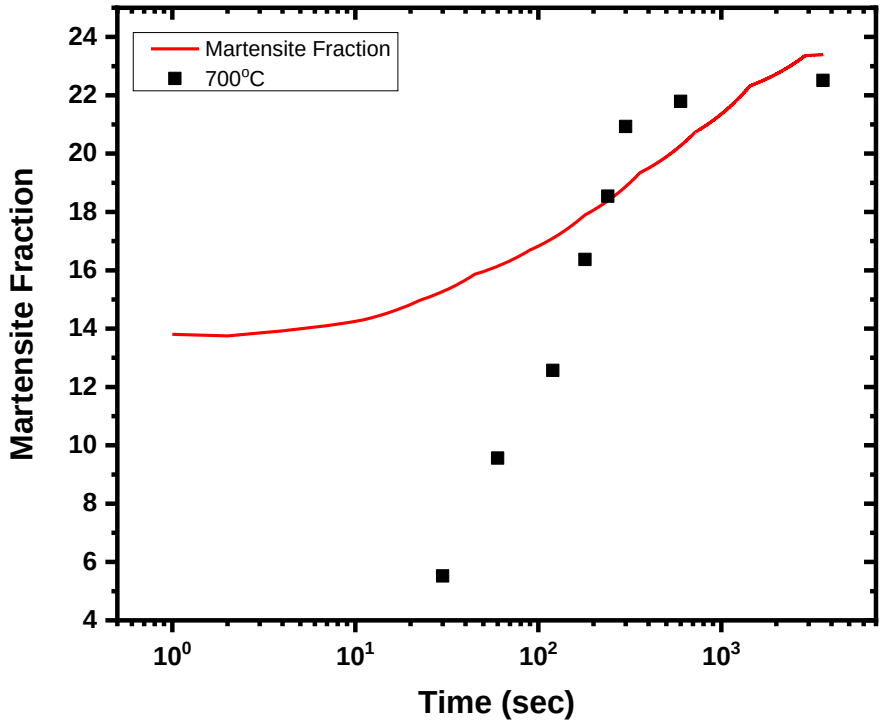

Figure 4.5: Kinetics of austenite formation for intercritical heat treatments at 700°C. Symbols represent the experimental results from G.C. Nanas [1], while the continuous red line the kinetic calculations with DICTRA software.

4.2.2 Validation of the 2nd Model ($\gamma_{\gamma+cem}$-α Model)

Similar to the 1st Model (γ-α Model) simulation, for the 2nd Model ($\gamma_{\gamma+cem}$-α Model) simulation, the same data sets described in paragraph 4.2.1 from the work of G.C. Nanas [1], were used for the validation of the model. The results of those experiments along with the results of the simulations, are presented in Figure 4.6, Figure 4.7, Figure 4.8 and Figure 4.9. The symbols represent the experimental results from G.C. Nanas [1], while the continuous lines the simulation results.

About the kinetic model, the initial grain size of the material was taken into account in the region size used by the model, as well as the initial ferrite perlite microstructure [22]. The initial conditions (initial phase composition) were evaluated using the thermodynamic software THERMOCALC. It was assumed that the perlite fraction of the microstructure, is spontaneously converted into austenite with the exposure to the intercritical annealing temperature. Also, for the 2nd Model ($\gamma_{\gamma+cem}$-α Model) model it was assumed that the initial austenite volume fraction is the sum of austenite and cementite.

For the 2nd Model ($\gamma_{\gamma+cem}$-α Model) simulation, like 1st Model (γ-α Model) simulation, it is evident that the simulation results are in good agreement with the experimental data, especially for the case of intercritical annealing at the higher temperatures of 760°C and 750°C. In the case of intercritical annealing, at the lower temperature of 720°C, there is a difference at shorter times between experimental data and simulation results and for 700°C the difference is at longer times.

Figure 4.6 depicts the simulation and experiment results for the case of intercritical heat treatment at 760°C and Figure 4.7 for 750°C. The symbols represent the experimental results from G.C. Nanas, while the continuous lines the kinetic calculations with DICTRA software. For the case of the 2nd Model ($\gamma_{\gamma+cem}$-α Model), we started with a too small enriched austenite region as obtained from phase diagram and the model is constructed by assuming initial austenite already formed from pearlite at the onset of the simulation. In the 2nd Model ($\gamma_{\gamma+cem}$-α Model), the very small austenite enriched region leads to a very good agreement between simulation and experimental results for shorter time as opposed to the 1st Model (γ-α Model). The experimental values are in good agreement with the simulation results for both 760°C and 750°C. the simulation model predicts slightly lower amounts of final austenite volume fraction at the end of intercritical annealing and subsequently lower amounts of final martensite at the end of quenching.

For the case of intercritical annealing at 720°C the kinetics for the simulation results deviate from the experimental values for shorter times. For longer times they are in good agreement with experimental results, while they predict almost same amounts of final austenite volume fraction at the end of inter-critical annealing. The results for 720°C are illustrated at Figure 4.8. The symbols represent the experimental results from G.C. Nanas, while the continuous lines the kinetic calculations with DICTRA software. Figure 4.9 depicts the results for 700°C. in this case it is notable that there is a good agreement between experimental and simulation results for shorter times. After 120 seconds there is a deviation between experimental and simulation results, while the simulation model predicts lower amounts of final austenite volume fraction at the end of intercritical annealing and subsequently lower amounts of final martensite at the end of quenching.

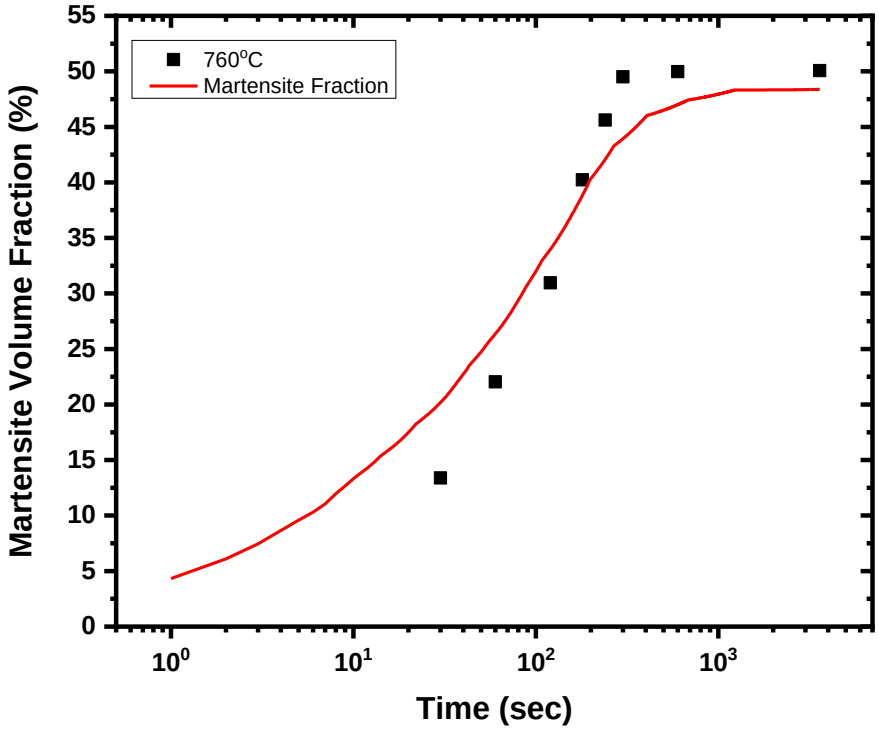

Figure 4.6: Kinetics of austenite formation for intercritical heat treatments at 760°C. Symbols represent the experimental results from G.C. Nanas [1], while the continuous red line the kinetic calculations with DICTRA software.

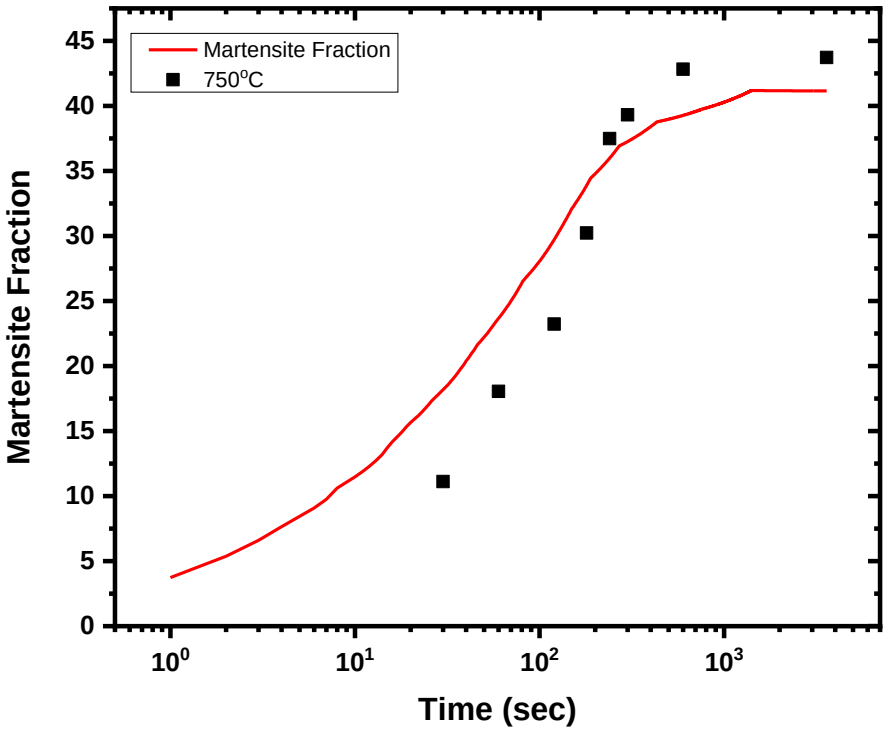

Figure 4.7: Kinetics of austenite formation for intercritical heat treatments at 750°C. Symbols represent the experimental results from G.C. Nanas [1], while the continuous red line the kinetic calculations with DICTRA software.

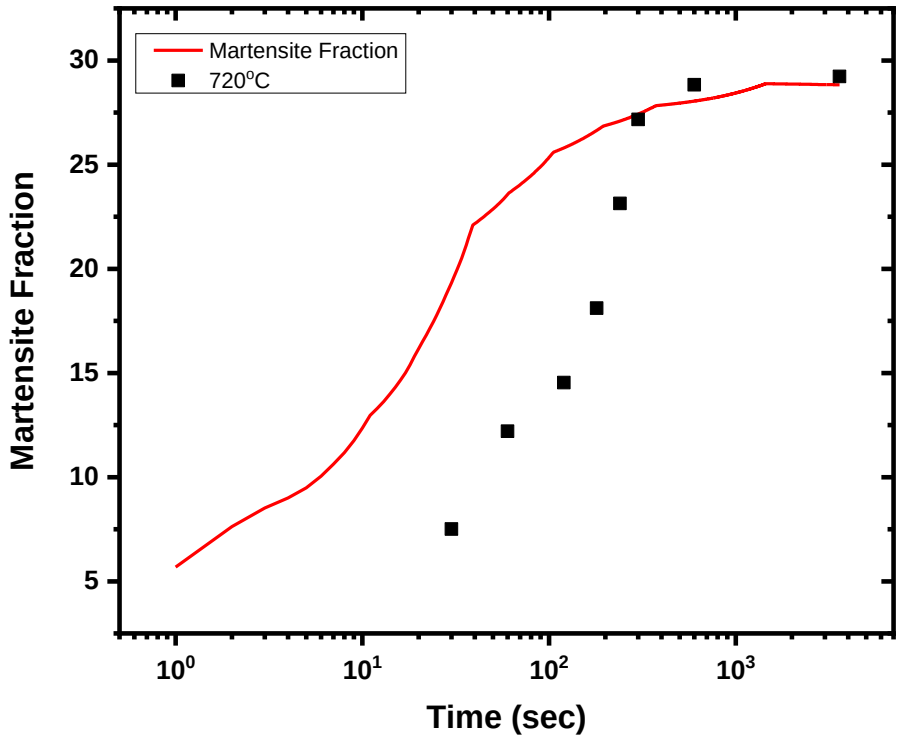

Figure 4.8: Kinetics of austenite formation for intercritical heat treatments at 720°C. Symbols represent the experimental results from G.C. Nanas [1], while the continuous red line the kinetic calculations with DICTRA software.

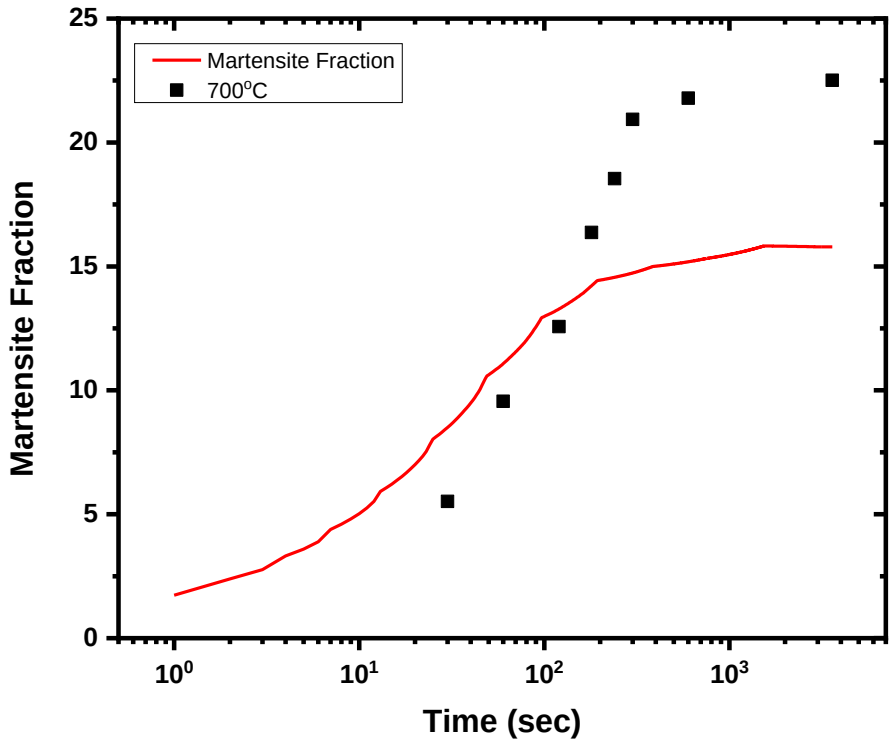

Figure 4.9: Kinetics of austenite formation for intercritical heat treatments at 700°C. Symbols represent the experimental results from G.C. Nanas [1], while the continuous red line the kinetic calculations with DICTRA software.

Chapter 5 Results

5.1 Simulation of IA process of DP-1000 and process design

The phase diagram that is presented in the Figure 5.1 was calculated with Thermo-Calc and TCFE6 database. The chemical composition was taken from Table 3.1. Austenite formation temperature during heating was calculated at 681.87°C (A_{c1}) and the temperature at which the transformation of ferrite to austenite is completed during heating (A_{c3}) was calculated at 803.42°C.

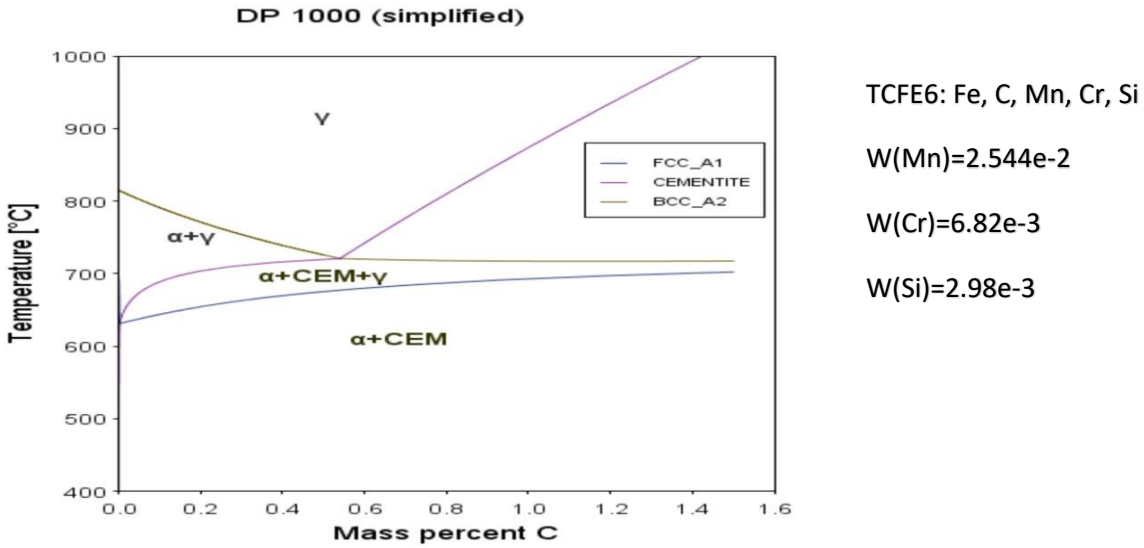

Figure 5.1: Isopleth diagram of DP1000 steel Calculated with THERMOCALC software and TCFE-6 database.

5.2 Results for the 1st Model (γ-α Model)

5.2.1 Computational kinetics Results for the 1st Model (γ-α Model)

Kinetic calculations of Intercritical Annealing of DP1000 steel were performed. The temperatures of isothermal holding are presented in Figure 5.2.

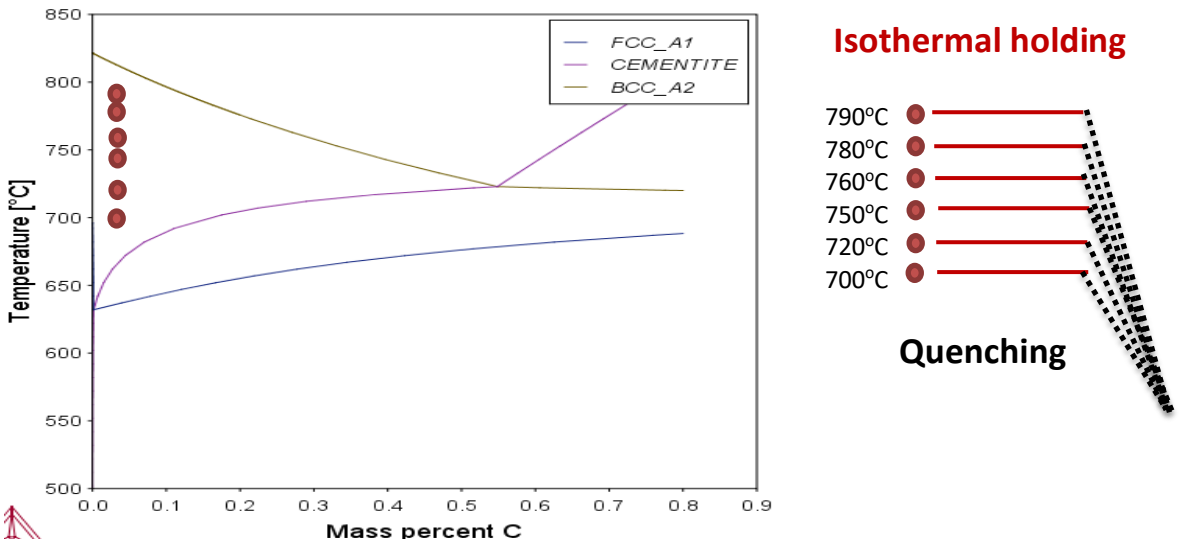

Figure 5.2: Isopleth diagram and heat treatment steps applied as an initial step IA and quenching.

The only effect to consider on the microstructure is the phase transformation from perlite-ferrite to austenite. Heating from room temperature to the intercritical annealing temperature in not considered in the model that was used and assumes the original microstructure as well as the initial conditions for the kinetic model, as conditions resulting from equilibrium calculations

Intercritical annealing was performed for 3600sec and the kinetic model (DICTRA –MOBFE-2) resulted in austenite volume fraction for each IA temperature with respect to holding time. Below are depicted six different figures. Every figure is for the same IA holding time but for different temperature. Figure 5.3 (a) depicts the austenite volume fraction for 790^{o}C, Figure 5.3 (b) depicts the austenite volume fraction for 780^{o}C and Figure 5.3 (c) for 760^{o}C. Figure 5.3 (d), Figure 5.3(e), Figure 5.3 (f) depict the austenite volume fraction for 750^{o}C 720^{o}C and 700^{o}C respectively (Table 5.1). It is evident that during IA the austenite volume fraction increases with increasing holding time. Also, higher IA temperature leads to higher austenite volume fraction. For the above six temperatures the element profiles for Carbon, Manganese Silicon and Chromium were created and are presented in the next pages. In Table 5.1, that follows a small list providing a small description of the figures and the temperature as well as the element they were calculated for, is presented. This list is provided as a guideline for the following pages.

Table 5.1: List, providing a small description of the figures and the temperature and the element they were calculated for

Temperature	Carbon profile	Manganese profile	Chromium profile	Silicon profile
790^{o}C	Figure 5.4	Figure 5.5	Figure 5.6	Figure 5.7
780^{o}C	Figure 5.8	Figure 5.9	Figure 5.10	Figure 5.11
760^{o}C	Figure 5.12	Figure 5.13	Figure 5.14	Figure 5.15
750^{o}C	Figure 5.16	Figure 5.17	Figure 5.18	Figure 5.19
720^{o}C	Figure 5.20	Figure 5.21	Figure 5.22	Figure 5.23
700^{o}C	Figure 5.24	Figure 5.25	Figure 5.26	Figure 5.27

In Figure 5.4 the partitioning of Carbon during intercritical annealing of DP1000 at 790^{o}C for 0, 5, 30, 50, 150, 300, 500, 1500, 2500, 3600sec, is presented. Austenite is on left the and with progressing time at IA moves towards the right consuming the preexisting ferrite, thus increasing in size with progressing holding time. The starting concentration of austenite (γ) is enriched in carbon and becomes depleted with holding time. The starting concentration of ferrite (α) in carbon is much smaller than that of the initial austenite becomes even more depleted with holding time.

The carbon concentration profile in austenite is divided in two areas. The left furthermost side of γ gains its C content, from the initial enriched γ region at 0sec. This side, as holding time increases, C is lowered, while on the right side, near the interface, γ gains the C content from the depletion of C from the neighboring ferrite.

Figure 5.5 illustrates the partitioning of Manganese during intercritical annealing of DP1000 at 790^{o}C for the same holding times mentioned above. It is evident that the Mn profile follows a similar behavior as in the case of carbon discussed previously. The Mn concentration profile in austenite is divided in two areas. The left furthermost side of γ gains its Mn content, from the initial enriched γ region at 0sec.

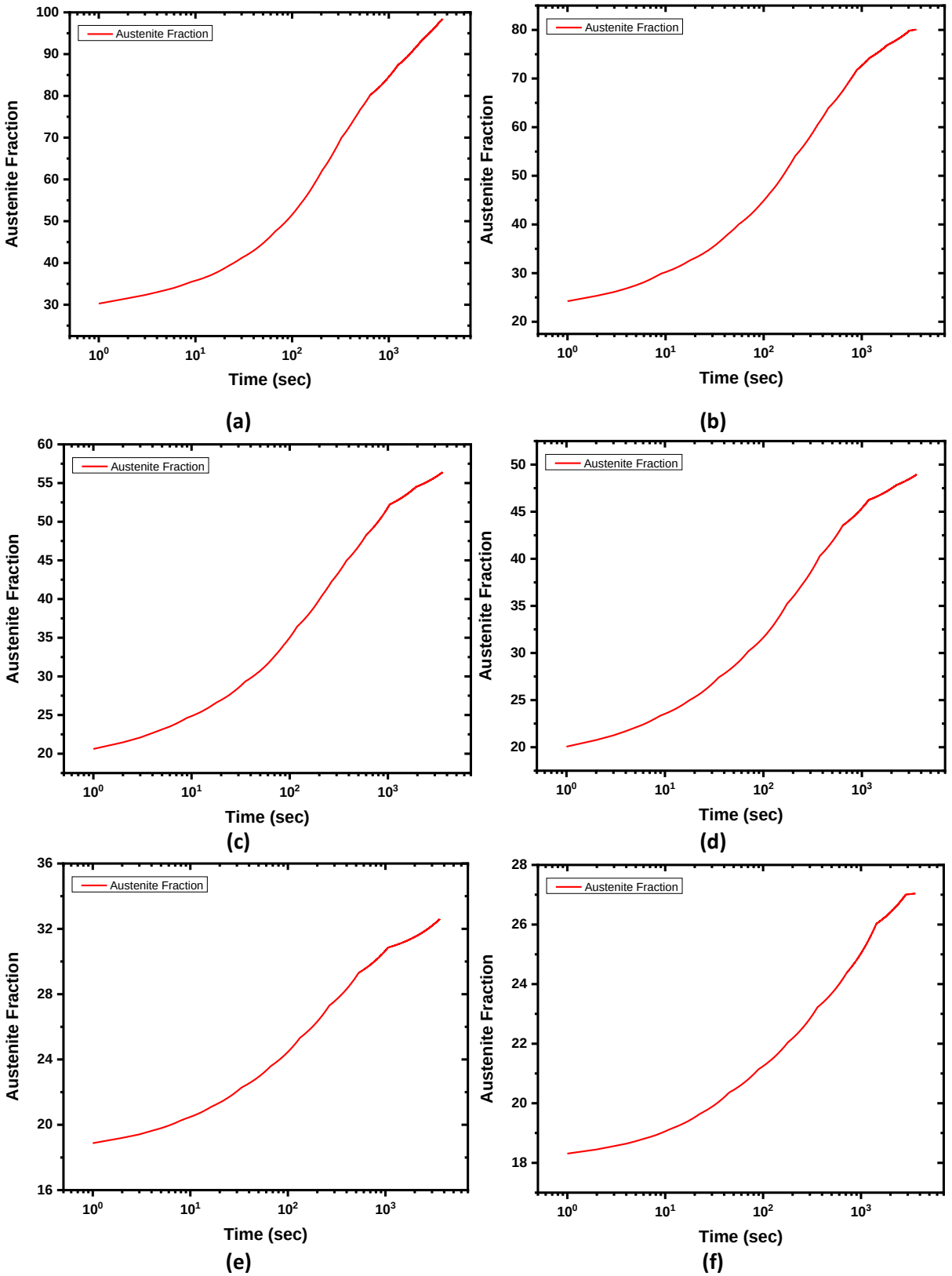

Figure 5.3: The evolution of austenite volume fraction for 800°C (a), 780°C (b), 760°C (c), 750°C (d), 720°C (e) and for 700°C (f) versus time.

This side, as holding time increases, is depleted from Mn, while on the right side, near the interface, γ is enriched in Mn, provided, from the depletion of Mn from the neighboring ferrite. The two areas are actually divided by the position of the initial interface between γ and α (t=0 sec). As Mn is the slower of the two main diffusing elements. The low diffusivity of Mn which needs more time at the IA temperature in order to diffuse from prior existing γ and α to the newly formed γ is the explanation for this phenomenon. Mn diffusion mechanism is substitutional while C diffusion is interstitial, the behavior of the C and Mn profiles is actually governed by the behavior of Mn.

Figure 5.6 presents the similarity in behavior between Cr and Mn. On the other hand, In contrast to Mn which tends to enrich austenite Silicon is depleted from austenite during IA holding as shown in the Figure 5.7. Higher intercritical annealing (IA) temperature leads to higher percentages of austenite and smooths out the profile of elements.

For IA at 790^{o}C the elemental profiles smooth out at about 1500 sec holding time.

In Figure 5.8 the partitioning of C, during intercritical annealing of DP1000 at 780^{o}C for 0, 5, 30, 50, 150, 300, 500, 1500, 2500, 3600sec, is presented. Austenite is on left ferrite on the right. As in the case of IA at 790^{o}C the carbon concentration profile in austenite is divided in two areas. The left furthermost side of γ gains its C content, from the initial enriched γ region at 0sec. This side, as holding time increases, C is lowered, while on the right side, near the interface, γ gains the C content from the depletion of C from the neighboring ferrite.

Figure 5.9 illustrates the partitioning of Manganese during intercritical annealing of DP1000 at 780^{o}C for the same holding times mentioned above. It is evident that the Mn profile follows a similar behavior as in the case of carbon discussed previously. The Mn concentration profile in austenite is divided in two areas. The left furthermost side of γ gains its Mn content, from the initial enriched γ region at 0sec. This side, as holding time increases, is depleted from Mn, while on the right side, near the interface, γ is enriched in Mn, provided, from the depletion of Mn from the neighboring ferrite. The two areas are divided by the position of the initial interface between γ and α (t=0 sec). As Mn is the slower of the two main diffusing elements. The low diffusivity of Mn which needs more time at the IA temperature in order to diffuse from prior existing γ and α to the newly formed γ is the explanation for this phenomenon. Mn diffusion mechanism is substitutional while C diffusion is interstitial, the behavior of the C and Mn profiles is governed by the behavior of Mn.

Figure 5.10 presents the similarity in behavior between Cr and Mn. On the other hand, in contrast to Mn which tends to enrich austenite Silicon is depleted from austenite during IA holding as shown in the Figure 5.11. Higher intercritical annealing (IA) temperature leads to higher percentages of austenite and smooths out the profile of elements.

For IA at 780^{o}C the elemental profiles smooth out at about 1500 sec holding time.

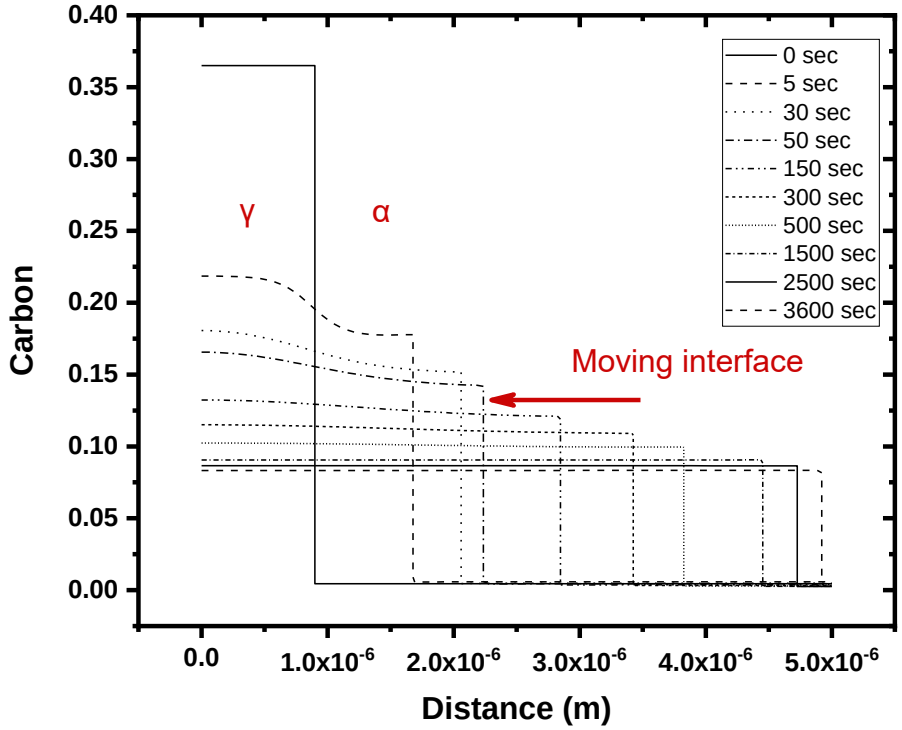

Figure 5.4: Partitioning of Carbon during intercritical annealing of DP1000 at 790°C for 0, 5, 30, 50, 150, 300, 500, 1500, 2500, 3600sec. Austenite is on left the and with progressing time at IA moves towards the right consuming preexisting ferrite.

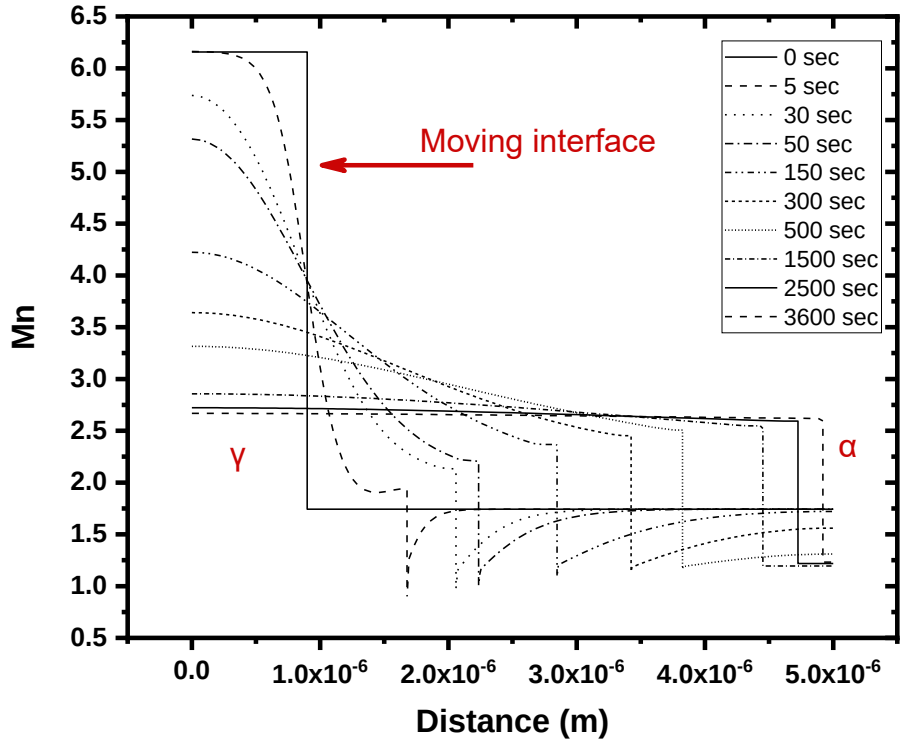

Figure 5.5: Partitioning of Manganese during intercritical annealing of DP1000 at 790°C for 0, 5, 30, 50, 150, 300, 500, 1500, 2500, 3600sec.

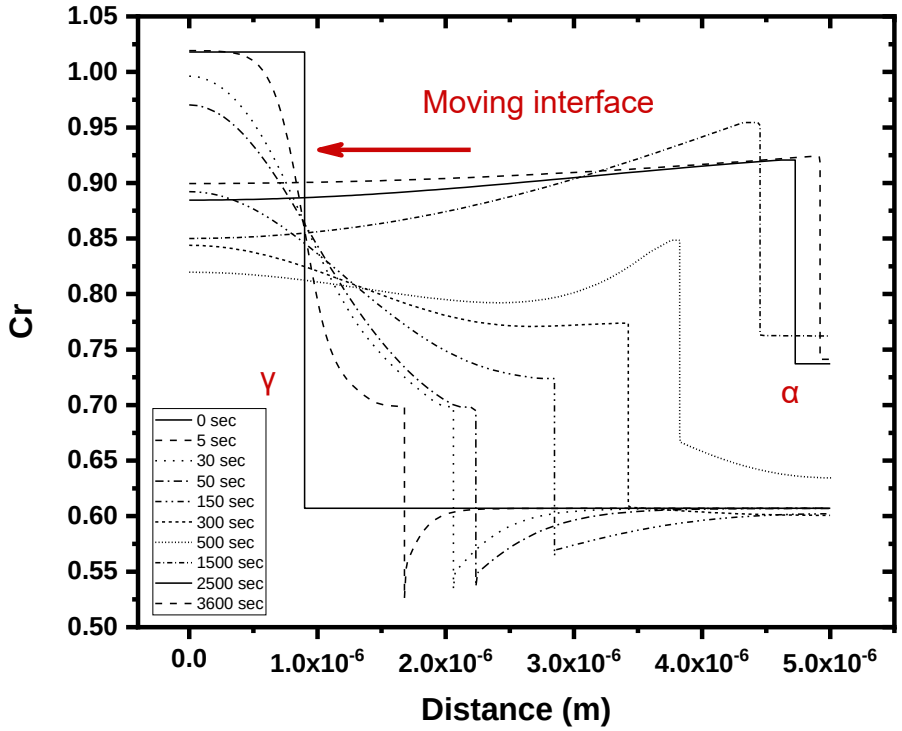

Figure 5.6: Partitioning of Chromium during intercritical annealing of DP1000 at 790°C for 0, 5, 30, 50, 150, 300, 500, 1500, 2500, 3600sec.

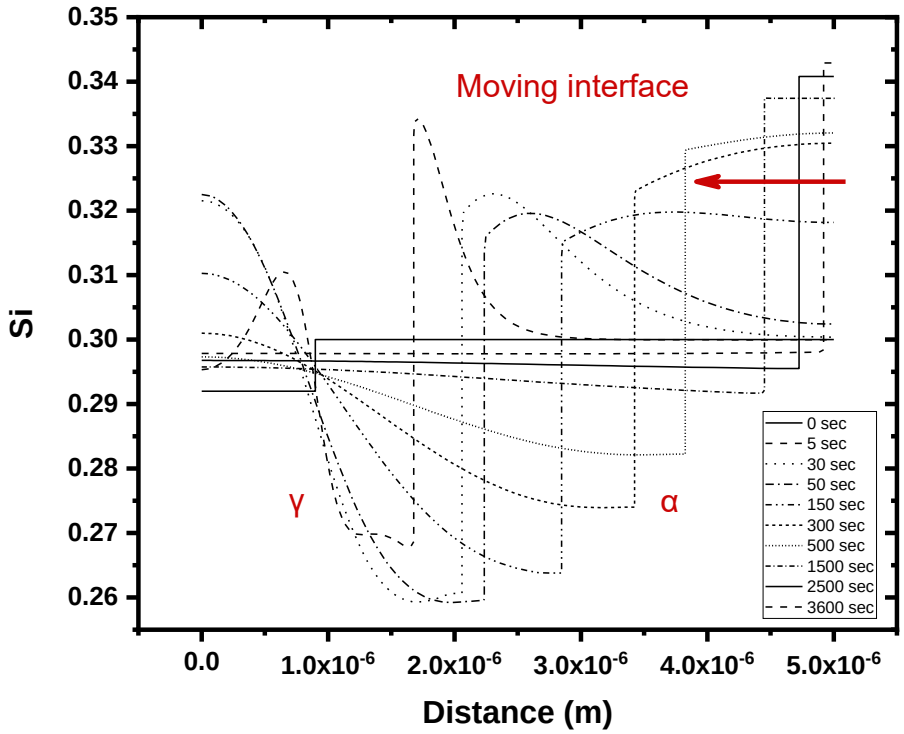

Figure 5.7: Partitioning of Silicon during intercritical annealing of DP1000 at 790°C for 0, 5, 30, 50, 150, 300, 500, 1500, 2500, 3600sec.

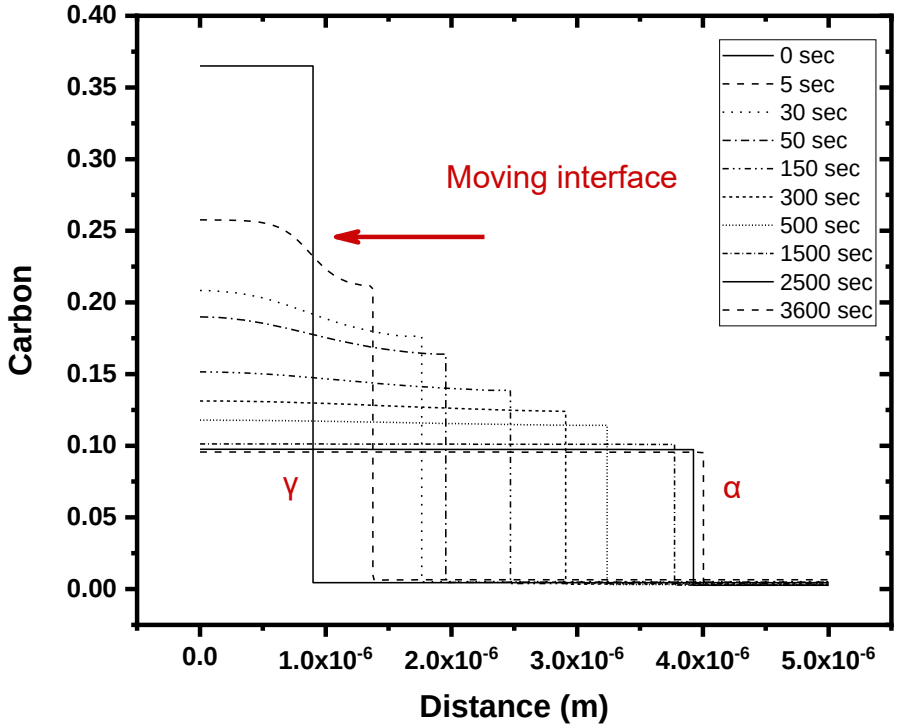

Figure 5.8: Partitioning of Carbon during intercritical annealing of DP1000 at 780°C for 0, 5, 30, 50, 150, 300, 500, 1500, 2500, 3600sec. Austenite is on left the and with progressing time at IA moves towards the right consuming preexisting ferrite.

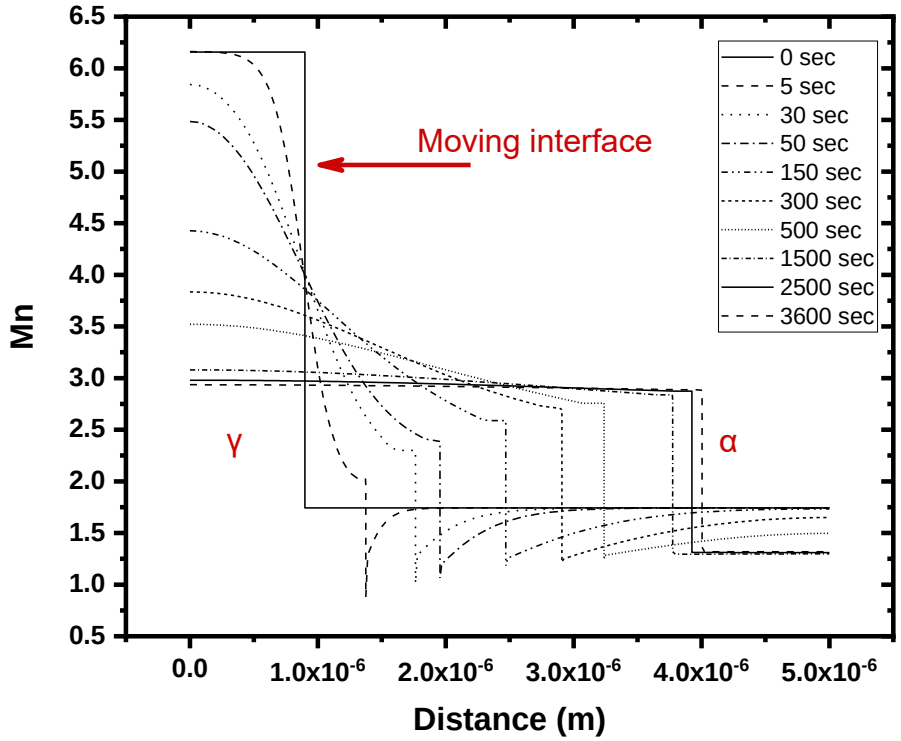

Figure 5.9: Partitioning of Manganese during intercritical annealing of DP1000 at 780°C for 0, 5, 30, 50, 150, 300, 500, 1500, 2500, 3600sec.

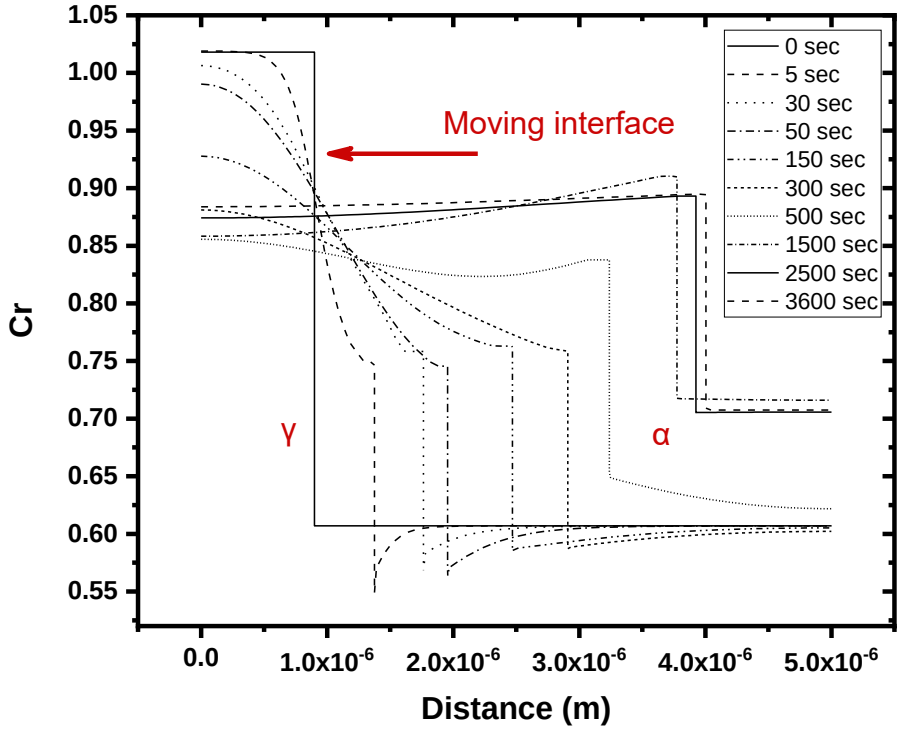

Figure 5.10: Partitioning of Chromium during intercritical annealing of DP1000 at 780°C for 0, 5, 30, 50, 150, 300, 500, 1500, 2500, 3600sec.

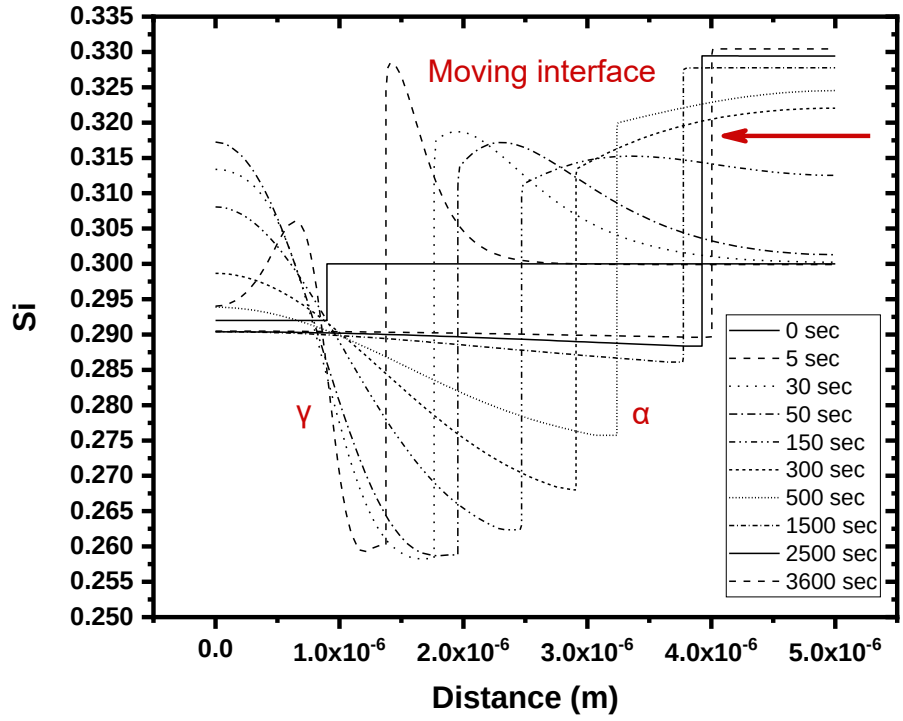

Figure 5.11: Partitioning of Silicon during intercritical annealing of DP1000 at 780°C for 0, 5, 30, 50, 150, 300, 500, 1500, 2500, 3600sec.

In Figure 5.12 the partitioning of C, during intercritical annealing of DP1000 at 760°C for 0, 5, 30, 50, 150, 300, 500, 1500, 2500, 3600sec, is presented. Austenite is on left ferrite on the right. As in the case of IA at 790°C and 780°C the carbon concentration profile in austenite is divided in two areas. The left furthermost side of γ gains its C content, from the initial enriched γ region at 0sec. This side, as holding time increases, C is lowered, while on the right side, near the interface, γ gains the C content from the depletion of C from the neighboring ferrite. Because 760°C is a lower temperature than 790°C and 780°C the overall kinetics of austenite formation are slower and less γ is formed at corresponding times. This results in higher enrichment of γ. Furthermore, the difference in C content between the two areas in γ is less pronounced.

Figure 5.13 illustrates the partitioning of Manganese during intercritical annealing of DP1000 at 760°C for the same holding times mentioned above. It is evident that the Mn profile follows a similar behavior as in the case of carbon discussed previously. The Mn concentration profile in austenite is divided in two areas. The left furthermost side of γ gains its Mn content, from the initial enriched γ region at 0sec. This side, as holding time increases, is depleted from Mn, while on the right side, near the interface, γ is enriched in Mn, provided, from the depletion of Mn from the neighboring ferrite. The two areas are actually divided by the position of the initial interface between γ and α (t=0 sec). As Mn is the slower of the two main diffusing elements. The low diffusivity of Mn which needs more time at the IA temperature in order to diffuse from prior existing γ and α to the newly formed γ is the explanation for this phenomenon. Mn diffusion mechanism is substitutional while C diffusion is interstitial, the behavior of the C and Mn profiles is actually governed by the behavior of Mn.

Figure 5.14 presents the similarity in behavior between Cr and Mn. On the other hand, In contrast to Mn which tends to enrich austenite Silicon is depleted from austenite during IA holding as shown in the Figure 5.15. Higher intercritical annealing (IA) temperature leads to higher percentages of austenite and smooths out the profile of elements. For IA at 760°C the elemental profiles smooth out at about 300sec holding time.

A similar behavior is observed for IA at 750°C. The elemental profile for C is presented in Figure 5.16, for Mn in Figure 5.17, for Cr in Figure 5.18 and finally for Si in Figure 5.19.

On the other hand, a different behavior is observed for IA at 720°C and 700°C. In Figure 5.20 the partitioning of Carbon during intercritical annealing of DP1000 at 720°C, is presented. Austenite is on left the and with progressing time at IA moves towards the right consuming the preexisting ferrite, thus increasing in size with progressing holding time. The starting concentration of austenite (γ) is enriched in carbon and becomes depleted with holding time. The starting concentration of ferrite (α) in carbon is much smaller than that of the initial austenite becomes even more depleted with holding time.

The carbon concentration profile in austenite is smooth and not divided in two areas as for higher temperatures. All of the γ phase C content is provided from the initial enriched γ region at 0 sec. As holding time increases, C is lowered, because of the formation of new γ. For lower temperatures γ does not get any enrichment from ferrite. Although the overall volume fraction of austenite formed is smaller than for the higher temperatures, the C profile is smooth and more enriched.

Figure 5.21 illustrates the partitioning of Manganese during intercritical annealing of DP1000 at 720°C. It is evident that the Mn profile follows a similar behavior as in the case of carbon discussed previously. The Mn concentration profile in austenite is also smooth and more enriched. Figure 5.22 presents the similarity in behavior between Cr and Mn, Silicon profile is in the Figure 5.23. For IA at 720°C the elemental profiles smooth out at about 50 sec holding time.

A similar behavior is observed for IA at 700°C. The elemental profile for C is presented in Figure 5.24, for Mn in Figure 5.25, for Cr in Figure 5.26 and finally for Si in Figure 5.27.

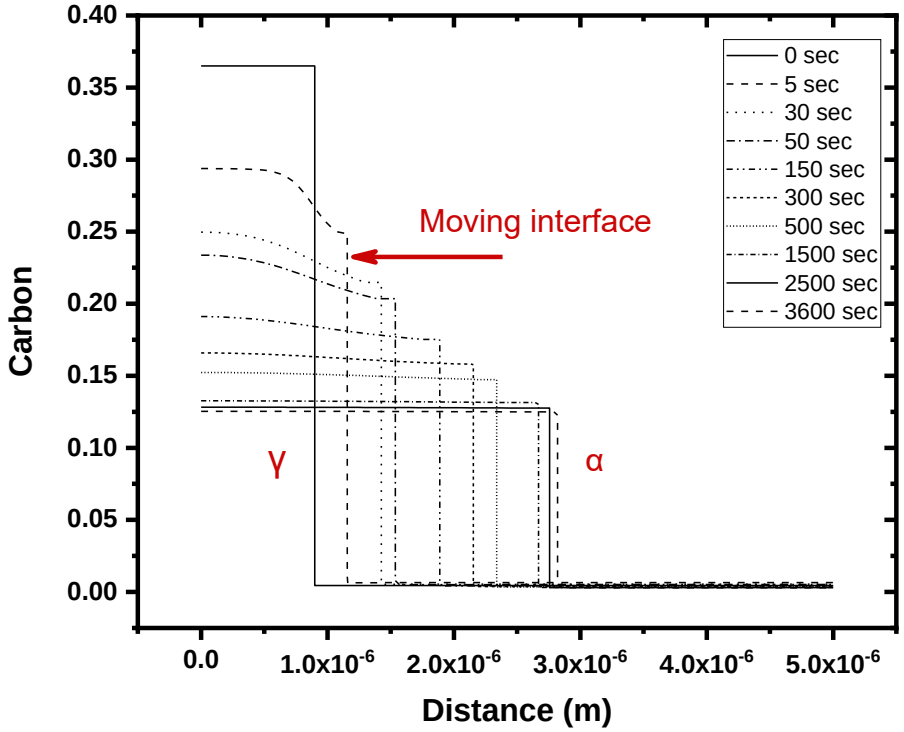

Figure 5.12: Partitioning of Carbon during intercritical annealing of DP1000 at 760°C for 0, 5, 30, 50, 150, 300, 500, 1500, 2500, 3600sec. Austenite is on left the and with progressing time at IA moves towards the right consuming preexisting ferrite.

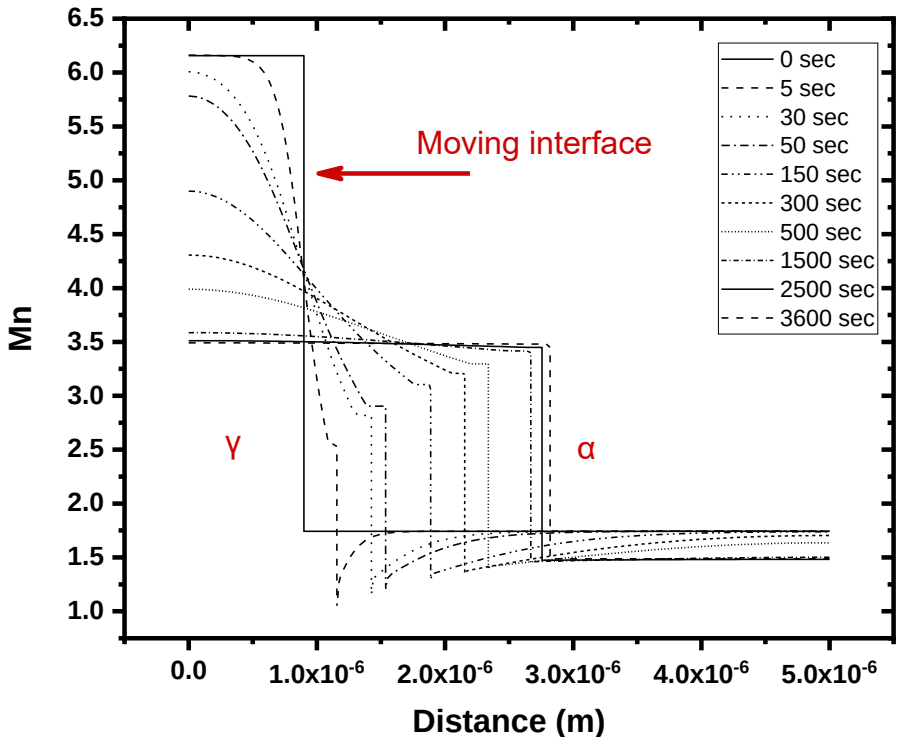

Figure 5.13: Partitioning of Manganese during intercritical annealing of DP1000 at 760°C for 0, 5, 30, 50, 150, 300, 500, 1500, 2500, 3600sec.

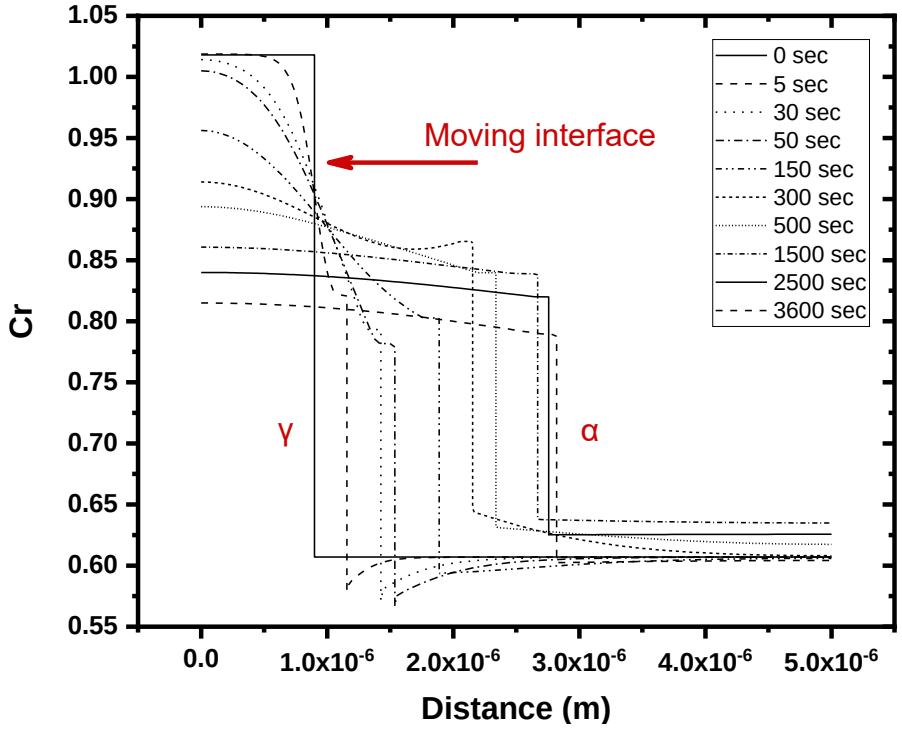

Figure 5.14: Partitioning of Chromium during intercritical annealing of DP1000 at 760°C for 0, 5, 30, 50, 150, 300, 500, 1500, 2500, 3600sec.

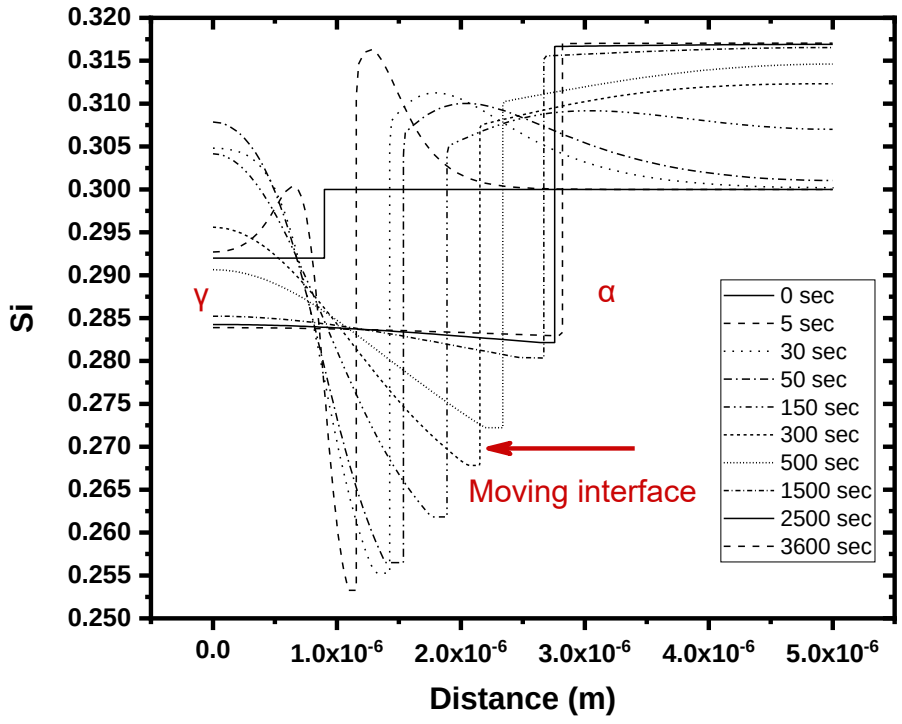

Figure 5.15: Partitioning of Silicon during intercritical annealing of DP1000 at 760°C for 0, 5, 30, 50, 150, 300, 500, 1500, 2500, 3600sec.

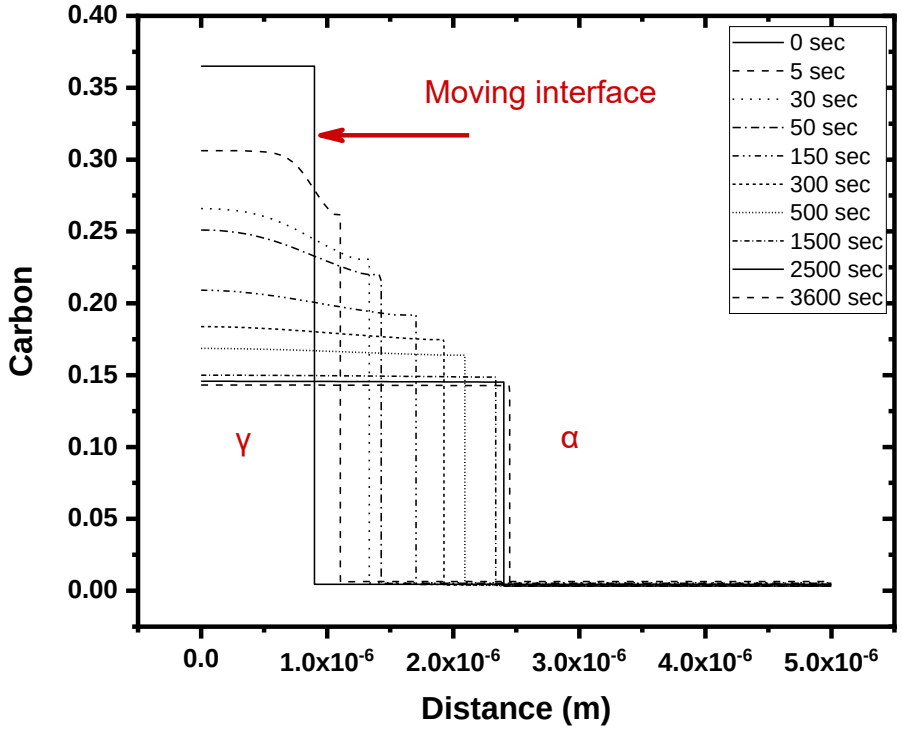

Figure 5.16: Partitioning of Carbon during intercritical annealing of DP1000 at 750°C for 0, 5, 30, 50, 150, 300, 500, 1500, 2500, 3600sec. Austenite is on left the and with progressing time at IA moves towards the right consuming preexisting ferrite.

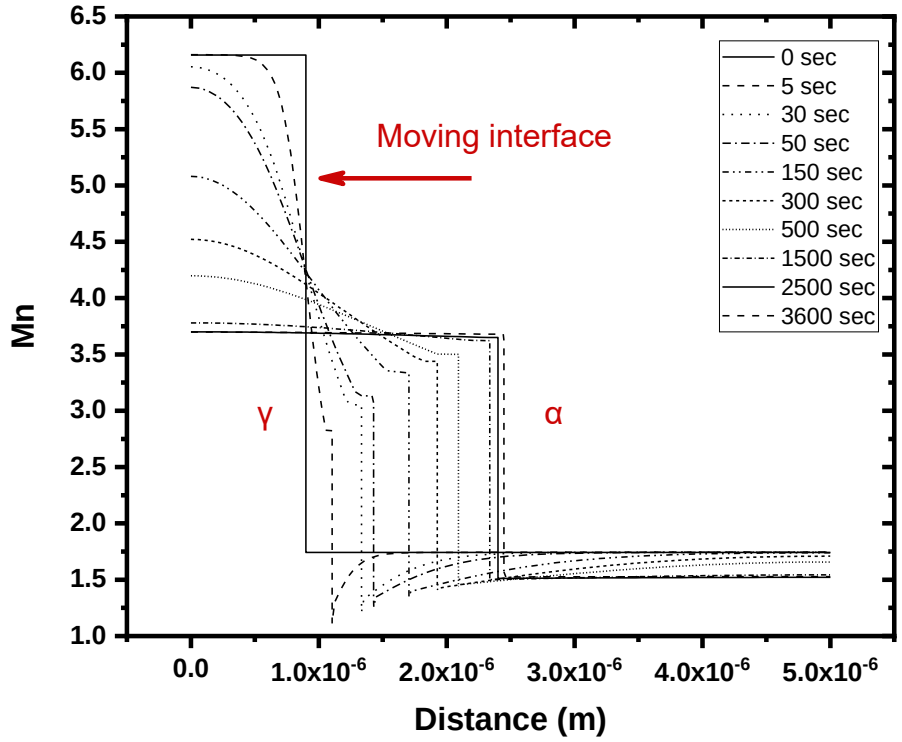

Figure 5.17: Partitioning of Manganese during intercritical annealing of DP1000 at 750°C for 0, 5, 30, 50, 150, 300, 500, 1500, 2500, 3600sec.

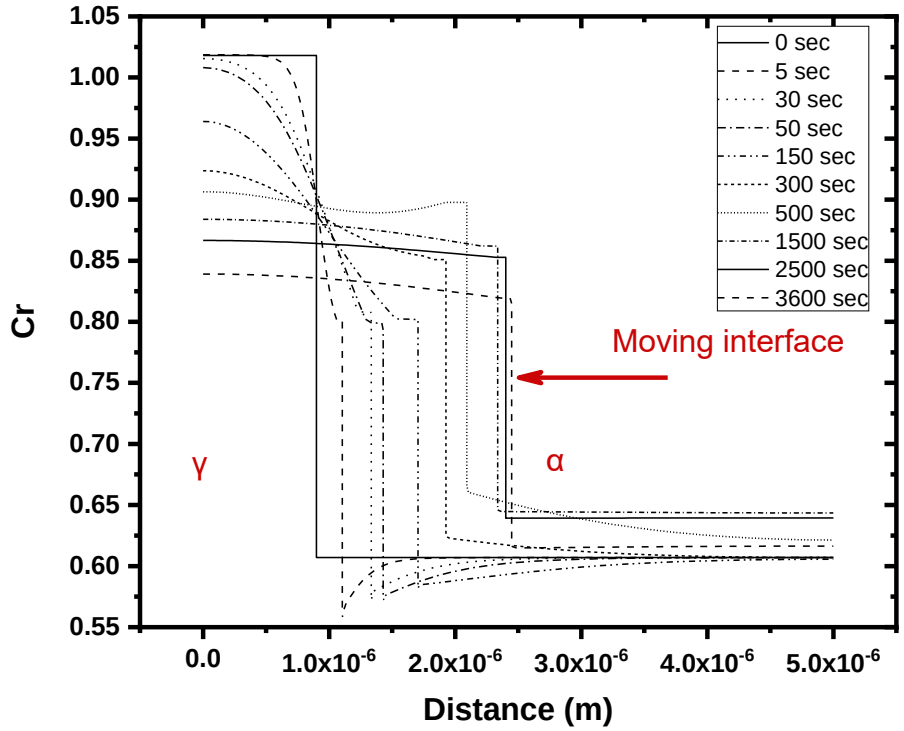

Figure 5.18: Partitioning of Chromium during intercritical annealing of DP1000 at 750°C for 0, 5, 30, 50, 150, 300, 500, 1500, 2500, 3600sec.

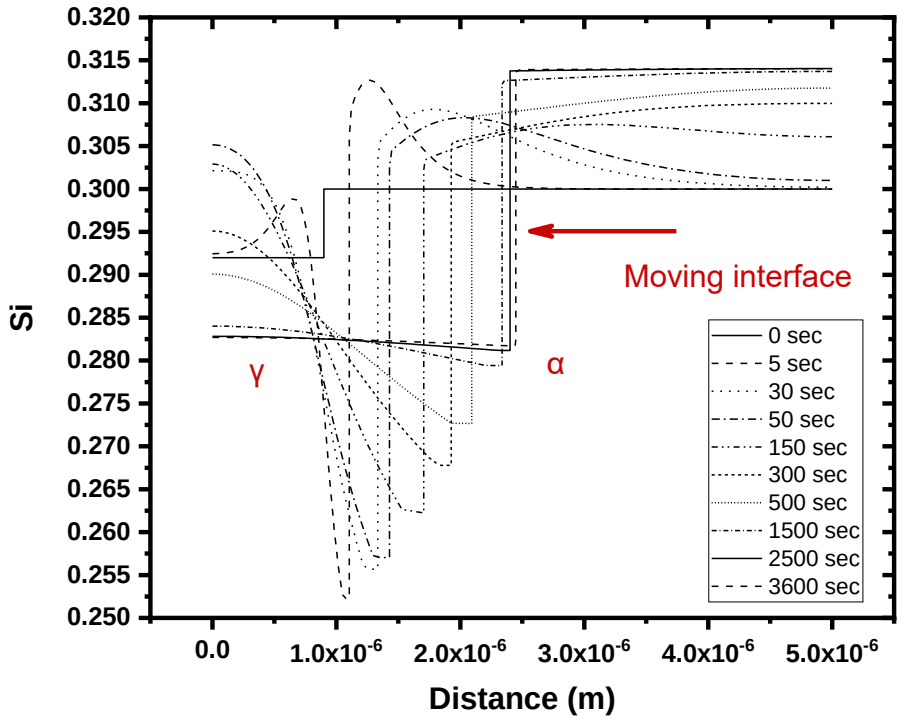

Figure 5.19: Partitioning of Silicon during intercritical annealing of DP1000 at 750°C for 0, 5, 30, 50, 150, 300, 500, 1500, 2500, 3600sec.

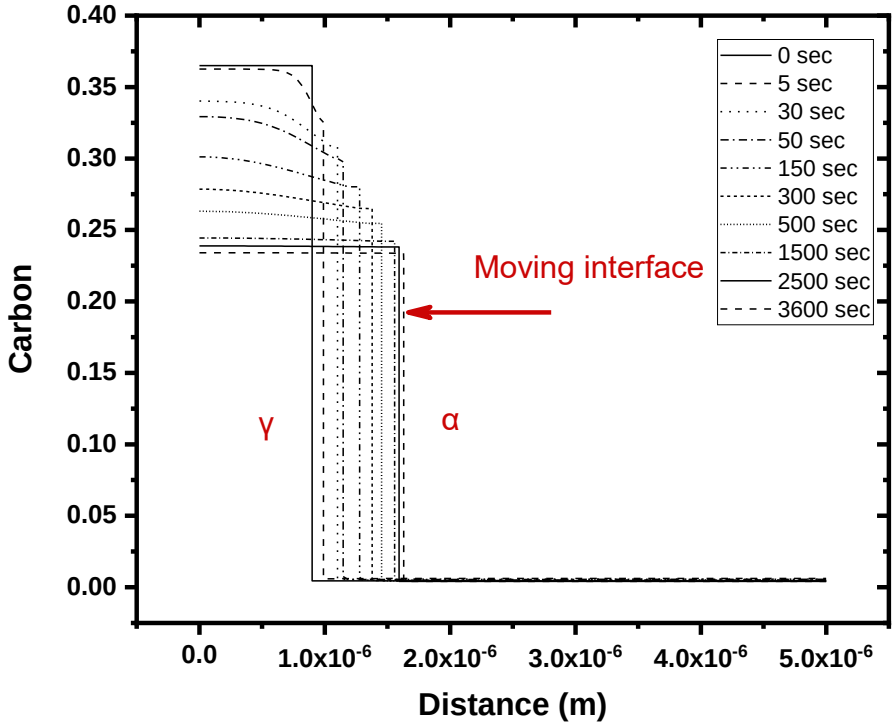

Figure 5.20: Partitioning of Carbon during intercritical annealing of DP1000 at 720°C for 0, 5, 30, 50, 150, 300, 500, 1500, 2500, 3600sec. Austenite is on left the and with progressing time at IA moves towards the right consuming preexisting ferrite.

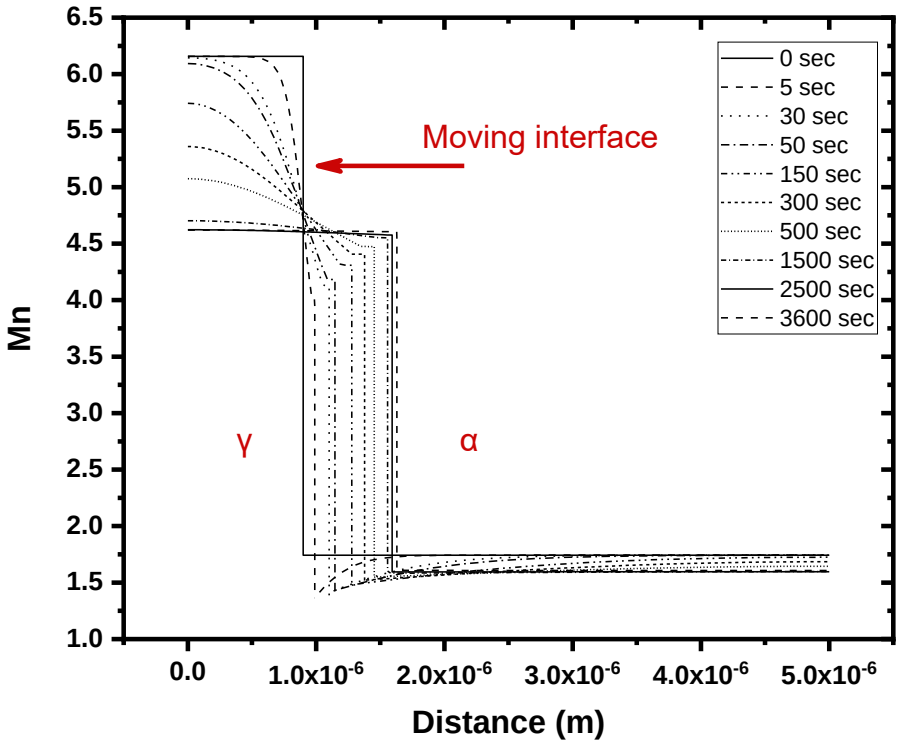

Figure 5.21: Partitioning of Manganese during intercritical annealing of DP1000 at 720°C for 0, 5, 30, 50, 150, 300, 500, 1500, 2500, 3600sec.

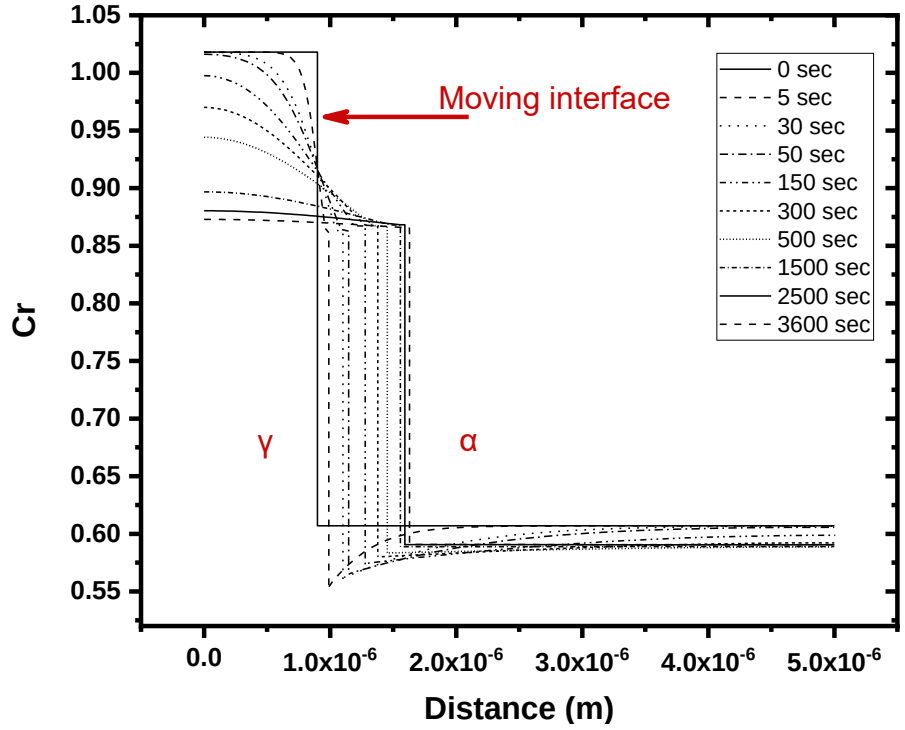

Figure 5.22: Partitioning of Chromium during intercritical annealing of DP1000 at 720°C for 0, 5, 30, 50, 150, 300, 500, 1500, 2500, 3600sec.

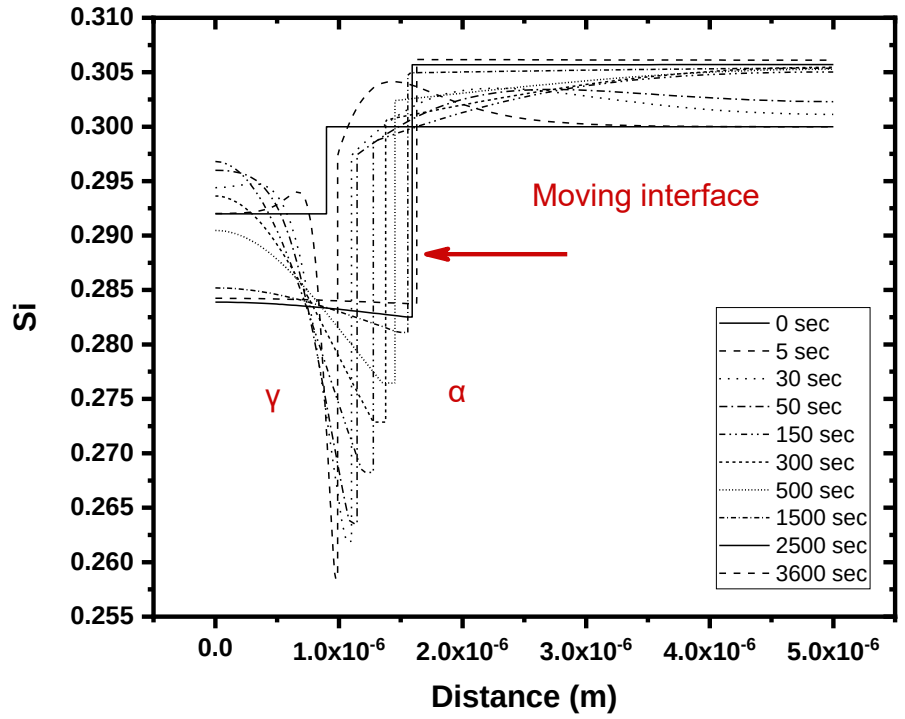

Figure 5.23: Partitioning of Silicon during intercritical annealing of DP1000 at 720°C for 0, 5, 30, 50, 150, 300, 500, 1500, 2500, 3600sec.

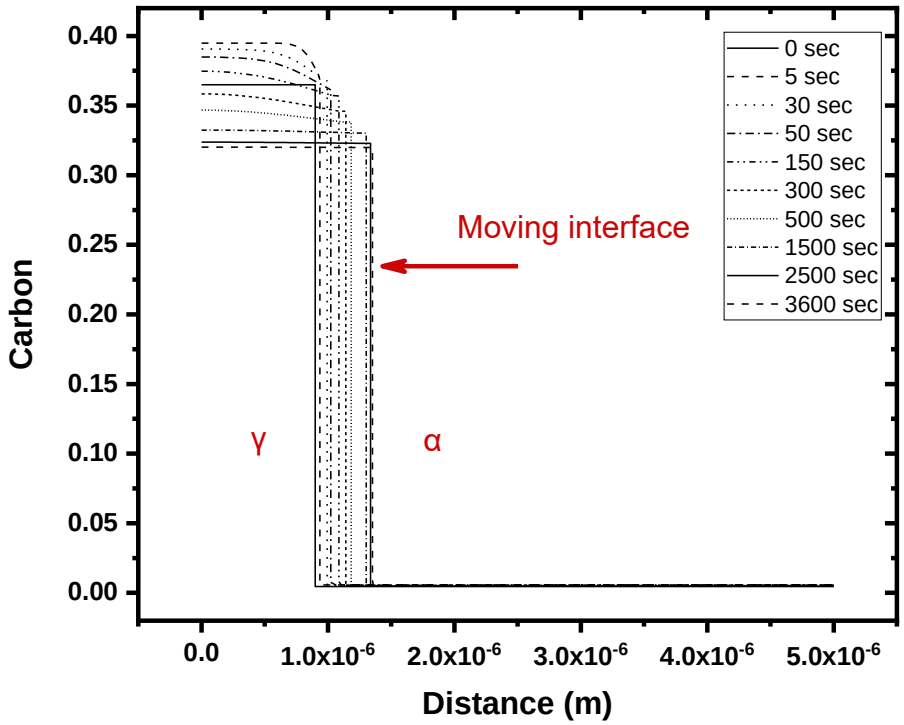

Figure 5.24: Partitioning of Carbon during intercritical annealing of DP1000 at 700°C for 0, 5, 30, 50, 150, 300, 500, 1500, 2500, 3600sec. Austenite is on left the and with progressing time at IA moves towards the right consuming preexisting ferrite.

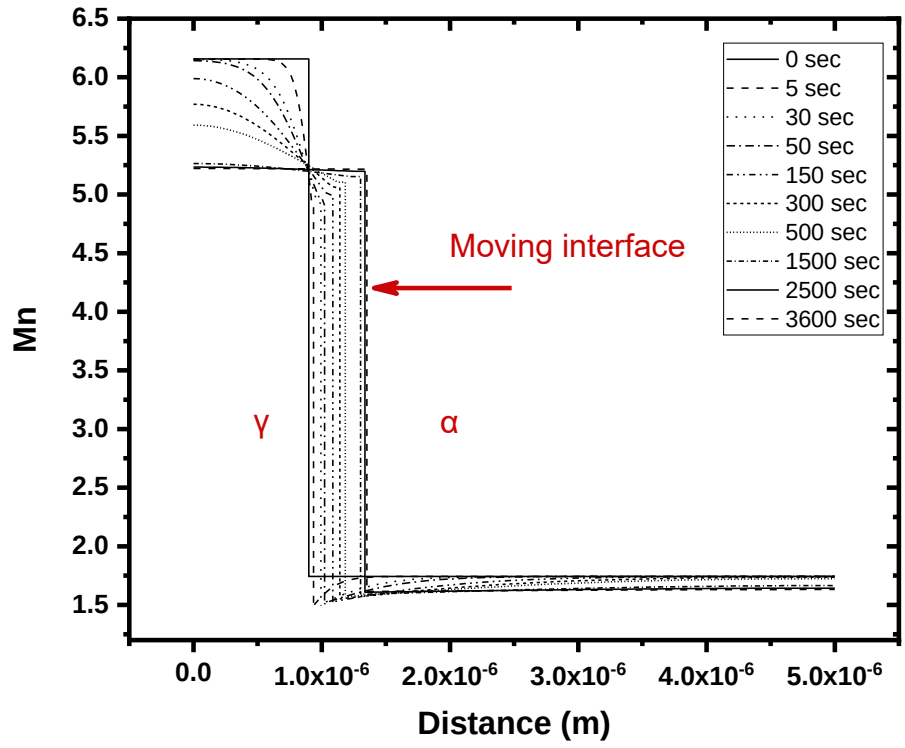

Figure 5.25: Partitioning of Manganese during intercritical annealing of DP1000 at 700°C for 0, 5, 30, 50, 150, 300, 500, 1500, 2500, 3600sec.

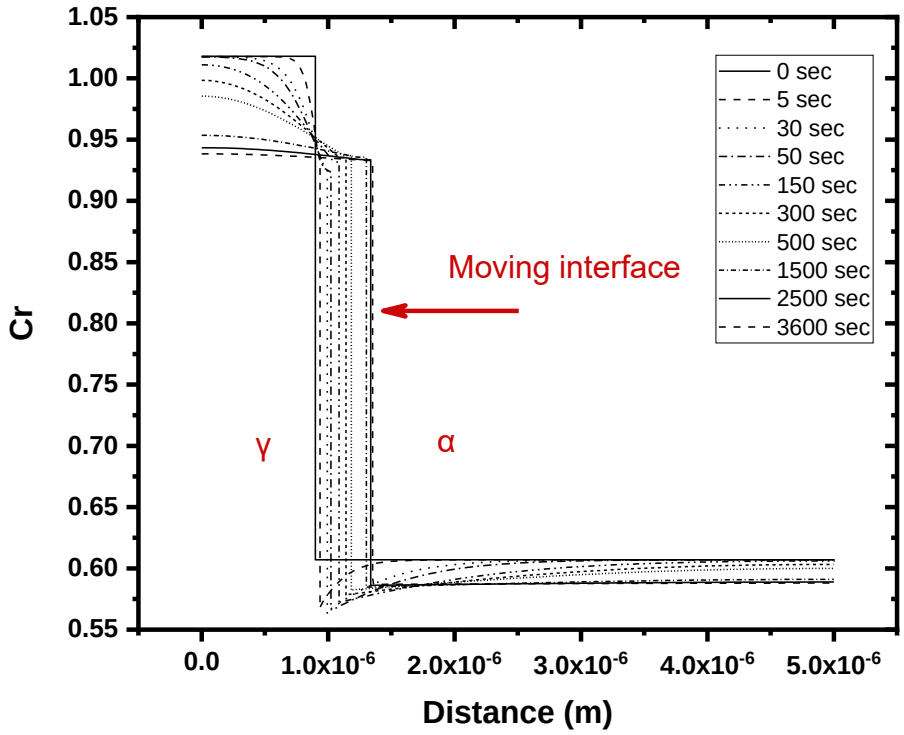

Figure 5.26: Partitioning of Chromium during intercritical annealing of DP1000 at 700°C for 0, 5, 30, 50, 150, 300, 500, 1500, 2500, 3600sec.

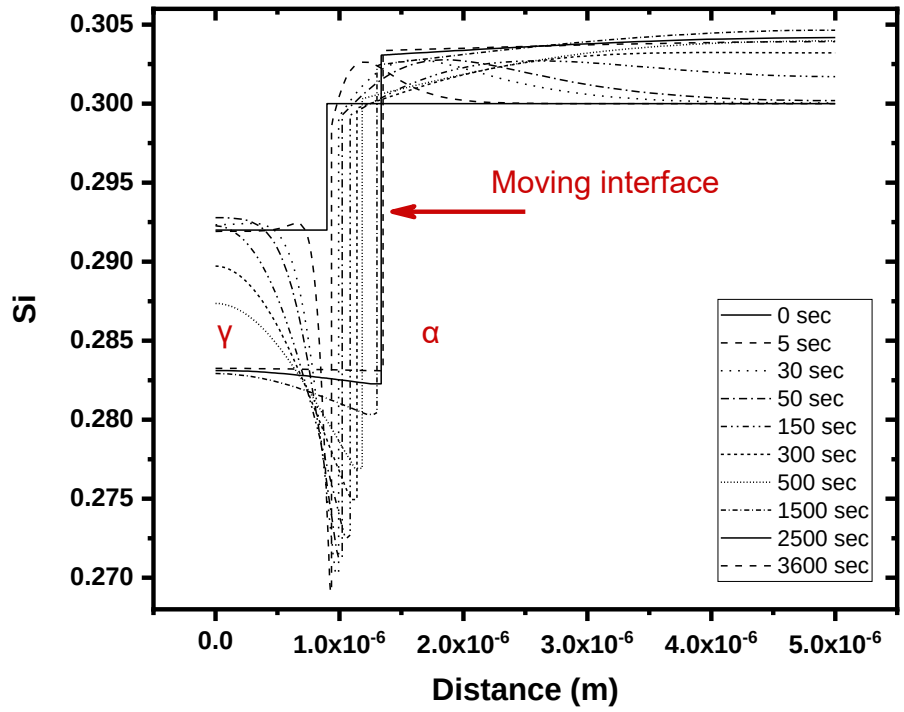

Figure 5.27: Partitioning of Silicon during intercritical annealing of DP1000 at 700°C for 0, 5, 30, 50, 150, 300, 500, 1500, 2500, 3600sec.

5.2.2 Results for Martensite formation for the 1st Model (γ-α Model)

Quenching is simulated with the MATLAB software. The concentration profiles illustrated in the figures above among with the POI (position of interface) at distinct time intervals (from 0 to 3600 sec with a step of 1 sec), were used as input for the Koistinen-Marburger model. The above procedure yielded results for the martensite and retained austenite volume fractions, as a function of the heat treatment time. The figures that follow illustrate examples for IA at different temperatures. Figure 5.28 (a) and Figure 5.28 (b) depict the volume fraction of austenite (black dashed lines), martensite (black lines) and the volume fraction of retained austenite (red line) for IA at 790°C and 780°C respectively. The austenite volume fraction and the martensite volume fraction increase with increasing IA holding time as expected. The volume fraction of retained austenite decreases with increasing IA holding time. Figure 5.29 (a),Figure 5.29 (b), Figure 5.30 (a) Figure 5.30 (b) illustrate similar results for IA at 760°C, 750°C, 720°Cand 700°C respectively. Figure 5.31 illustrates the Carbon content in martensite (red line), austenite (green line), retained austenite (black line) and ferrite (blue line) with respect to IA time, for IA at 790 °C (a), for IA at 780 °C (b), for IA at 760 °C (c), for IA at 750 °C (d), for IA at 720°C (e) and for IA at 700°C (f). Carbon is depleted from all three phases with the progression of intercritical annealing.

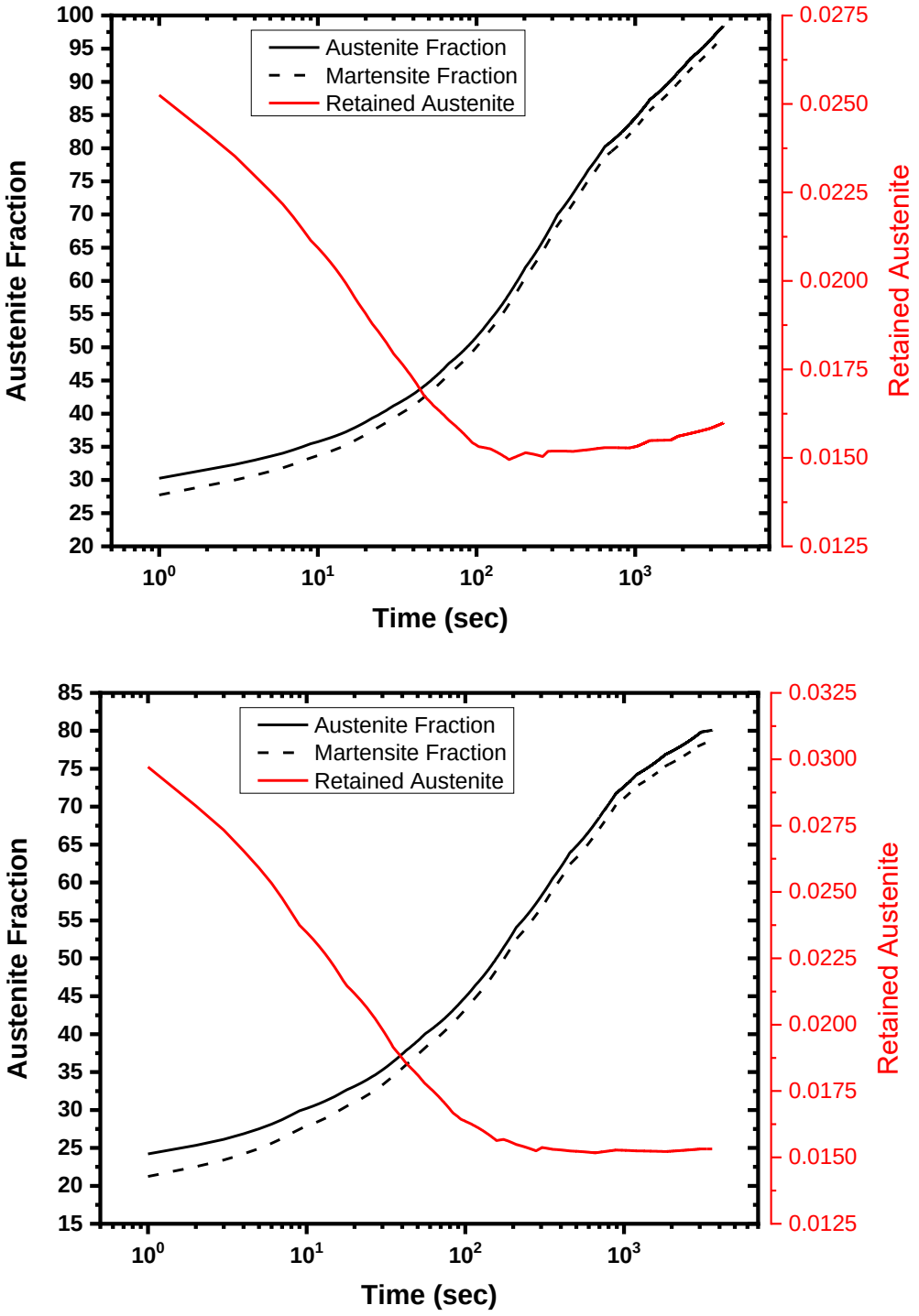

Figure 5.28: The volume fraction of austenite and martensite (black lines) and the volume fraction of retained austenite (red line) for IA at 790°C (a) and 780°C (b),for 3600sec.

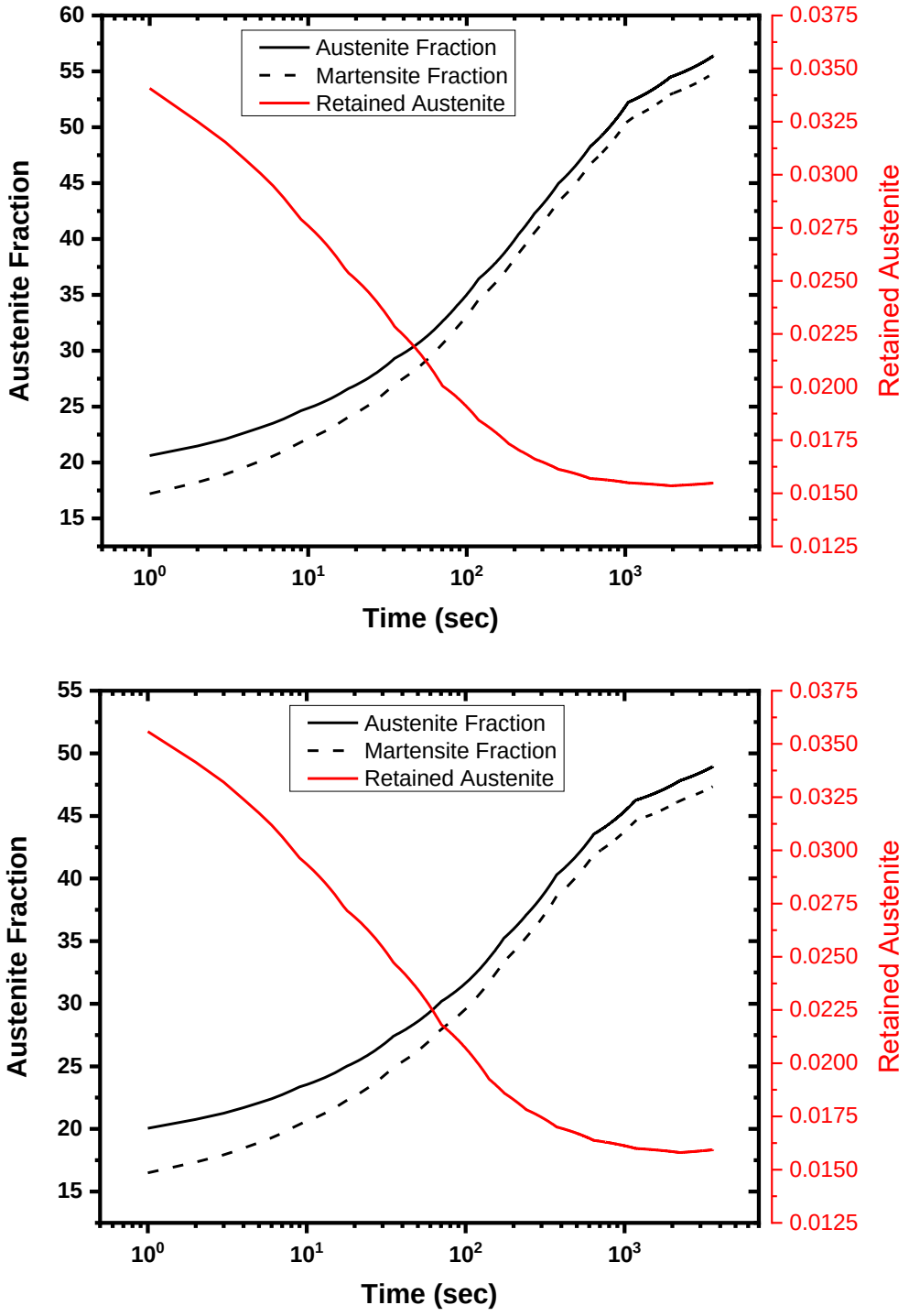

Figure 5.29: The volume fraction of austenite and martensite (black lines) and the volume fraction of retained austenite (red line) for IA at 760°C (a) and 750°C (b),for 3600sec.

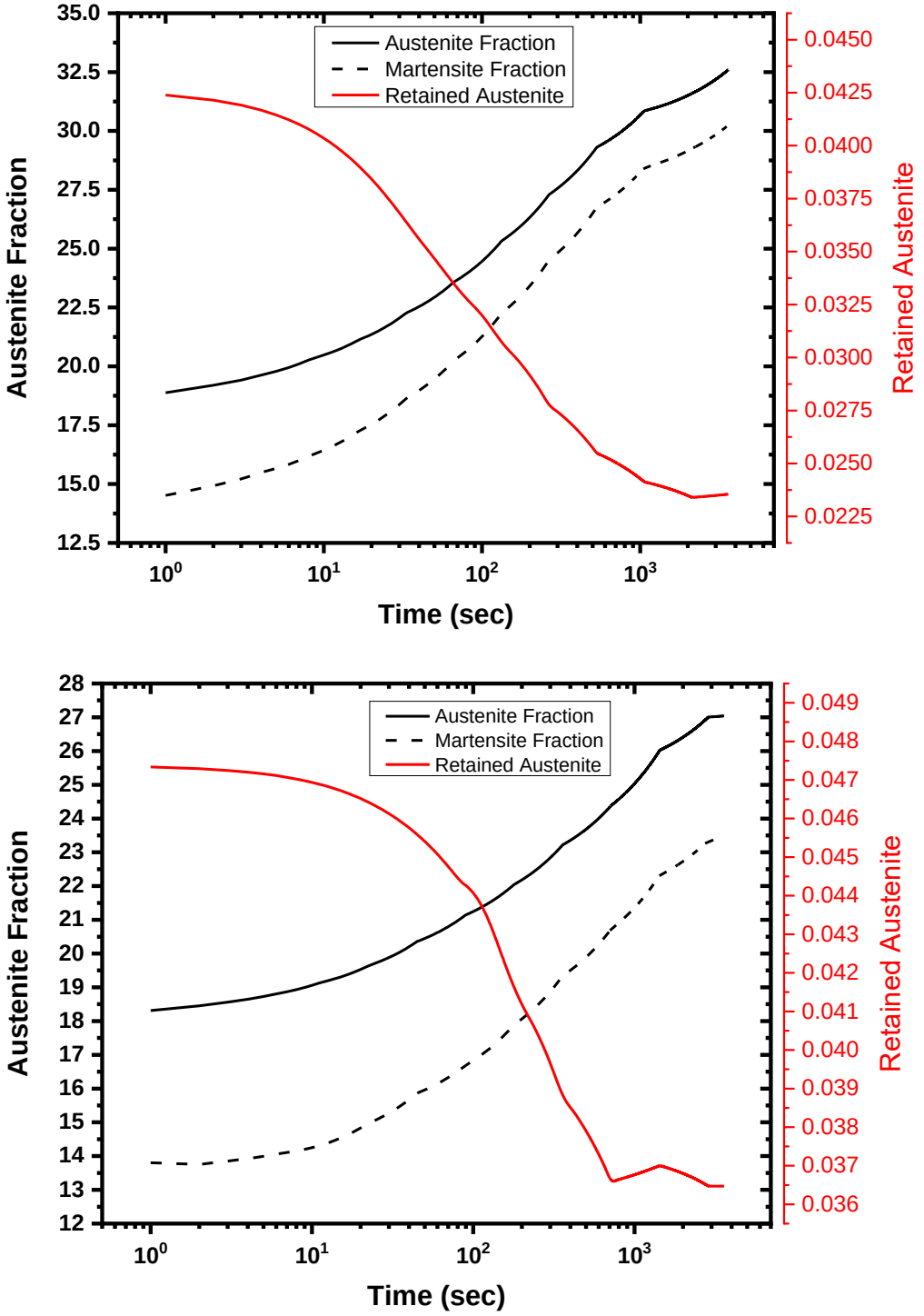

Figure 5.30: The volume fraction of austenite and martensite (black lines) and the volume fraction of retained austenite (red line) for IA at 720°C (a) and 700°C (b),for 3600sec.

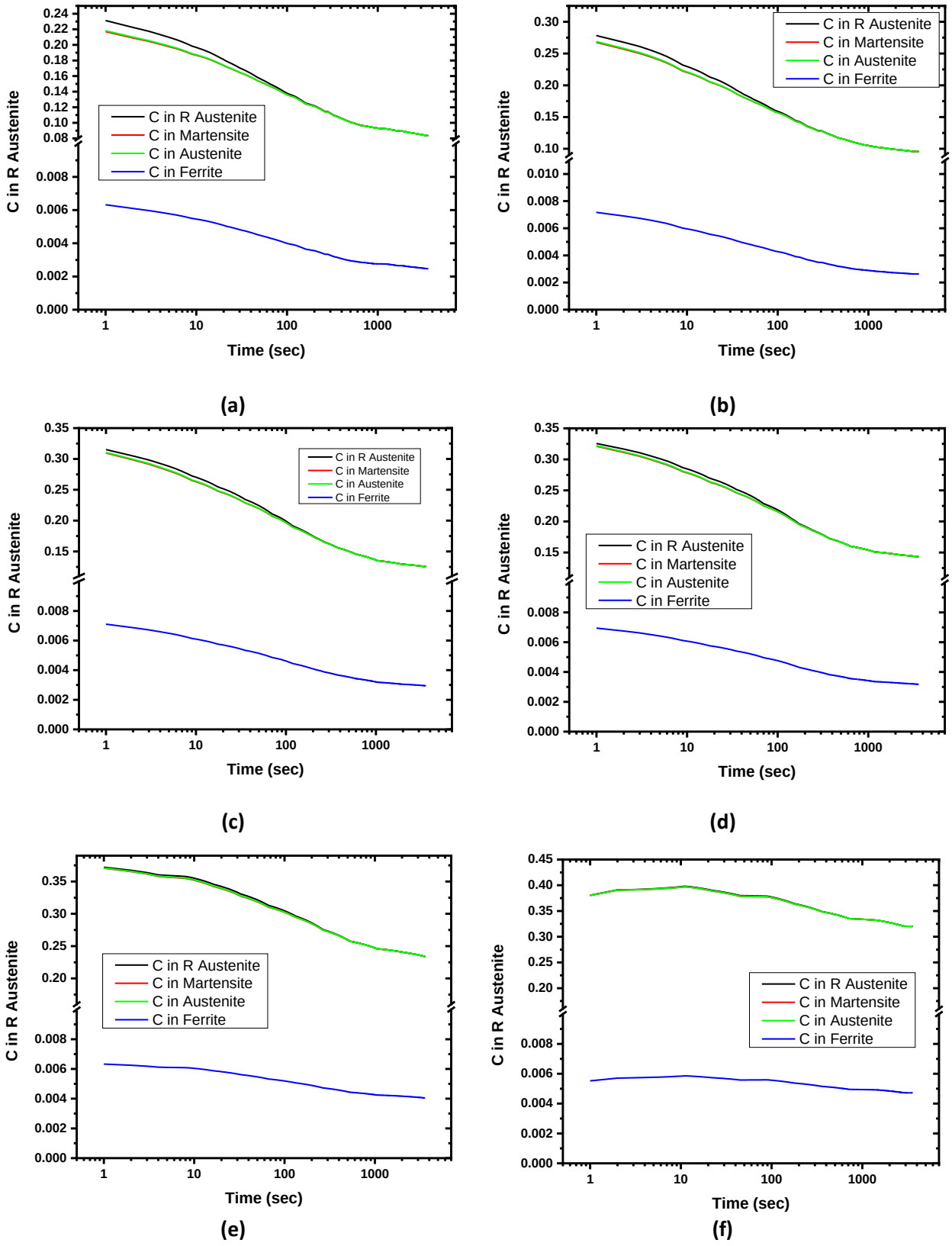

Figure 5.31: Carbon content in martensite (red line), austenite (green line), retained austenite(black line) and ferrite(blue line) for 3600sec with respect to IA time for IA at 790 °C (a), for IA at 780 °C (b), for IA at 760 °C (c), for IA at 750 °C (d), for IA at 720°C (e) and for IA at 700°C (f).

5.2.3 Results for Mapping for the 1st Model (γ-α Model)

Several maps are illustrated bellow in order to connect the results that emerged from the simulation with the procedure for the process design. These maps show the effect of IA temperature and time on martensite's volume fraction, on the volume fraction of Mn (manganese), C (carbon), Si (silicon) and retained austenite after quenching from the IA temperature as well as the volume fraction of austenite at the IA temperature.

Figure 5.32 depicts the volume fraction of austenite for six different temperatures compared with intercritical annealing (IA) holding time and intercritical annealing (IA) temperature before cooling. As it is expected, at higher IA temperatures more austenite is formed. For the 1st Model (γ-α Model), at 790^{o}C it is notable that almost 100% austenite has been formed which means that the full austenitic zone is close. Martensite's fraction after quenching is depicted on Figure 5.33. like austenite, martensite's volume fraction is increasing at higher temperatures. Also, according to Figure 5.33, as temperatures rises martensite formation is faster. Retained austenite is illustrated in Figure 5.34 with respect to IA temperature and IA holding time. For higher IA temperatures retained austenite percentages drop significantly. Figure 5.35 depicts the content of carbon in martensite. In Figure 5.36, Figure 5.37, Figure 5.38 is illustrated the map of austenite, martensite and retained austenite after quenching respectively. All in respect with IA time and IA temperature. The next three figures (Figure 5.39, Figure 5.40 and Figure 5.41), depict the mapping of different alloying elements in martensite. Figure 5.39 depicts the mapping of carbon (C) content in martensite with respect to IA time and IA temperature, while Figure 5.40 and Figure 5.41 the mapping of manganese (Mn) content and silicon (Si) content in martensite respectively. Black lines in Figure 5.42 represent the mapping of martensite and red lines the mapping of carbon (C) content in martensite. It is clear that as the martensite percentages increase, carbon content decreases.

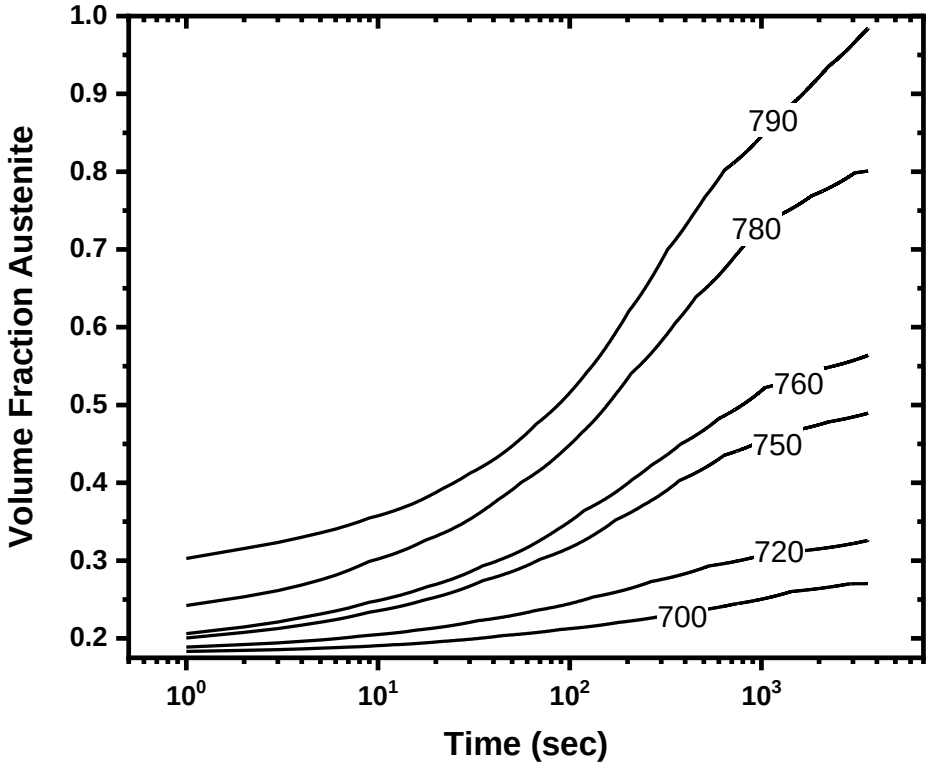

Figure 5.32: Volume fraction Austenite before cooling with respect to IA temperature and IA holding time.

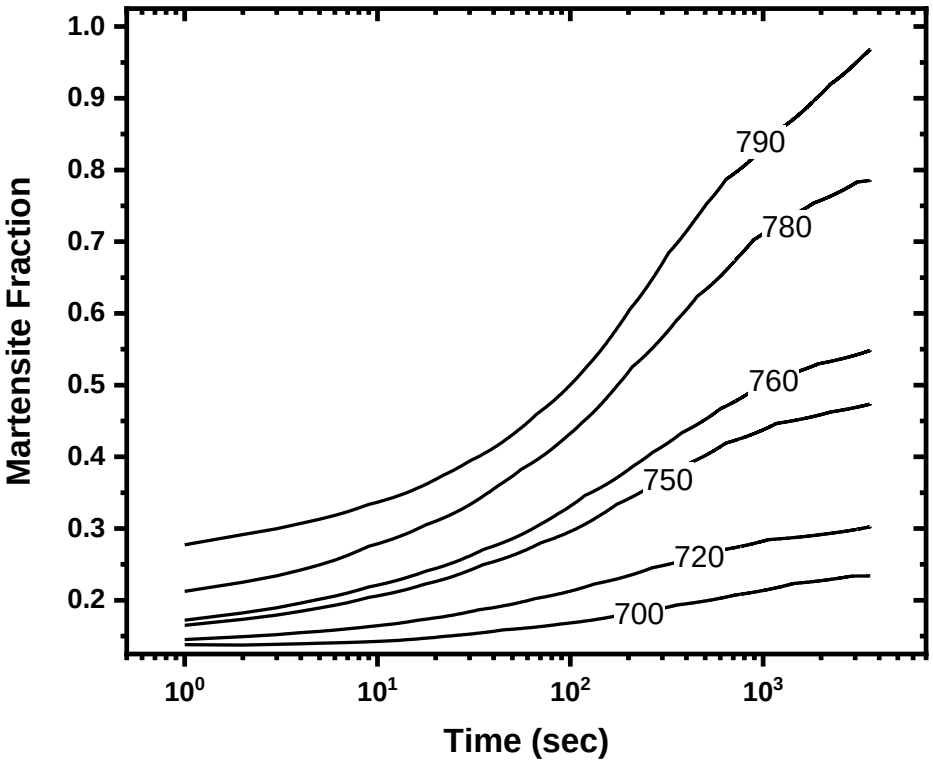

Figure 5.33: Volume fraction of martensite after quenching with respect to IA temperature and IA holding time.

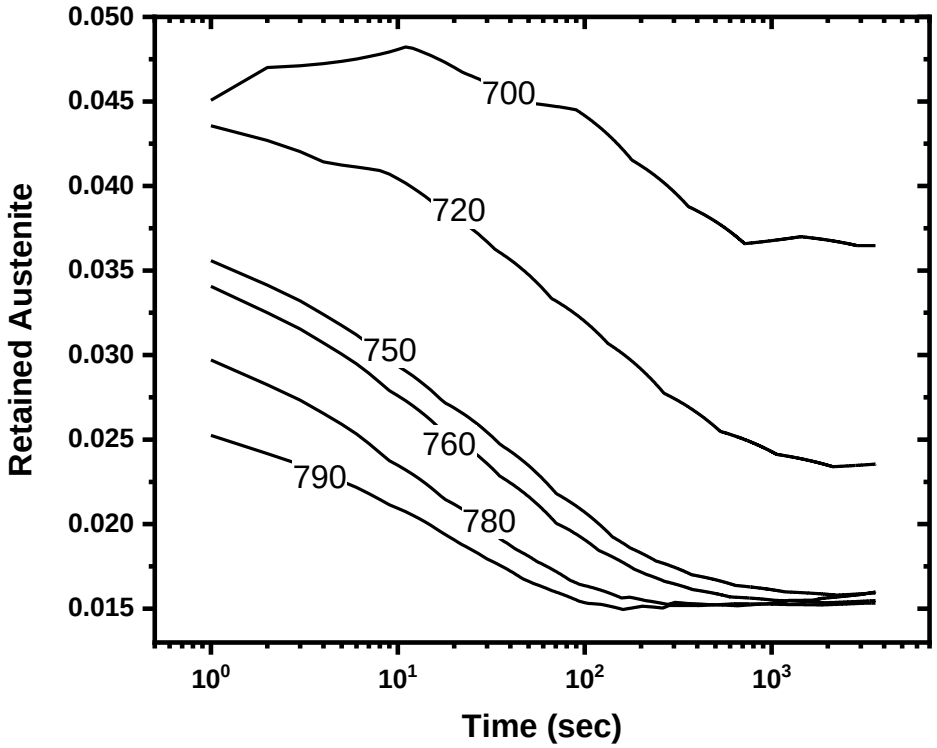

Figure 5.34: Volume fraction of Retained Austenite after quenching with respect to IA temperature and IA holding time.

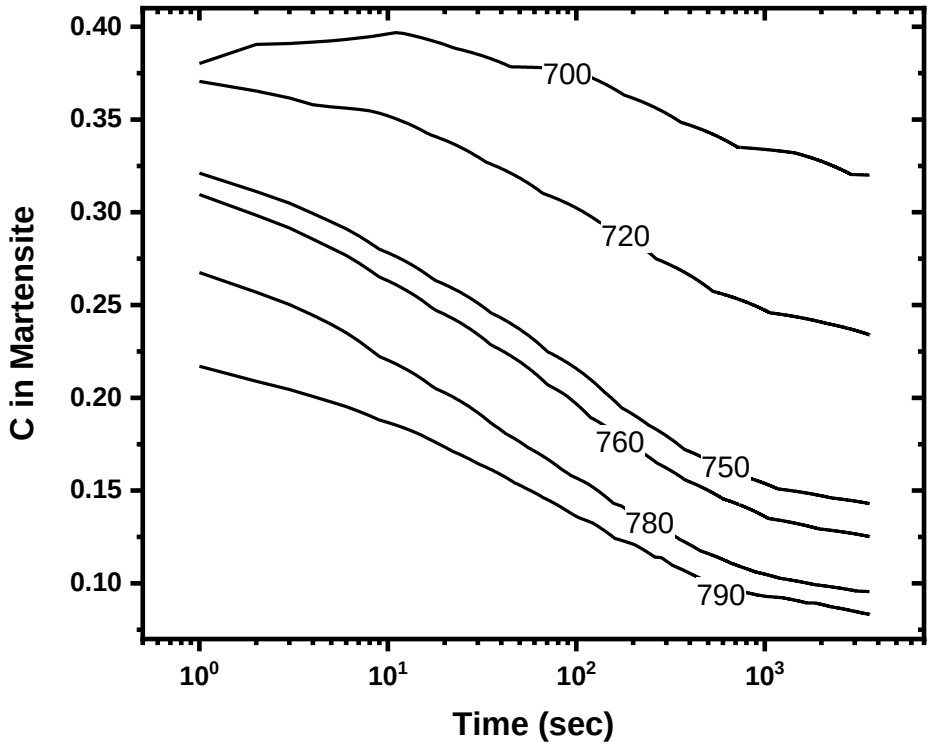

Figure 5.35: Carbon content in martensite with respect to IA time and IA temperature.

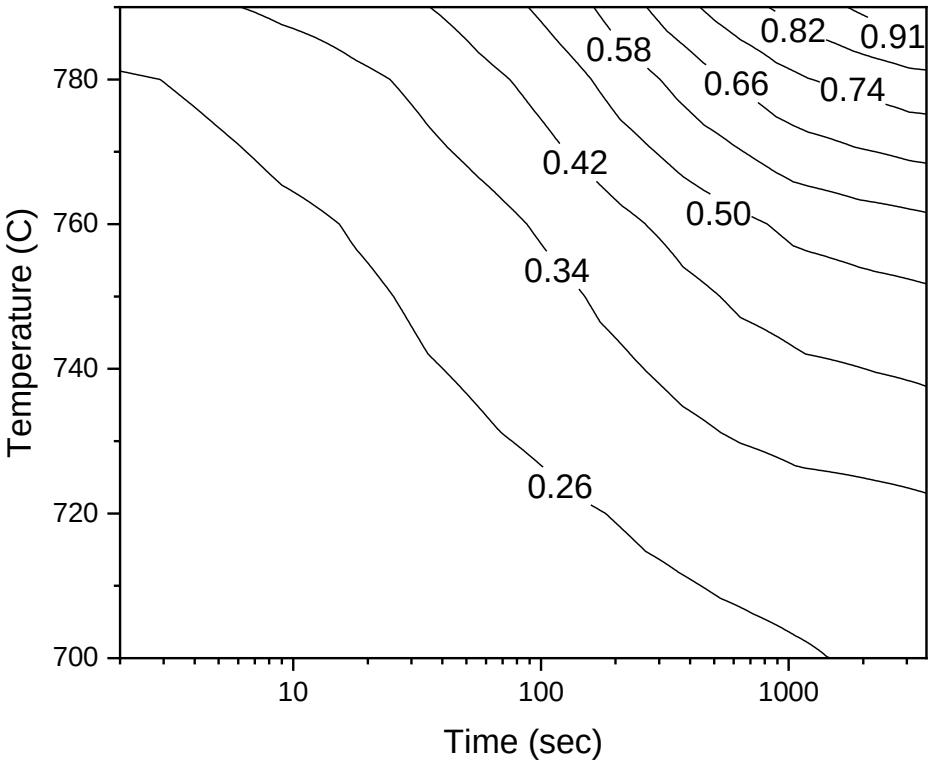

Figure 5.36: Mapping of Austenite volume fraction before cooling with respect to IA temperature and IA holding time

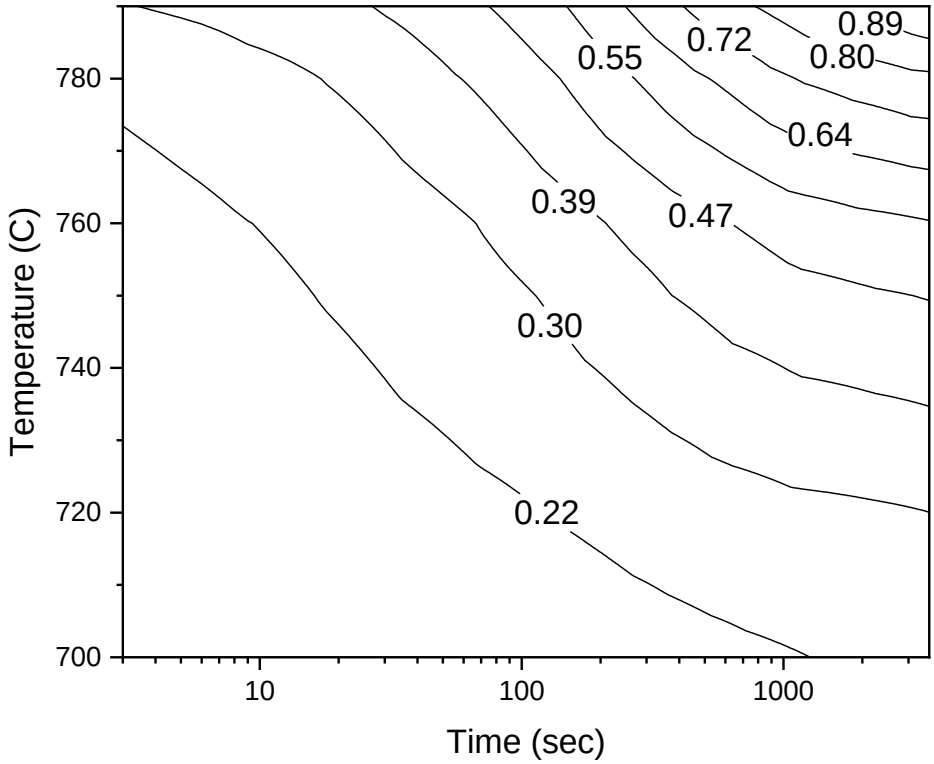

Figure 5.37: Mapping of martensite volume fraction after quenching with respect to IA temperature and IA holding time.

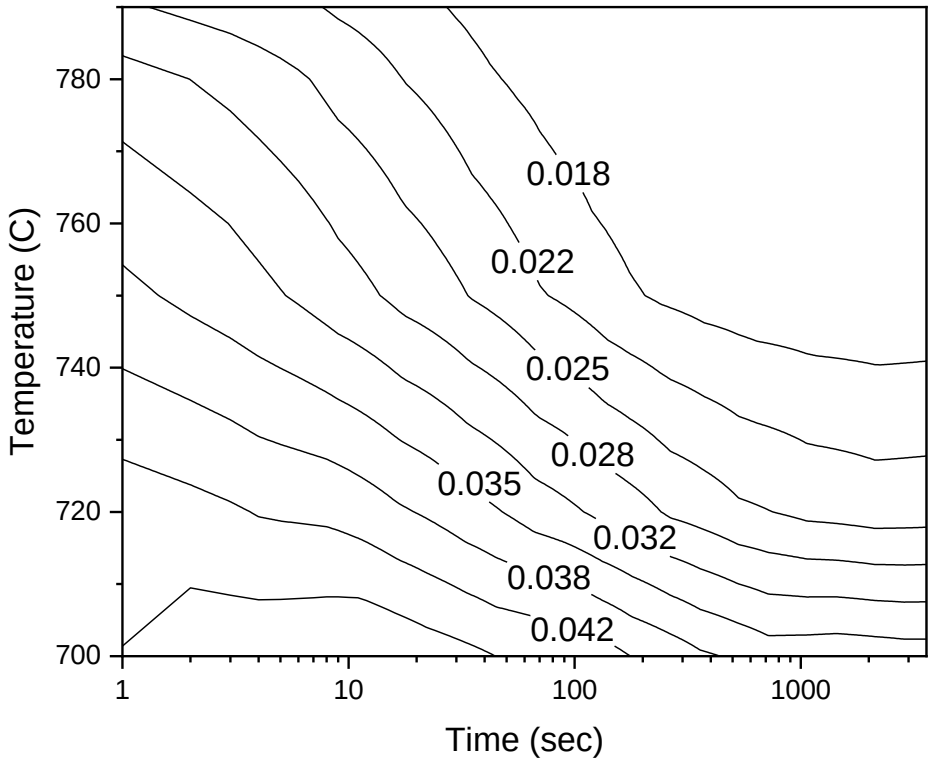

Figure 5.38: Mapping of Retained Austenite volume fraction after quenching with respect to IA temperature and IA holding time.

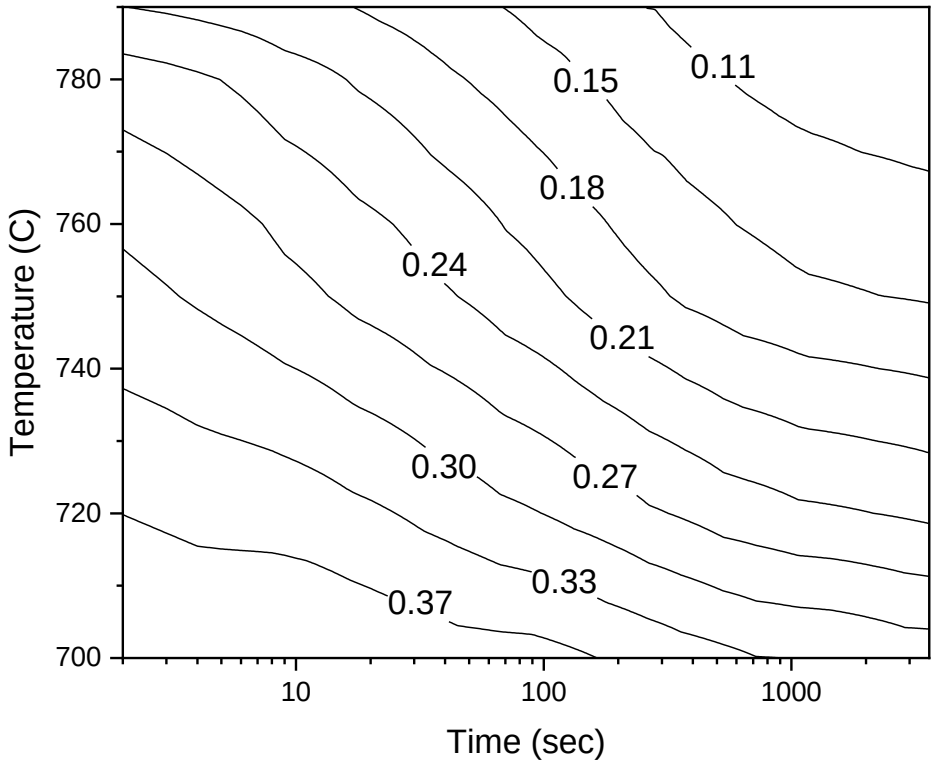

Figure 5.39: Mapping of carbon content in martensite with respect to IA time and IA temperature.

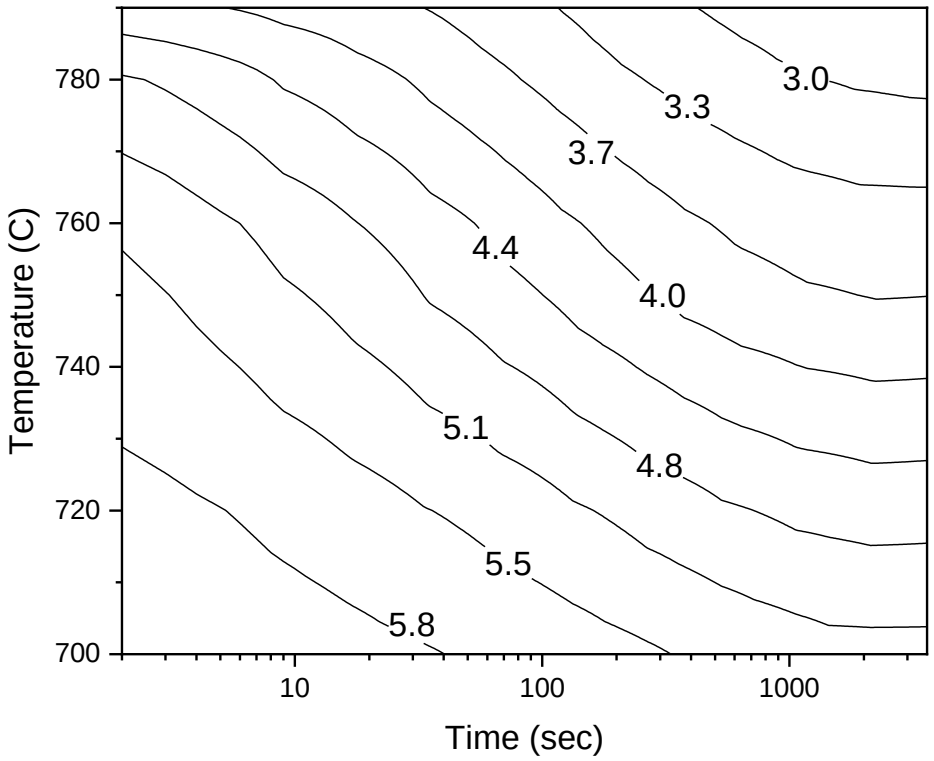

Figure 5.40: Mapping of Manganese content in martensite with respect to IA time and IA temperature

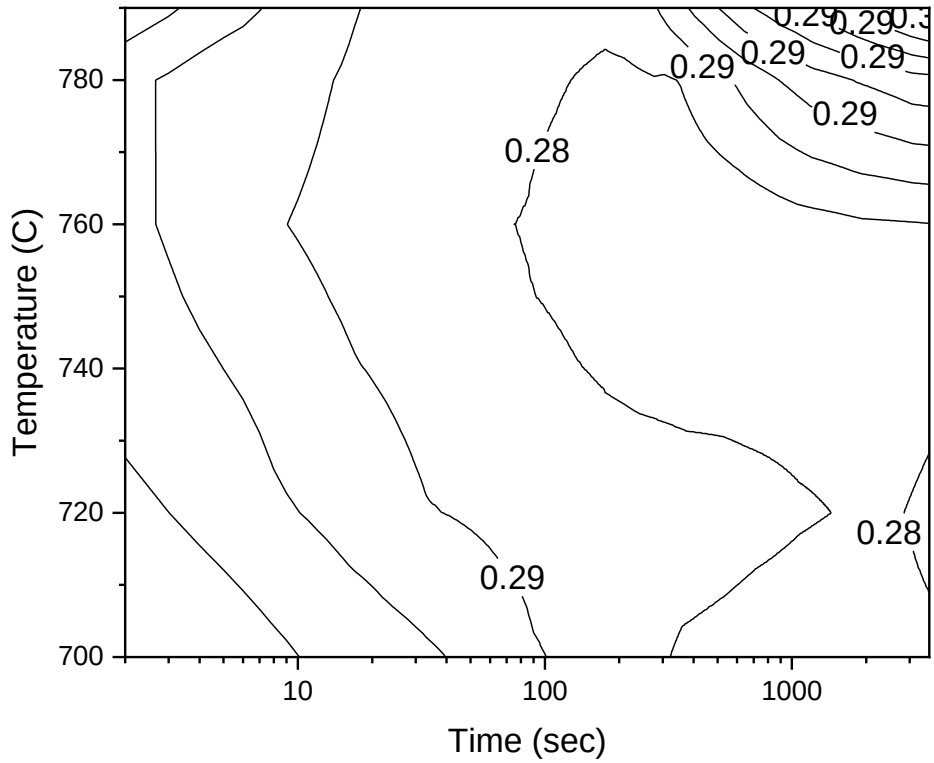

Figure 5.41: Mapping of Silicon content in martensite with respect to IA time and IA temperature

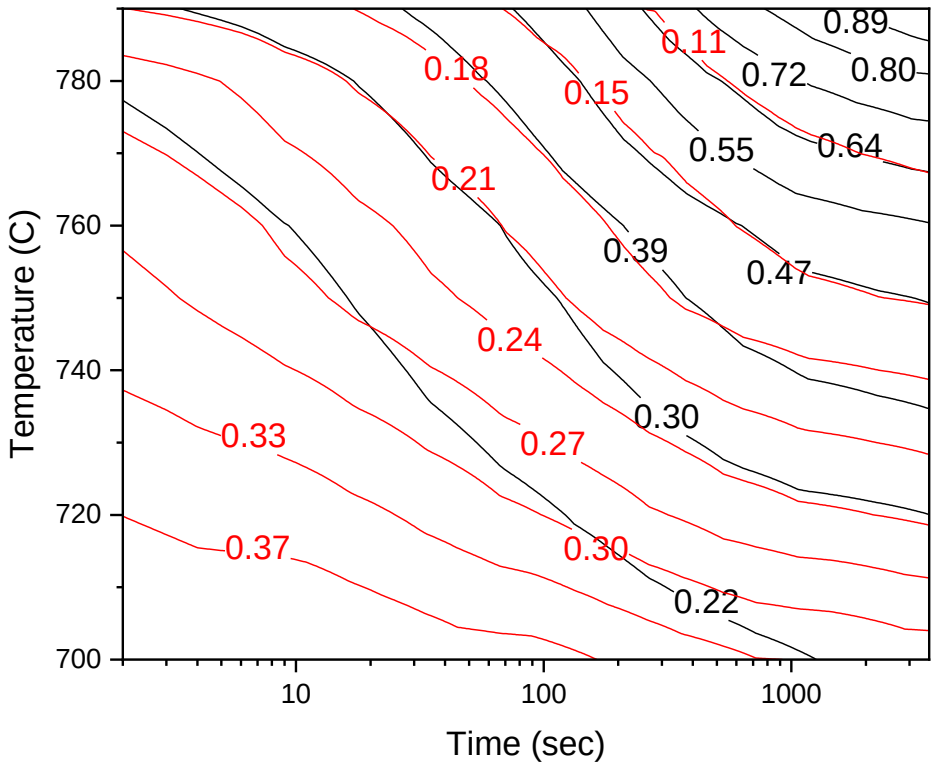

Figure 5.42: Mapping of martensite volume fraction (black lines) and carbon content in martensite (red lines) with respect to IA time and IA temperature for 3600 sec.

5.1Results for the 2nd Model ($\gamma_{\gamma+cem}$-α Model)

5.1.1 Computational kinetics Results for the 2nd Model ($\gamma_{\gamma+cem}$-α Model)

In the 2nd Model ($\gamma_{\gamma+cem}$-α Model), as in the 1st Model (γ-α Model), kinetic calculations of Intercritical Annealing of DP1000 steel were performed. The only effect to consider on the microstructure is the phase transformation from perlite-ferrite to austenite. Heating from room temperature to the intercritical annealing temperature in not considered in the model that was used and assumes the original microstructure as well as the initial conditions for the kinetic model, as conditions resulting from equilibrium calculations.

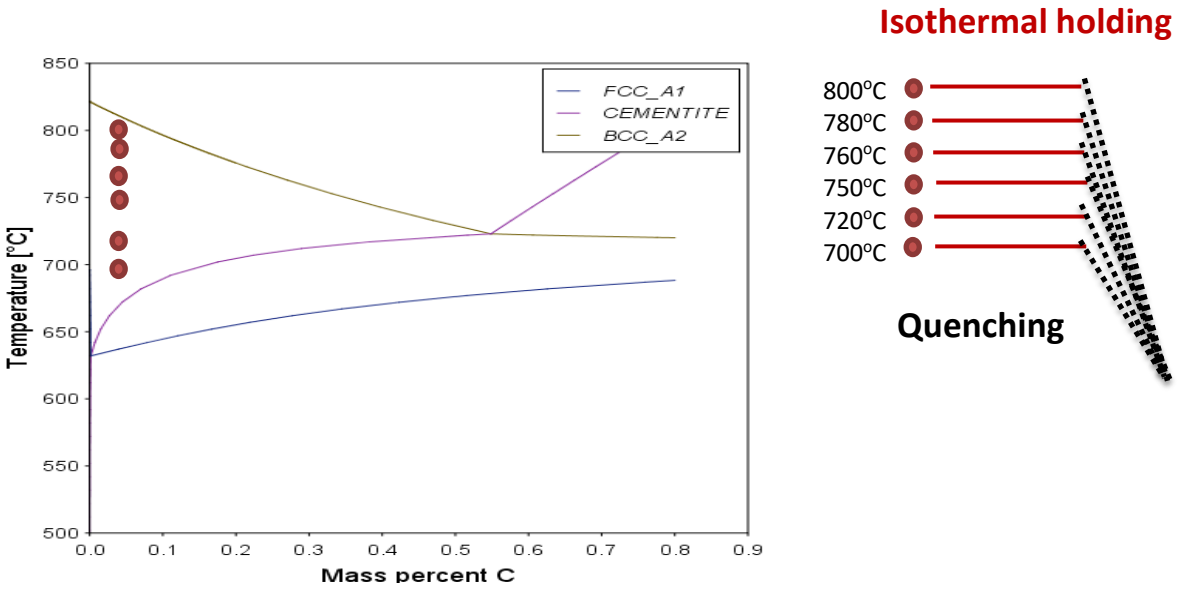

Figure 5.43: Isopleth diagram and heat treatment steps applied as an initial step IA and quenching

Intercritical annealing was performed for 3600sec and the kinetic model (DICTRA –MOBFE-2) resulted in austenite volume fraction for each IA temperature with respect to holding time. Below are depicted six different figures. Every figure is for the same IA holding but for different temperature. (a) Figure 5.44 depicts the austenite volume fraction for 800°C, Figure 5.44 (b) depicts the austenite volume fraction for 780°C and Figure 5.44 (c) for 760°C. Figure 5.44(d), Figure 5.44 (e), Figure 5.44 (f) depict the austenite volume fraction for 750°C 720°C and 700°C respectively. It is evident that during IA the austenite volume fraction increases with increasing holding time. Also, higher IA temperature leads to higher austenite volume fraction. For the above six temperatures the element profiles for Carbon, Manganese Silicon and Chromium were created and are presented in the next pages. In Table 5.2, that follows a small list providing a small description of the figures and the temperature as well as the element they were calculated for, is presented. This list is provided as a guideline for the following pages.

Table 5.2: List, providing a small description of the figures and the temperature and the element they were calculated for

Temperature	Carbon profile	Manganese profile	Chromium profile	Silicon profile
790°C	Figure 5.45	Figure 5.46	Figure 5.47	Figure 5.48
780°C	Figure 5.49	Figure 5.50	Figure 5.51	Figure 5.52
760°C	Figure 5.53	Figure 5.54	Figure 5.55	Figure 5.56
750°C	Figure 5.57	Figure 5.58	Figure 5.59	Figure 5.60
720°C	Figure 5.61	Figure 5.62	Figure 5.63	Figure 5.64
700°C	Figure 5.65	Figure 5.66	Figure 5.67	Figure 5.68

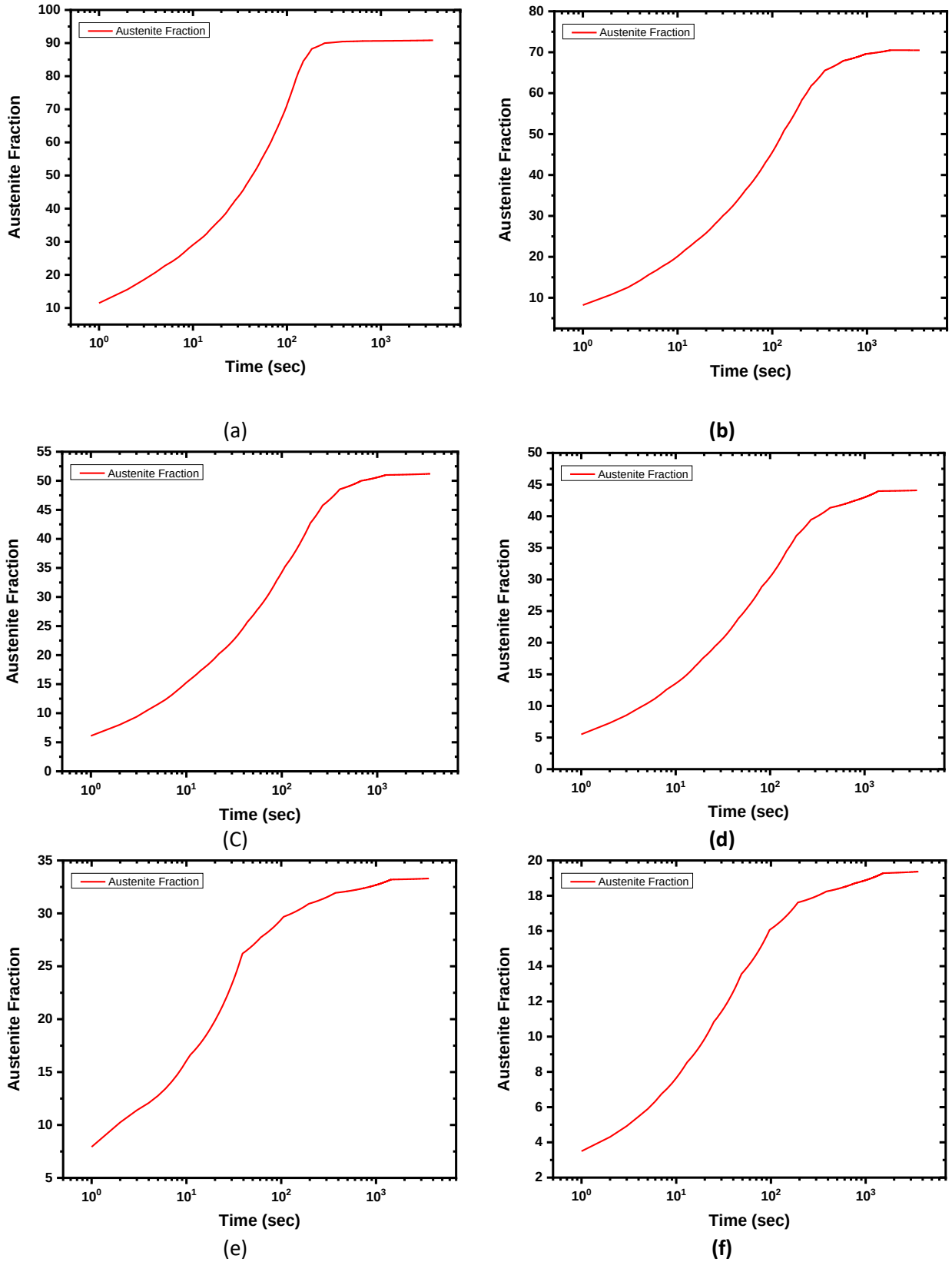

Figure 5.44: The evolution of austenite volume fraction for 800°C (a), 780°C (b), 760°C (c), 750°C (d) , 720°C (e) and for 700°C (f) versus time.

In Figure 5.45 the partitioning of Carbon during intercritical annealing of DP1000 at 800^{o}C for 0, 5, 30, 50, 150, 300, 500, 1500, 2500, 3600sec, is presented. Austenite is on left the and with progressing time at IA moves towards the right consuming the preexisting ferrite, thus increasing in size with progressing holding time. The starting concentration of austenite (γ) is enriched in carbon and becomes depleted with holding time. The starting concentration of ferrite (α) in carbon is much smaller than that of the initial austenite becomes even more depleted with holding time.

The carbon concentration profile in austenite is divided in three areas. The left furthermost side of γ gains its C content, from the initial highly enriched γ region at 0sec. This side, as holding time increases, C is lowered. On the right side, near the interface, γ gains the C content from the depletion of C from the neighboring ferrite. The middle area is enriched by both the left and right areas.

Figure 5.46 illustrates the partitioning of Manganese during intercritical annealing of DP1000 at 800^{o}C for the same holding times mentioned above. The Mn profile does not follow a similar behavior as in the case of carbon discussed previously. The Mn concentration profile in austenite is divided in two areas. The left furthermost side of γ gains its Mn content, from the initial highly enriched γ region at 0sec. On the right side, near the interface, γ gains the Mn content from the depletion of Mn from the neighboring ferrite. The middle area is missing in the case of MN partitioning.

Figure 5.47 presents the similarity in behavior between Cr and Mn. On the other hand, In contrast to Mn which tends to enrich austenite Silicon is depleted from austenite during IA holding as shown in the Figure 5.48. Higher intercritical annealing (IA) temperature leads to higher percentages of austenite and smooths out the profile of elements.

For this model the elemental profiles never smooth out.

Similar behavior is observed for the cases of the remaining IA temperatures. For IA at 780^{o}C the results are presented in Figure 5.49 to Figure 5.52. For IA at 760^{o}C the results are presented in Figure 5.53 to Figure 5.56. For IA at 750^{o}C the results are presented in Figure 5.57 to Figure 5.60. For IA at 720^{o}C the results are presented in Figure 5.61to Figure 5.64. Finally, for IA at 700^{o}C the results are presented in Figure 5.65 to Figure 5.68.

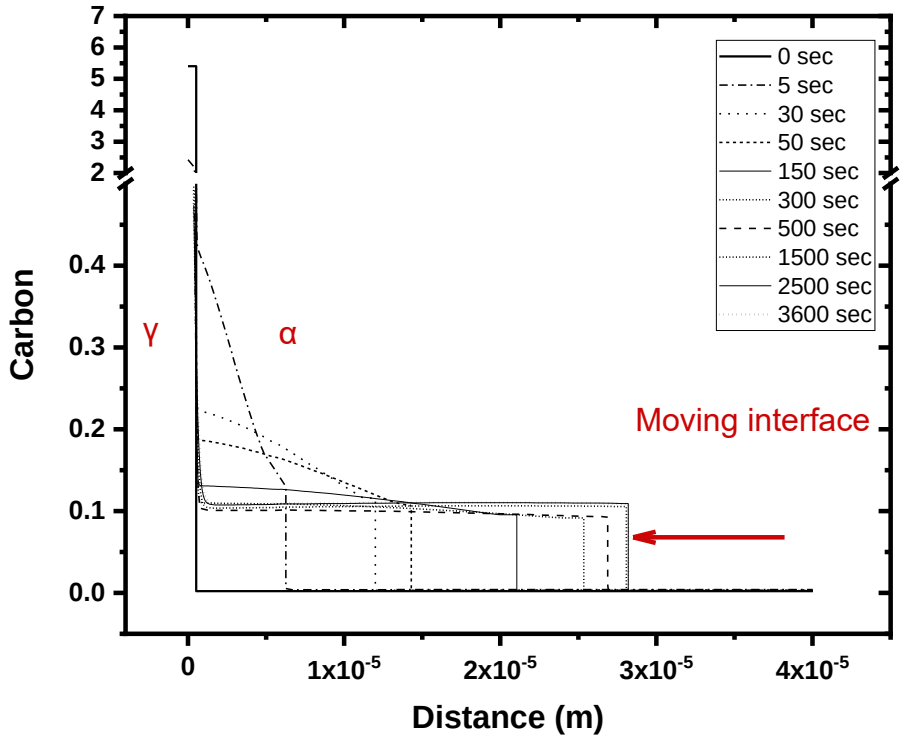

Figure 5.45: Partitioning of Carbon during intercritical annealing of DP1000 at 800°C for 0, 5, 30, 50, 150, 300, 500, 1500, 2500, 3600sec. Austenite is on left the and with progressing time at IA moves towards the right consuming preexisting ferrite.

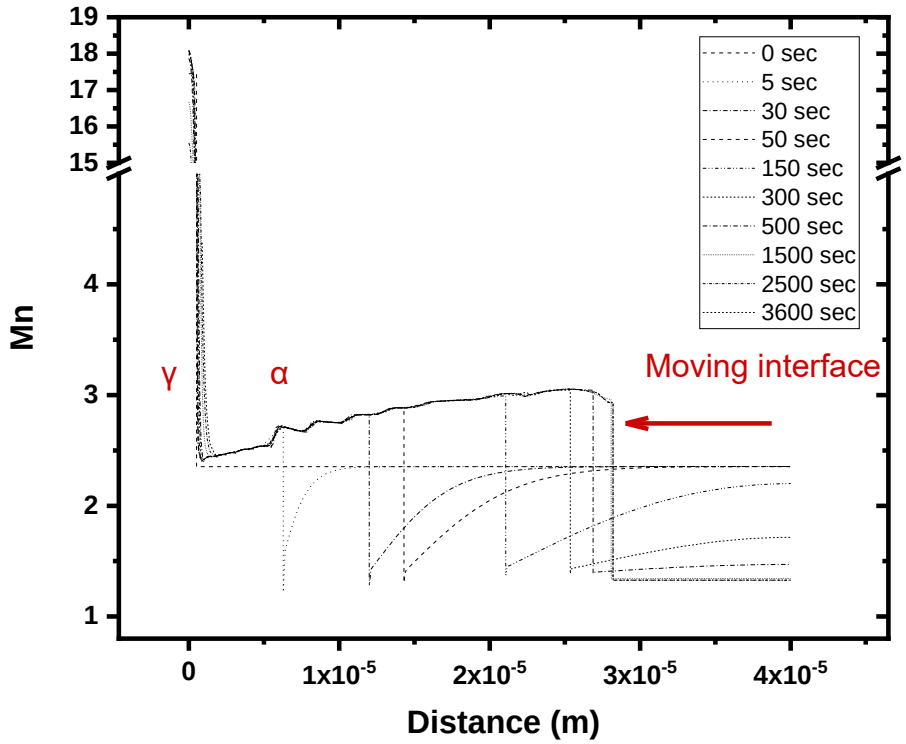

Figure 5.46: Partitioning of Manganese during intercritical annealing of DP1000 at 800°C for 0, 5, 30, 50, 150, 300, 500, 1500, 2500, 3600sec.

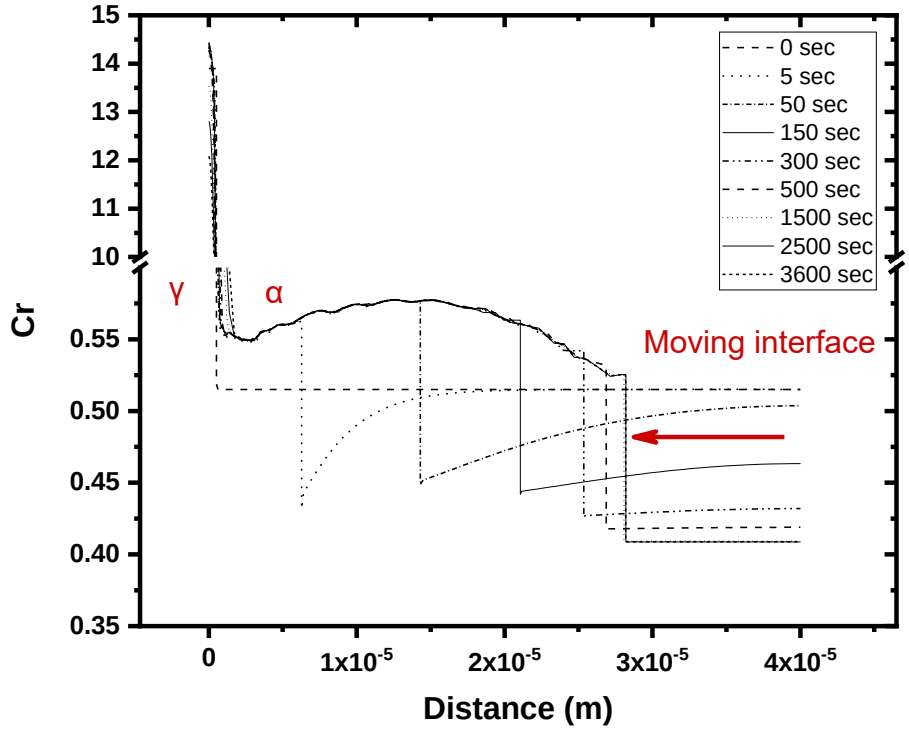

Figure 5.47: Partitioning of Chromium during intercritical annealing of DP1000 at 800°C for 0, 5, 30, 50, 150, 300, 500, 1500, 2500, 3600sec.

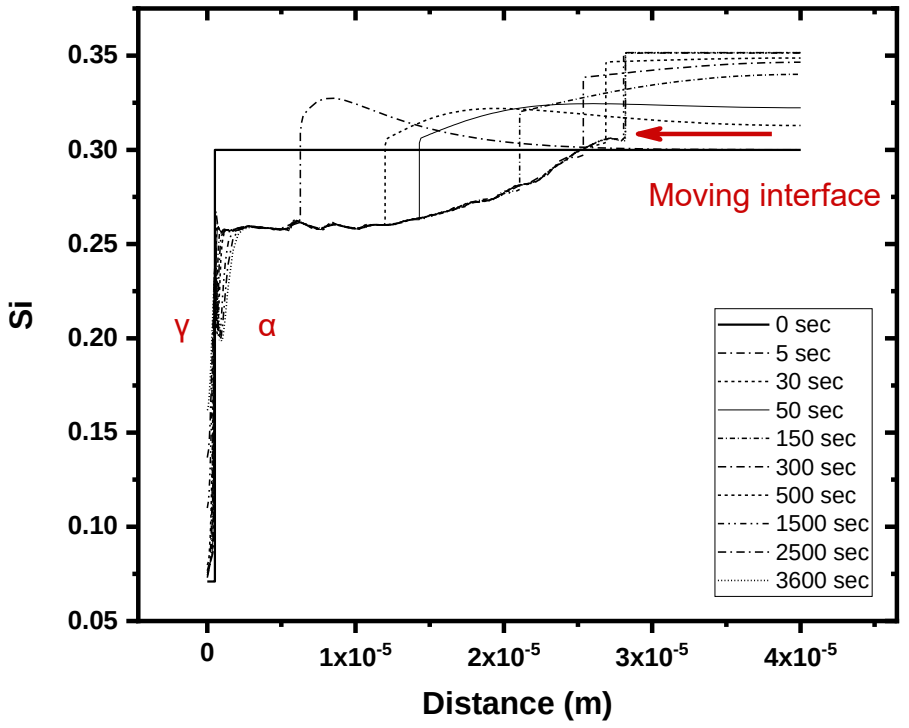

Figure 5.48: Partitioning of Silicon during intercritical annealing of DP1000 at 800°C for 0, 5, 30, 50, 150, 300, 500, 1500, 2500, 3600sec.

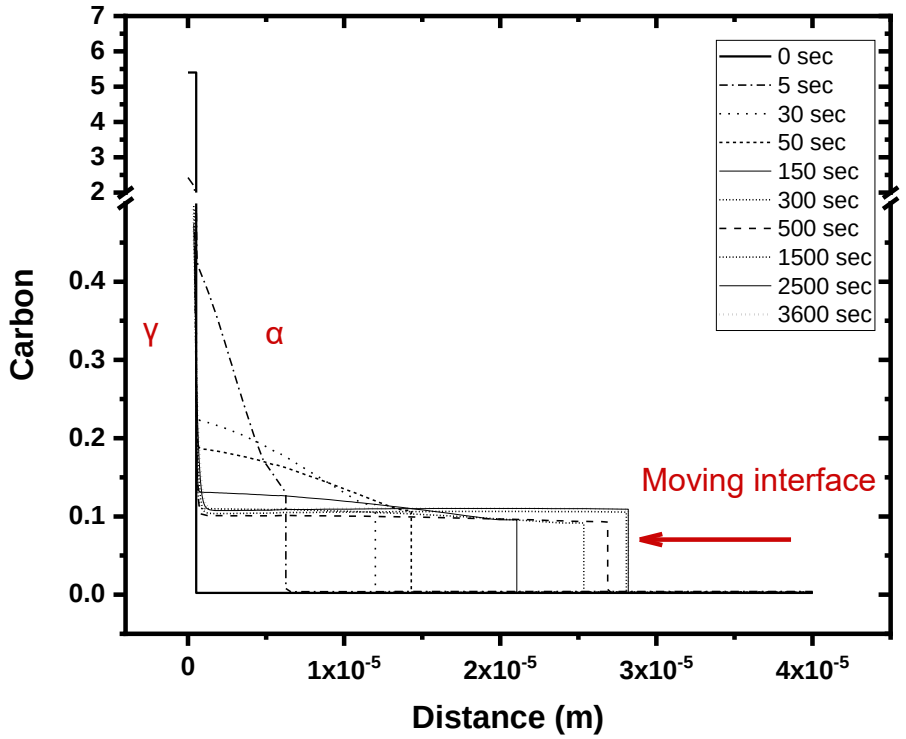

Figure 5.49: Partitioning of Carbon during intercritical annealing of DP1000 at 780°C for 0, 5, 30, 50, 150, 300, 500, 1500, 2500, 3600sec. Austenite is on left the and with progressing time at IA moves towards the right consuming preexisting ferrite.

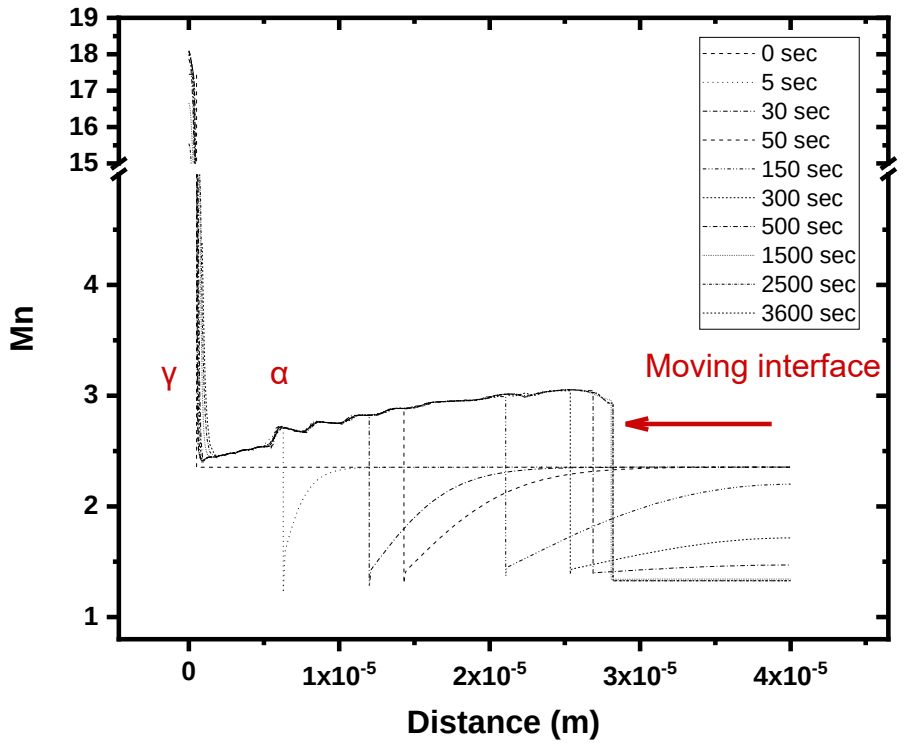

Figure 5.50: Partitioning of Manganese during intercritical annealing of DP1000 at 780°C for 0, 5, 30, 50, 150, 300, 500, 1500, 2500, 3600sec.

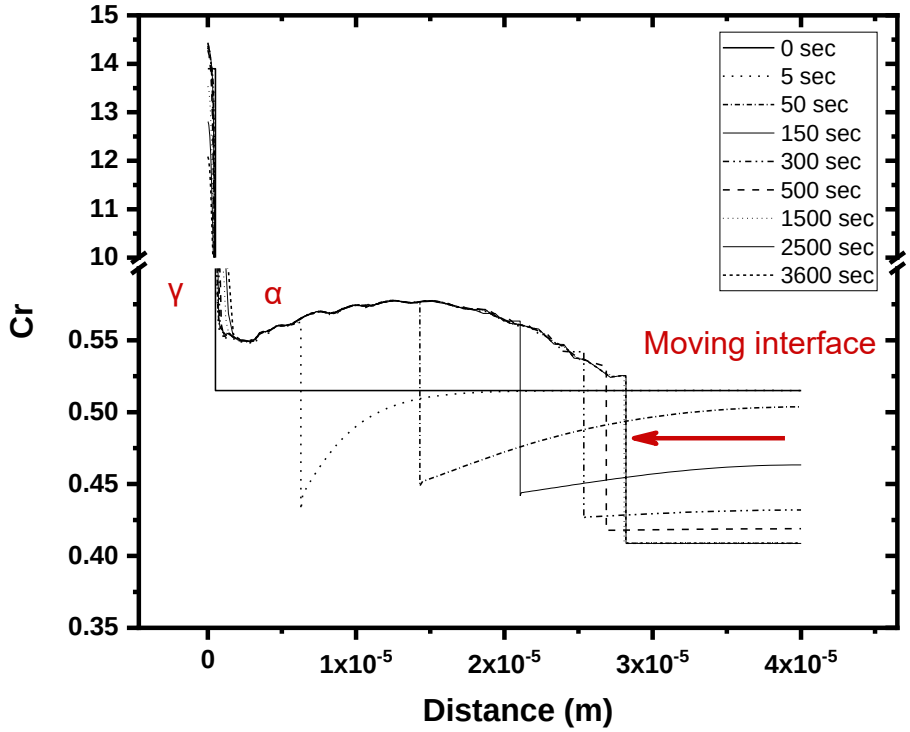

Figure 5.51: Partitioning of Chromium during intercritical annealing of DP1000 at 780°C for 0, 5, 30, 50, 150, 300, 500, 1500, 2500, 3600sec.

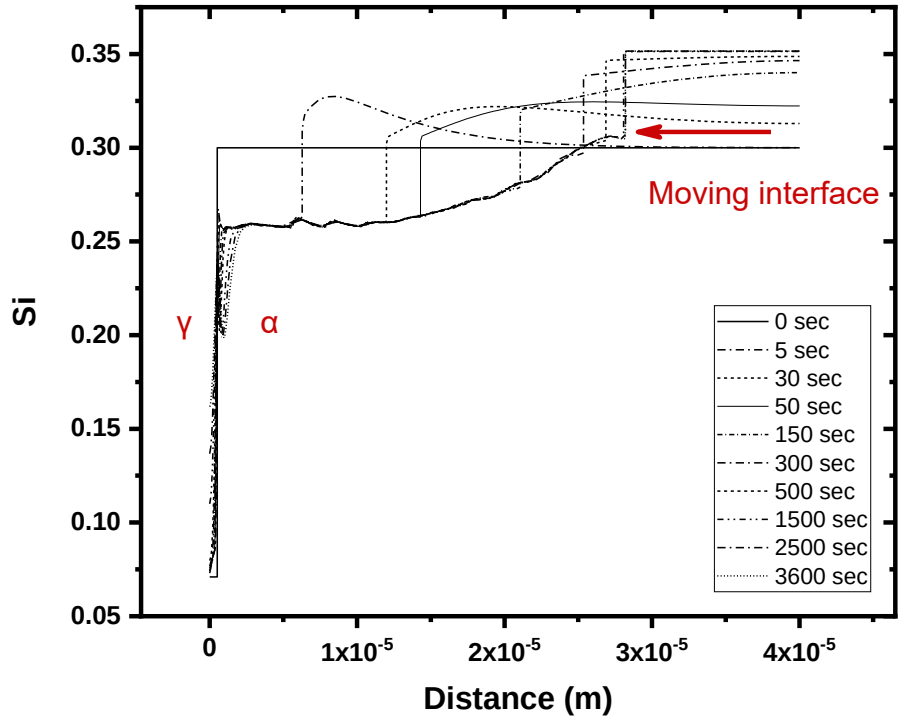

Figure 5.52: Partitioning of Silicon during intercritical annealing of DP1000 at 780°C for 0, 5, 30, 50, 150, 300, 500, 1500, 2500, 3600sec.

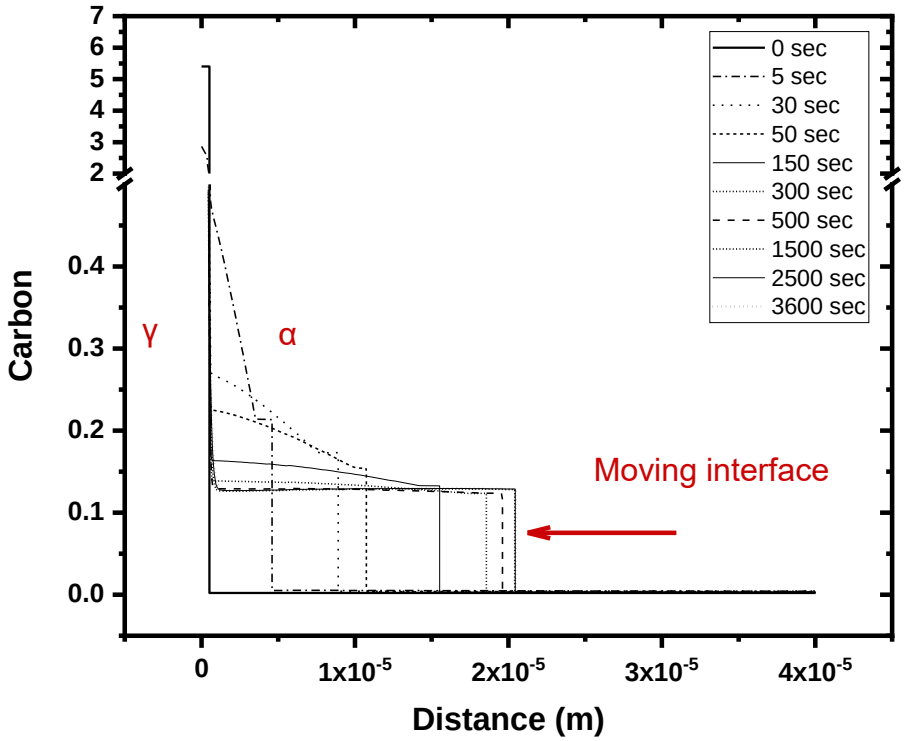

Figure 5.53: Partitioning of Carbon during intercritical annealing of DP1000 at 760°C for 0, 5, 30, 50, 150, 300, 500, 1500, 2500, 3600sec. Austenite is on left the and with progressing time at IA moves towards the right consuming preexisting ferrite.

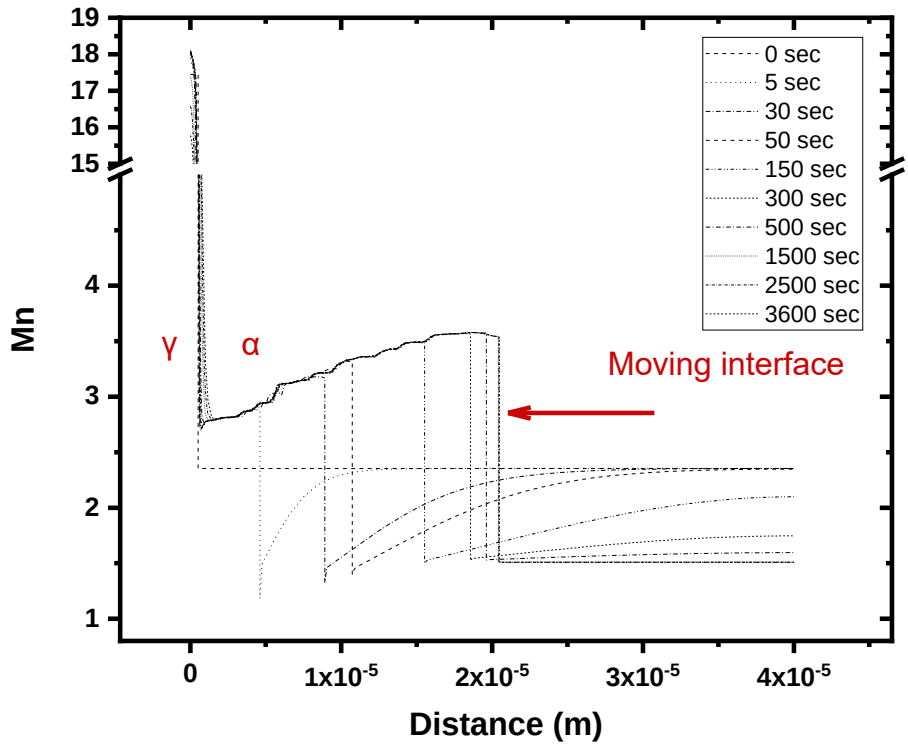

Figure 5.54: Partitioning of Manganese during intercritical annealing of DP1000 at 760°C for 0, 5, 30, 50, 150, 300, 500, 1500, 2500, 3600sec.

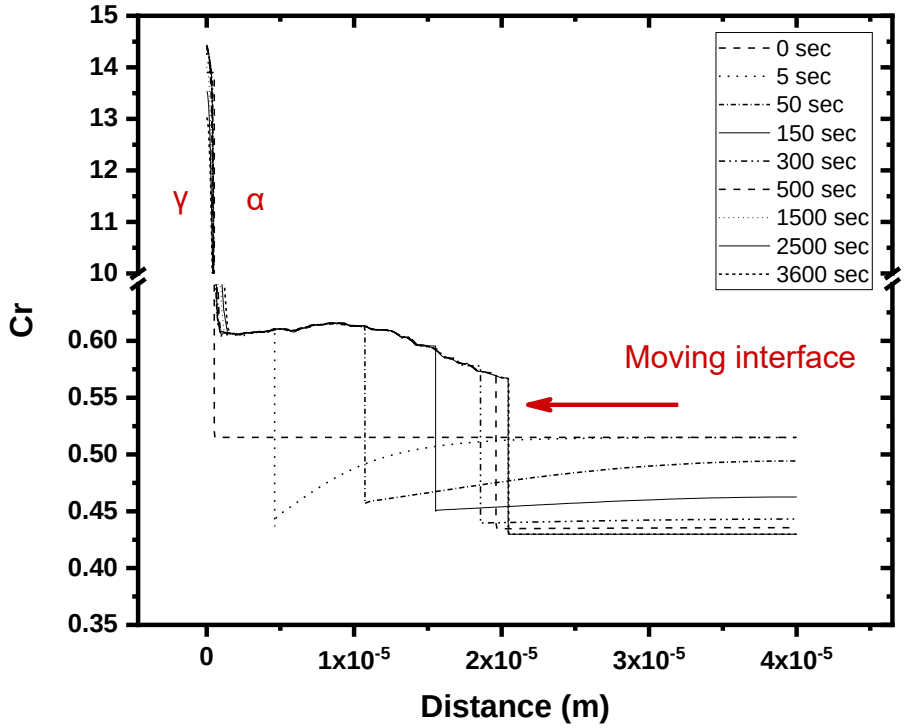

Figure 5.55: Partitioning of Chromium during intercritical annealing of DP1000 at 760°C for 0, 5, 30, 50, 150, 300, 500, 1500, 2500, 3600sec.

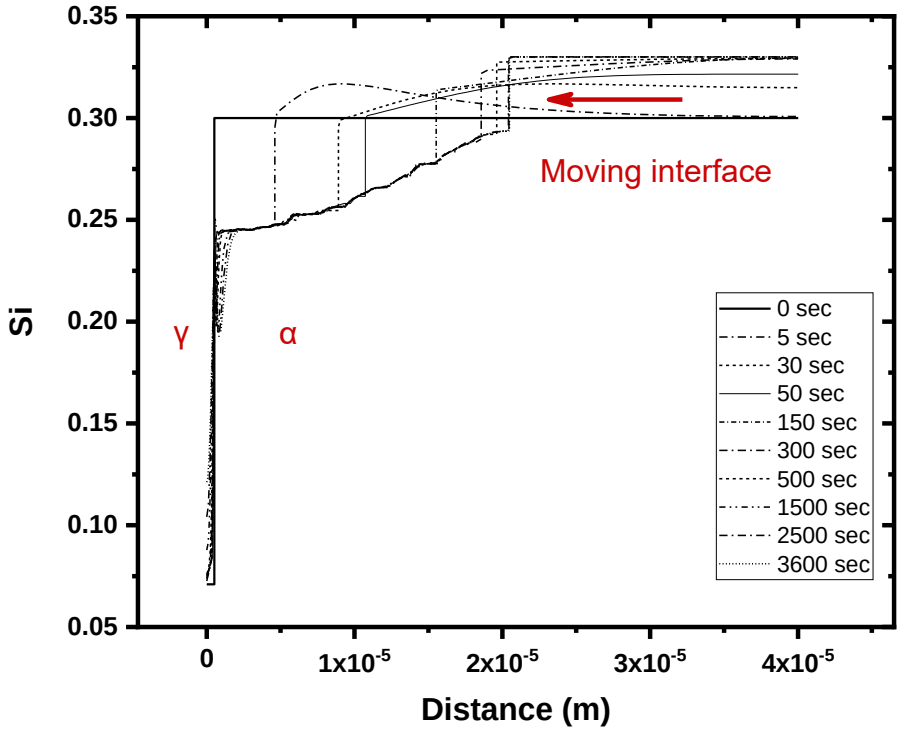

Figure 5.56: Partitioning of Silicon during intercritical annealing of DP1000 at 760°C for 0, 5, 30, 50, 150, 300, 500, 1500, 2500, 3600sec

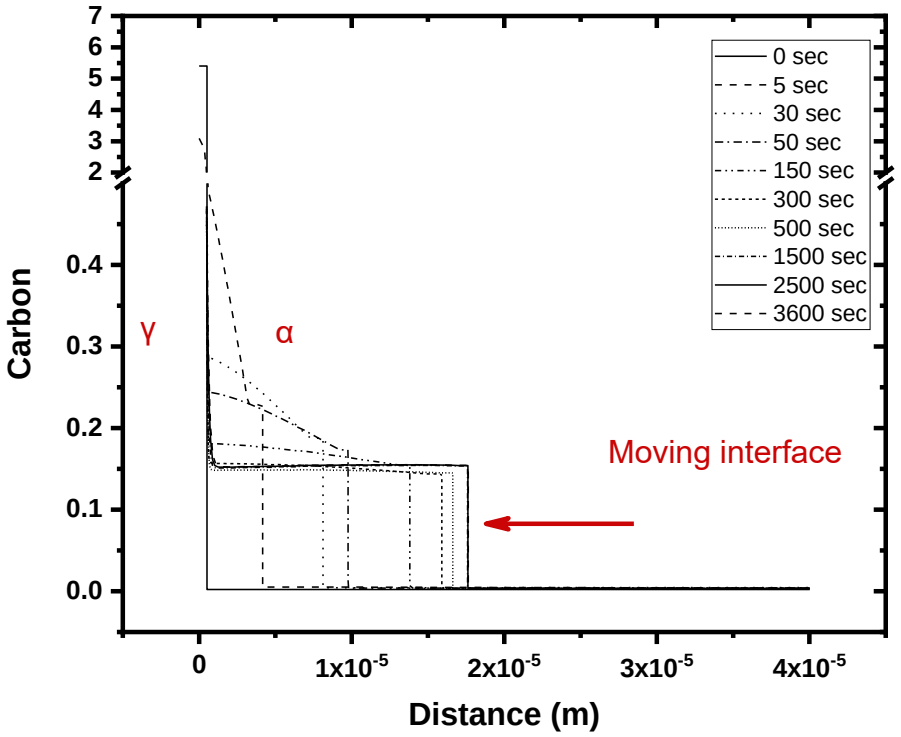

Figure 5.57: Partitioning of Carbon during intercritical annealing of DP1000 at 750°C for 0, 5, 30, 50, 150, 300, 500, 1500, 2500, 3600sec.

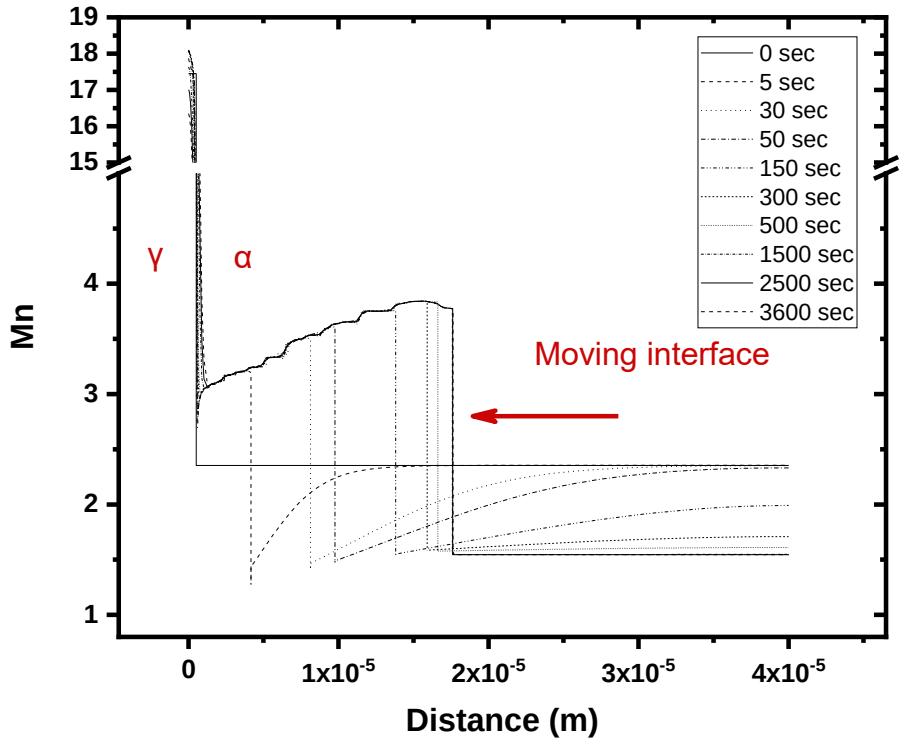

Figure 5.58: Partitioning of Manganese during intercritical annealing of DP1000 at 750°C for 0, 5, 30, 50, 150, 300, 500, 1500, 2500, 3600sec.

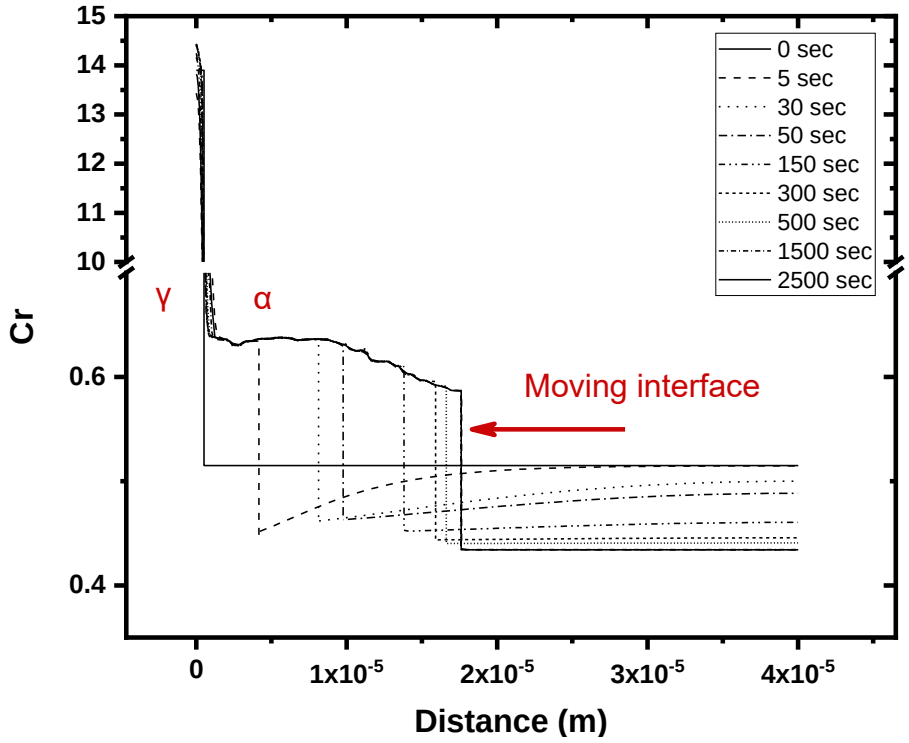

Figure 5.59: Partitioning of Chromium during intercritical annealing of DP1000 at 750°C for 0, 5, 30, 50, 150, 300, 500, 1500, 2500, 3600sec.

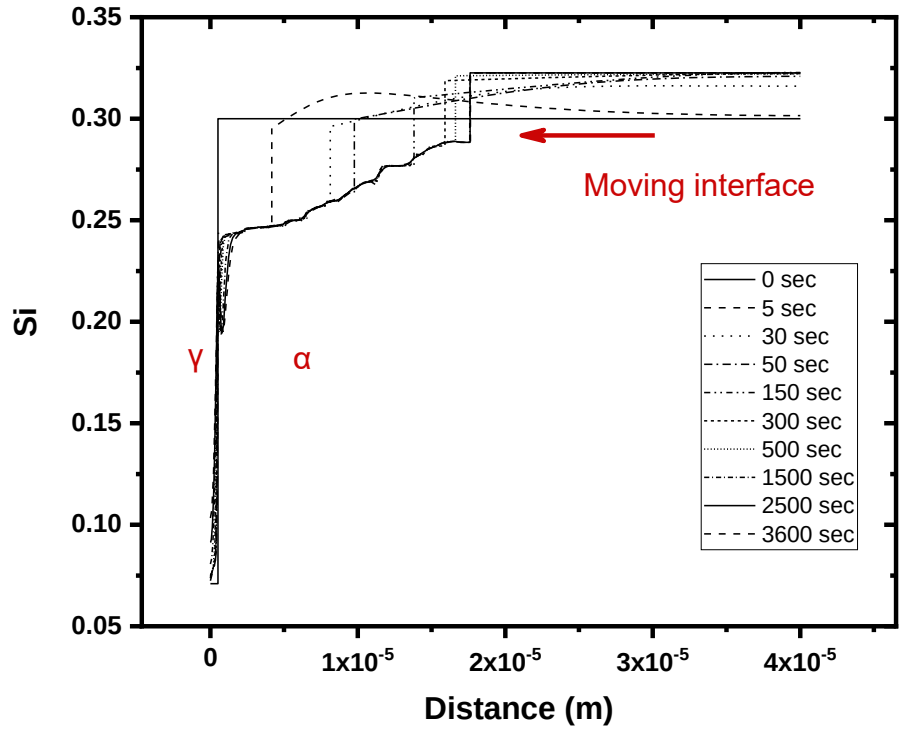

Figure 5.60: Partitioning of Silicon during intercritical annealing of DP1000 at 750°C for 0, 5, 30, 50, 150, 300, 500, 1500, 2500, 3600sec.

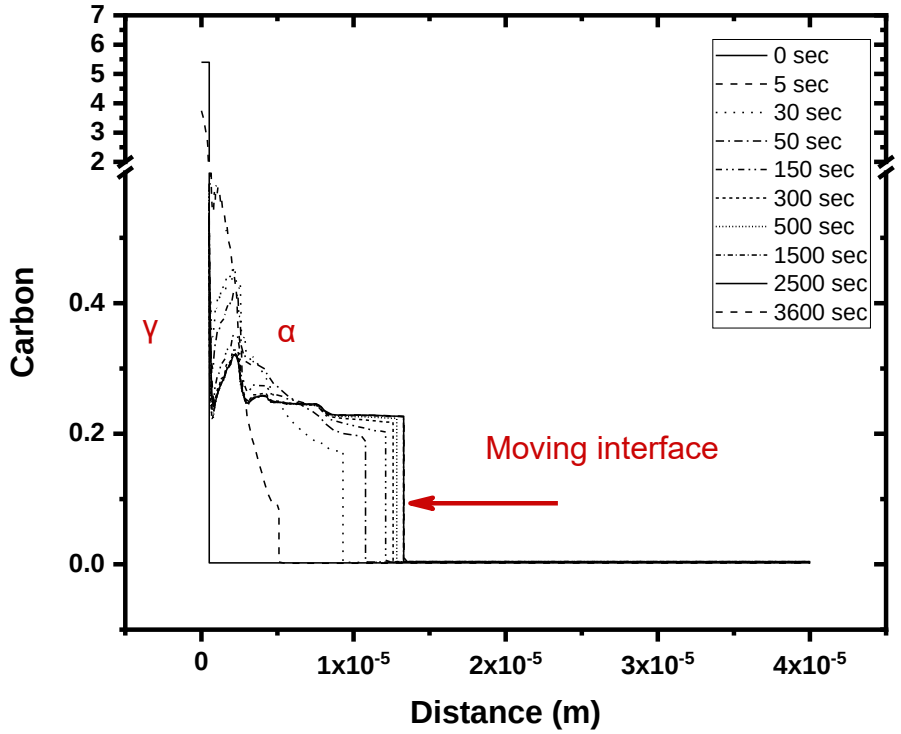

Figure 5.61: Partitioning of Carbon during intercritical annealing of DP1000 at 720°C for 0, 5, 30, 50, 150, 300, 500, 1500, 2500, 3600sec.

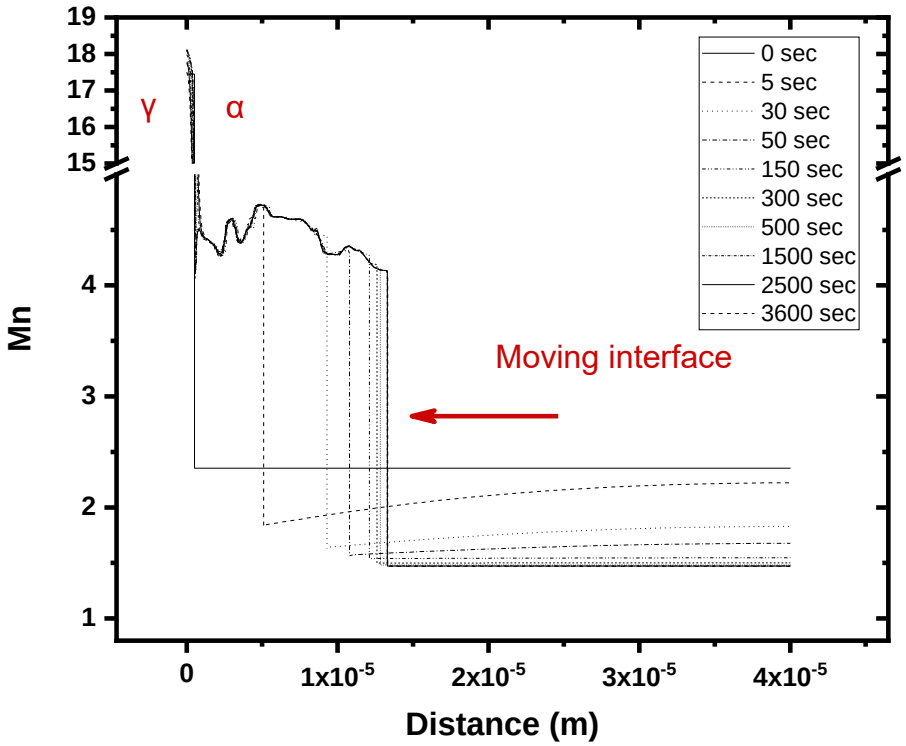

Figure 5.62: Partitioning of Manganese during intercritical annealing of DP1000 at 720°C for 0, 5, 30, 50, 150, 300, 500, 1500, 2500, 3600sec.

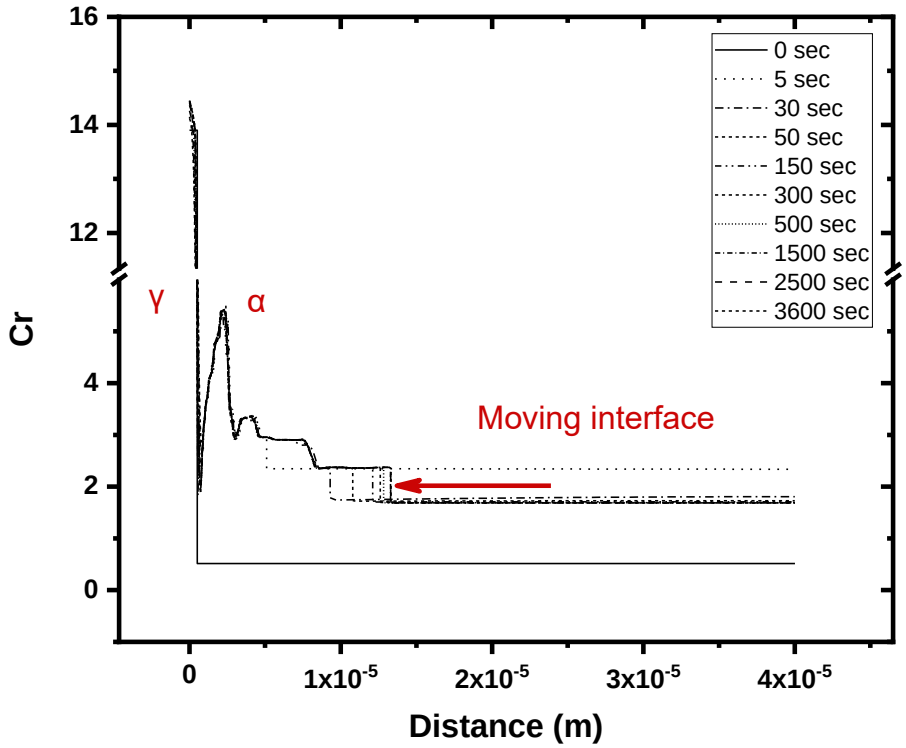

Figure 5.63: Partitioning of Chromium during intercritical annealing of DP1000 at 720°C for 0, 5, 30, 50, 150, 300, 500, 1500, 2500, 3600sec.

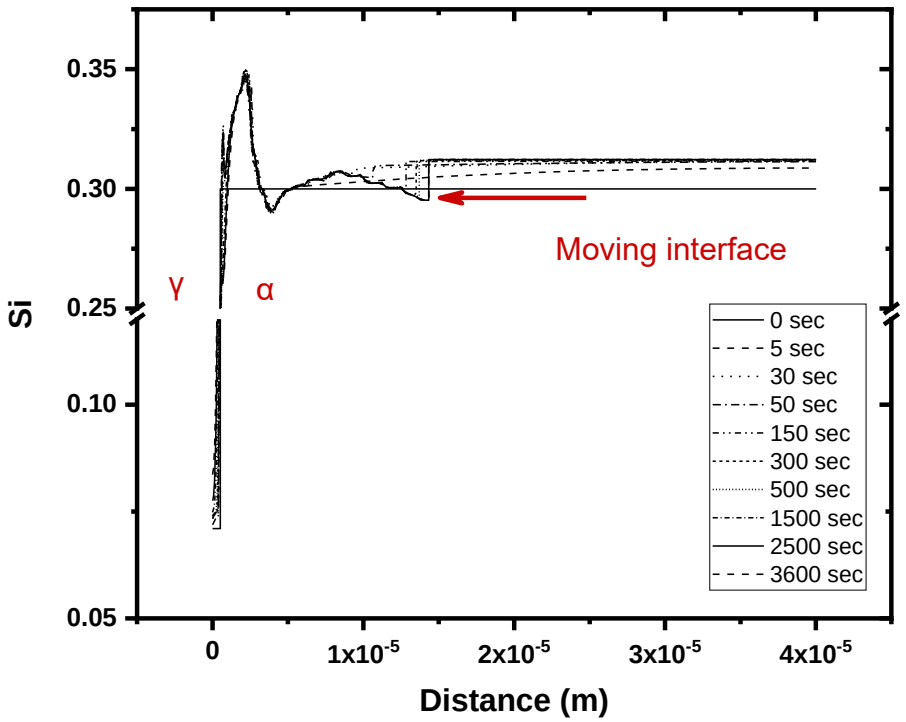

Figure 5.64: Partitioning of Silicon during intercritical annealing of DP1000 at 720°C for 0, 5, 30, 50, 150, 300, 500, 1500, 2500, 3600sec.

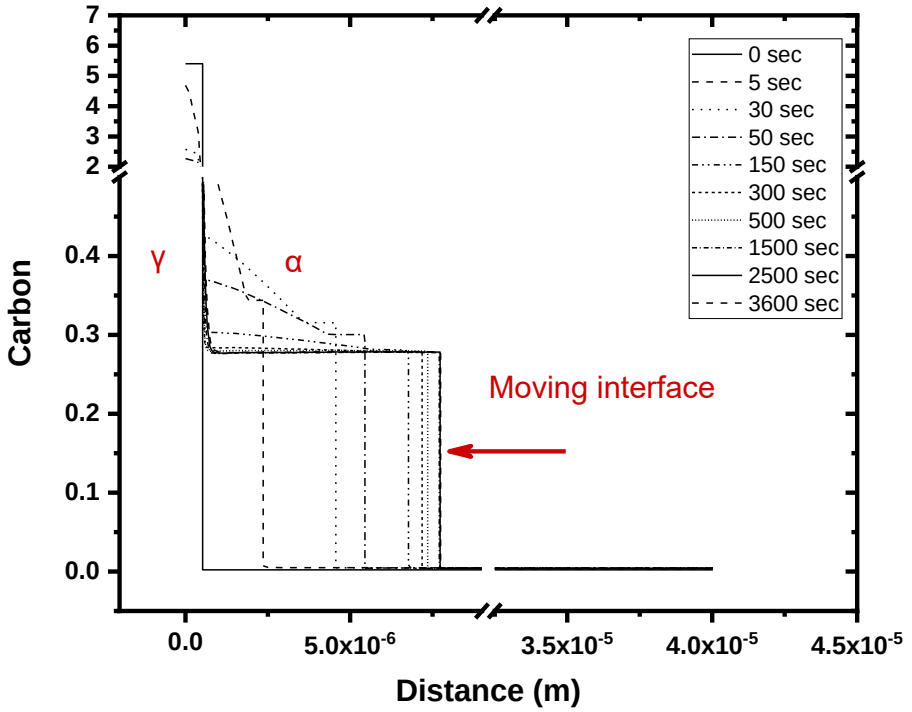

Figure 5.65: Partitioning of Carbon during intercritical annealing of DP1000 at 700°C for 0, 5, 30, 50, 150, 300, 500, 1500, 2500, 3600sec.

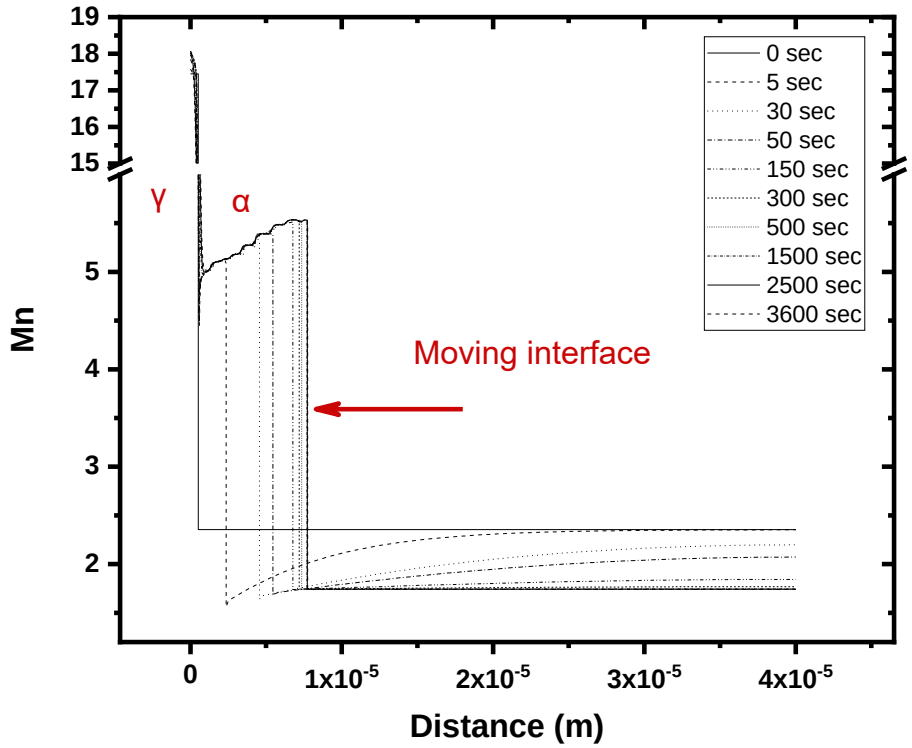

Figure 5.66: Partitioning of Manganese during intercritical annealing of DP1000 at 700°C for 0, 5, 30, 50, 150, 300, 500, 1500, 2500, 3600sec.

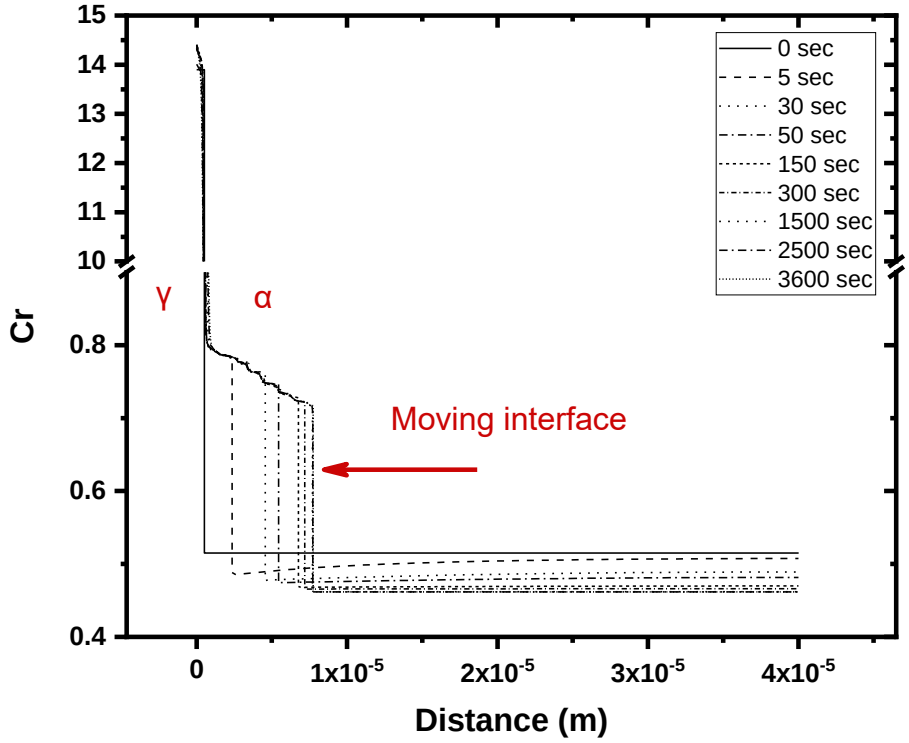

Figure 5.67: Partitioning of Chromium during intercritical annealing of DP1000 at 700°C for 0, 5, 30, 50, 150, 300, 500, 1500, 2500, 3600sec.

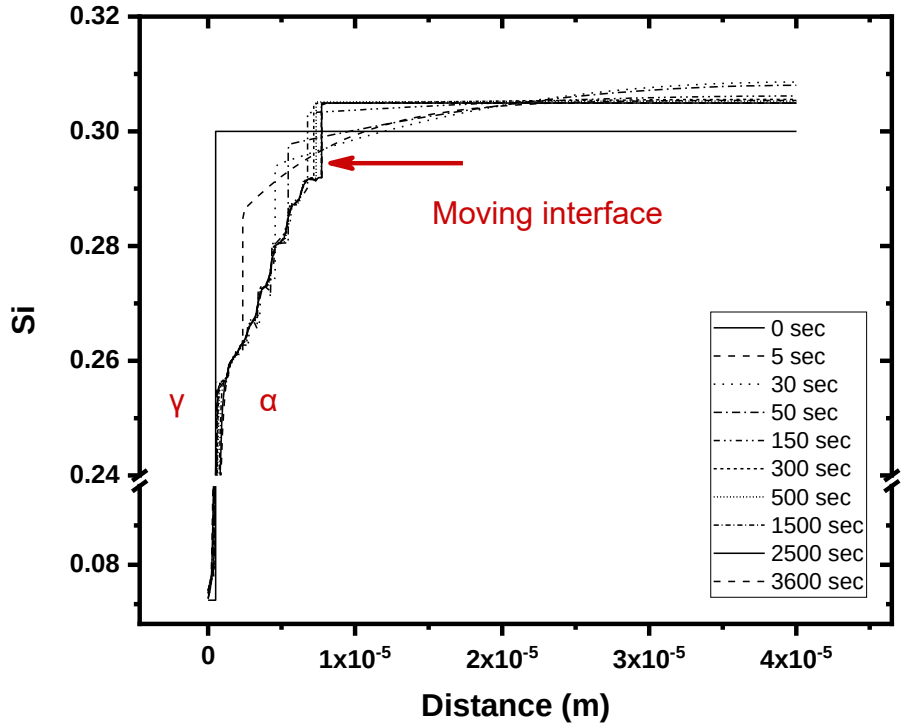

Figure 5.68: Partitioning of Silicon during intercritical annealing of DP1000 at 700°C for 0, 5, 30, 50, 150, 300, 500, 1500, 2500, 3600sec.

5.1.2 Results for Martensite formation for the 2nd Model ($\gamma_{\gamma+cem}$-α Model)

In the 2nd Model ($\gamma_{\gamma+cem}$-α Model) the same procedure was followed as reported in paragraph 5.2.2 . The figures that follow illustrate examples for IA at different temperatures. Figure **5**.**69** (a) and Figure **5**.**69**(b) depict the volume fraction of austenite (black dashed lines), martensite (black lines) and the volume fraction of retained austenite (red line) for IA at 800°C and 780°C respectively. The austenite volume fraction and the martensite volume fraction increase with increasing IA holding time as expected. Although it is expected that the volume fraction of retained austenite will decrease with the increase of IA holding time, it actually increases. Figure **5**.**70** (a), Figure **5**.**70** (b), Figure **5**.**71**(a) and Figure **5**.**71**(b) illustrate similar results for IA at 760°C, 750°C, 720°Cand 700°C respectively.

Figure **5**.**72** illustrates the Carbon content in martensite (red line), austenite (green line), retained austenite (black line) and ferrite (blue line) with respect to IA time, for IA at 800 °C (a), for IA at 780 °C (b), for IA at 760 °C (c), for IA at 750 °C (d), for IA at 720°C (e) and for IA at 700°C (f). Carbon is depleted from austenite, martensite and retained austenite. Carbon in ferrite has some fluctuations with the progression of intercritical annealing.

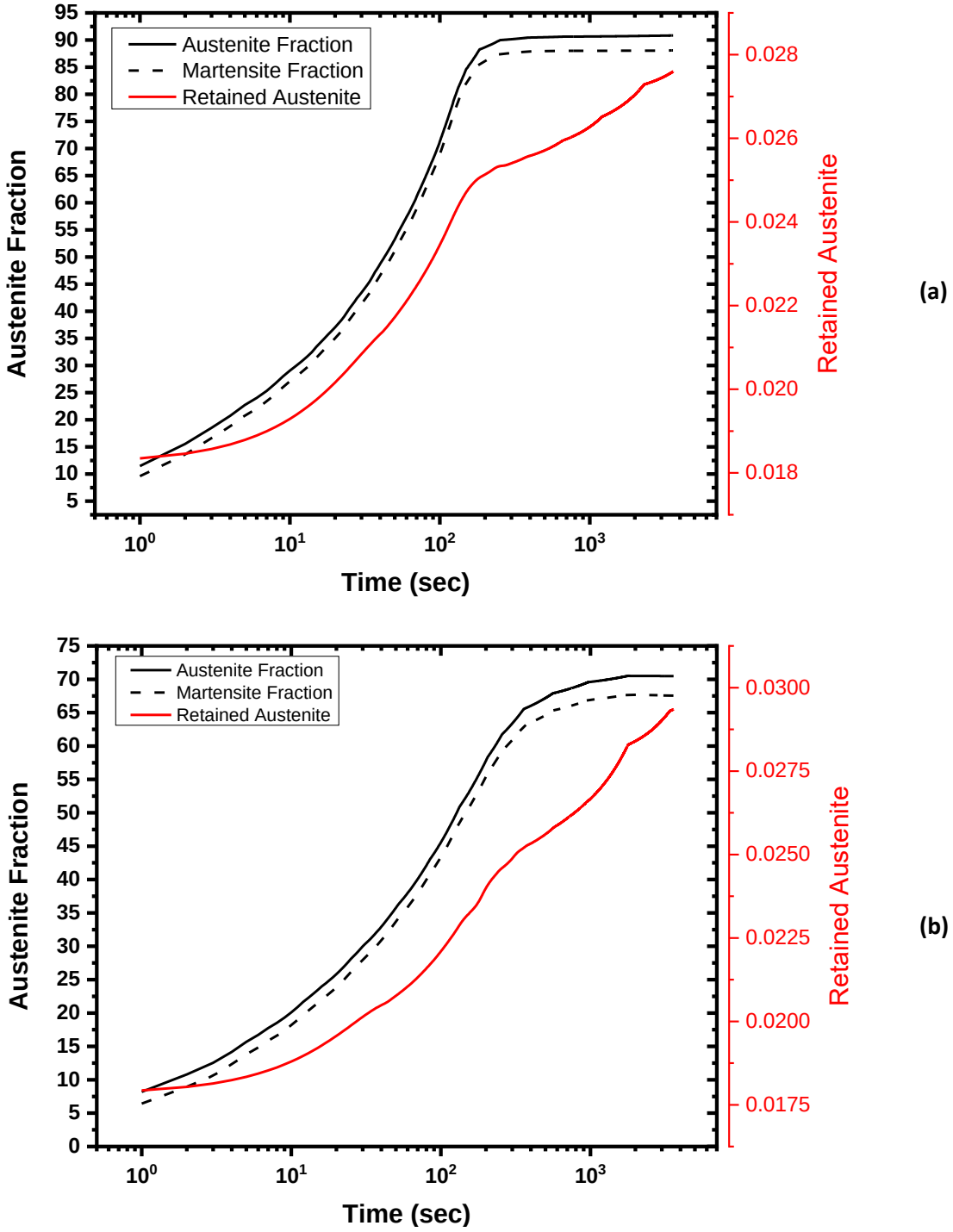

Figure 5.69: The volume fraction of austenite and martensite (black lines) and the volume fraction of retained austenite (red line) for IA at 800°C (a), 780°C (b), for 3600 sec.

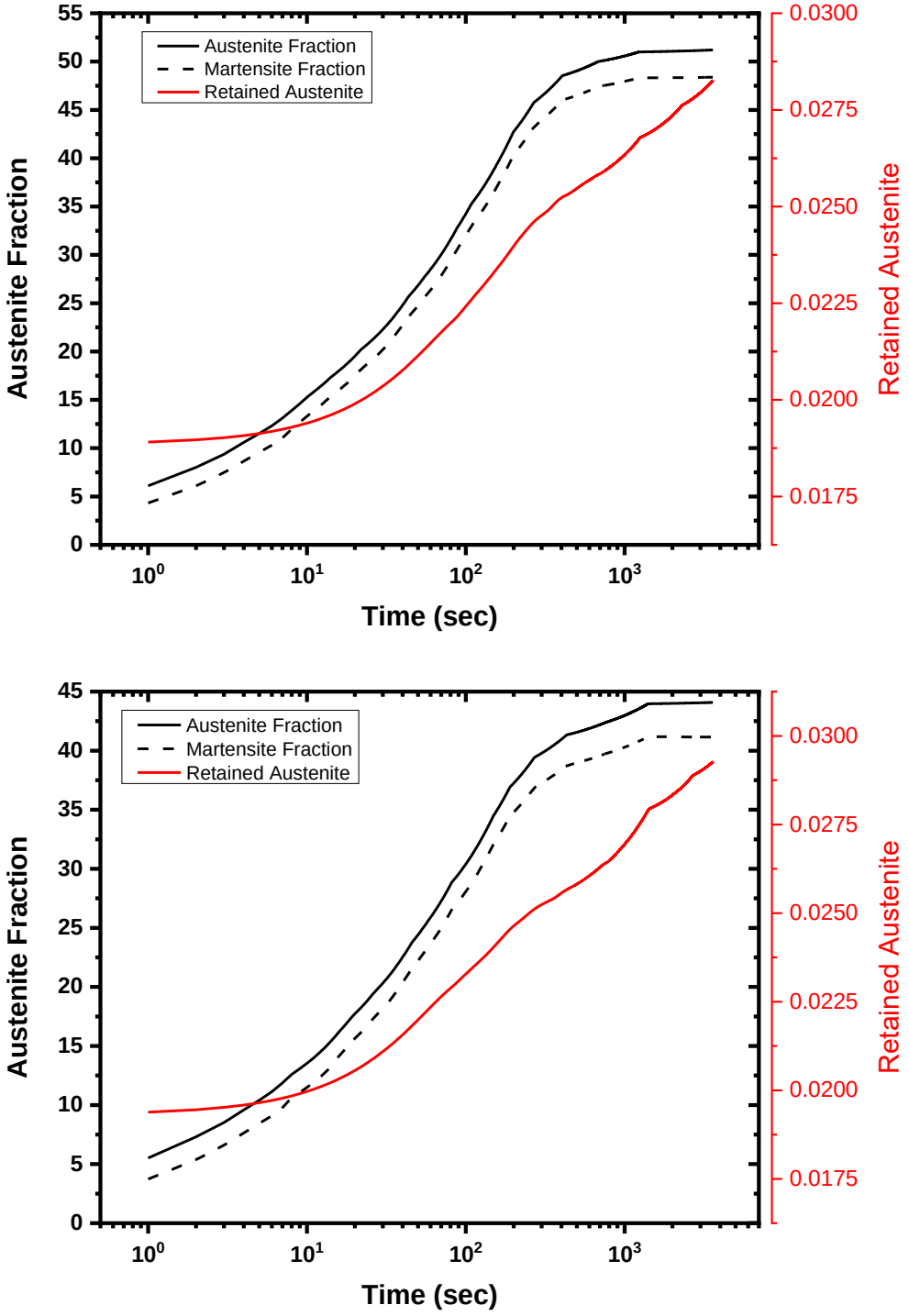

Figure 5.70: The volume fraction of austenite and martensite (black lines) and the volume fraction of retained austenite (red line) for IA at 760°C (a) and 750°C (b),for 3600sec.

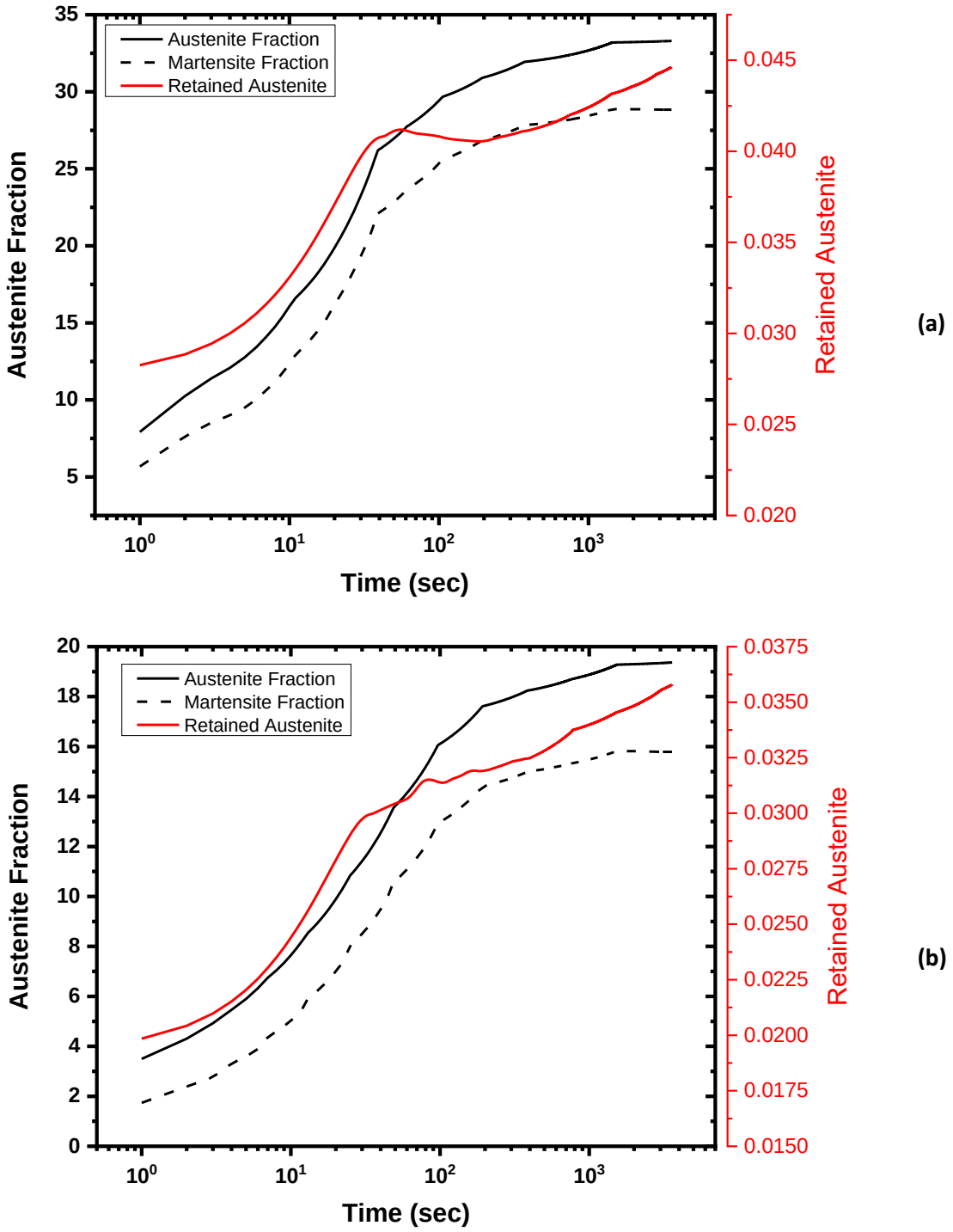

Figure 5.71: The volume fraction of austenite and martensite (black lines) and the volume fraction of retained austenite (red line) for IA at 720°C (a), 700°C (b), for 3600sec.

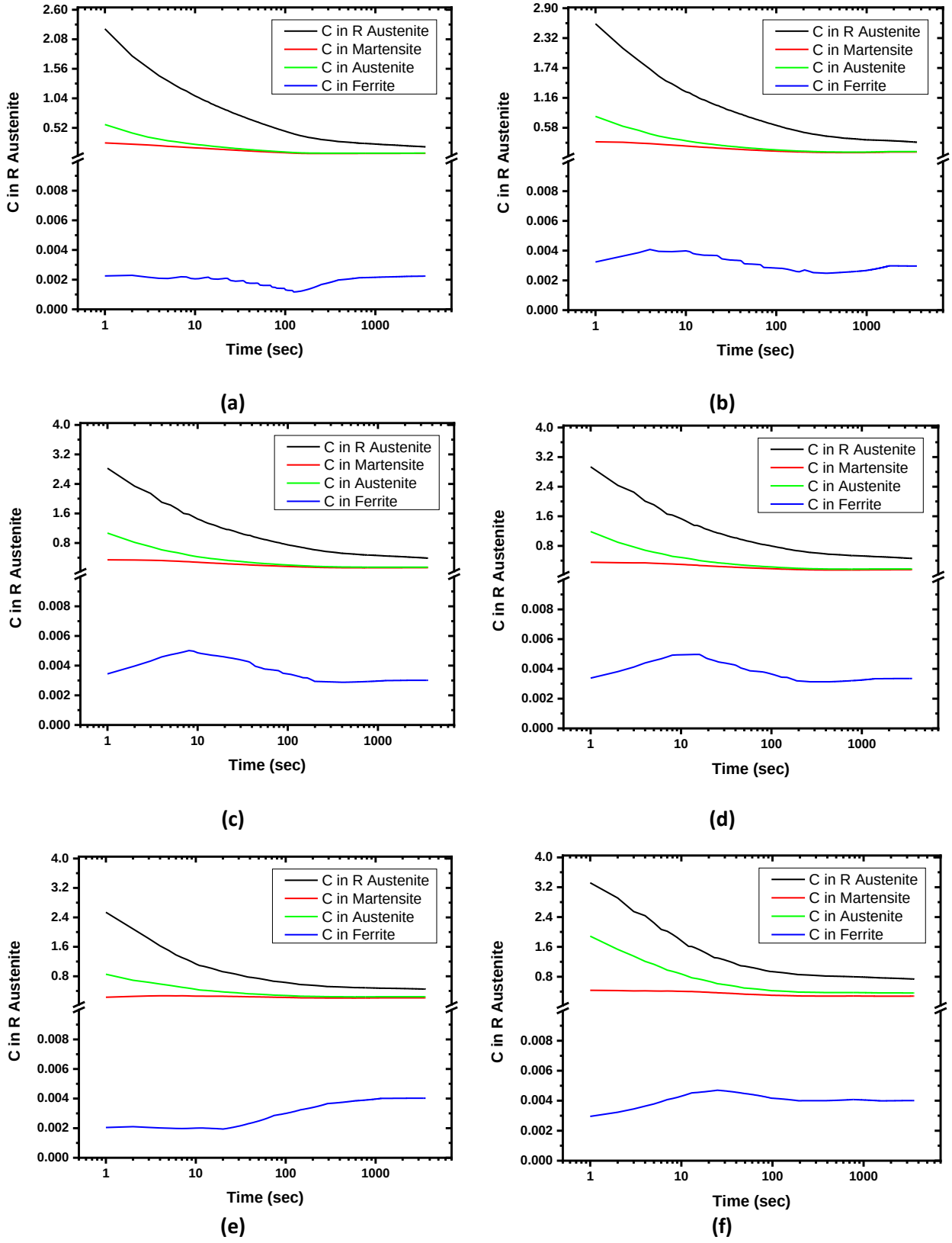

Figure 5.72: Carbon content in martensite (red line), austenite (green line), retained austenite(black line) and ferrite(blue line) for 3600sec with respect to IA time for IA at 800 °C (a), for IA at 780 °C (b), for IA at 760 °C (c), for IA at 750 °C (d), for IA at 720°C (e) and for IA at 700°C (f).

5.1.3 Results for Mapping of 2nd Model ($\gamma_{\gamma+cem}$-α Model)

Like in the 1st Model (γ-α Model), in the 2nd Model ($\gamma_{\gamma+cem}$-α Model) several maps are also illustrated bellow in order to connect the results that emerged from the simulation with the procedure for the process design. These maps show the effect of IA temperature and time on martensite's volume fraction, on the volume fraction of Mn (manganese), C (carbon), Si (silicon) and retained austenite after quenching from the IA temperature as well as the volume fraction of austenite at the IA temperature.

Figure 5.73 depicts the volume fraction of austenite for six different temperatures compared with intercritical annealing (IA) holding time and intercritical annealing (IA) temperature before cooling. As it is expected, at higher IA temperatures more austenite is formed. Martensite's fraction after quenching is depicted on Figure 5.74. like austenite, martensite's volume fraction is increasing at higher temperatures. Also, according to Figure 5.74, as temperatures rises martensite formation is faster. Retained austenite is illustrated in Figure 5.75with respect to IA temperature and IA holding time. Figure 5.76depicts the content of carbon in martensite. In Figure 5.77, Figure 5.78, Figure 5.79 is illustrated the map of austenite, martensite and retained austenite after quenching respectively. All in respect with IA time and IA temperature. The next three figures (Figure 5.80, Figure 5.81 and Figure 5.82), depict the mapping of different alloying elements in martensite. Figure 5.80 depicts the mapping of carbon (C) content in martensite with respect to IA time and IA temperature, while the Figure 5.81 and Figure 5.82 the mapping of manganese (Mn) content and silicon (Si) content in martensite respectively. Black lines in Figure 5.83 represent the mapping of martensite and red lines the mapping of carbon (C) content in martensite. It is observed that as the martensite percentages increase, carbon content decreases.

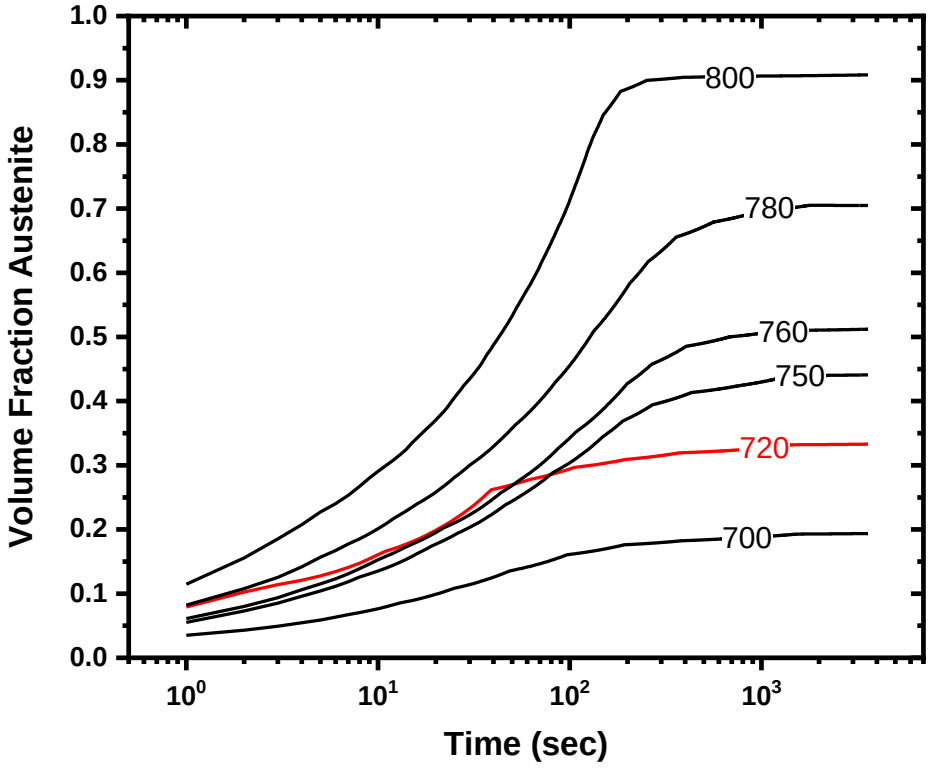

Figure 5.73: Volume fraction Austenite before cooling with respect to IA temperature and IA holding time.

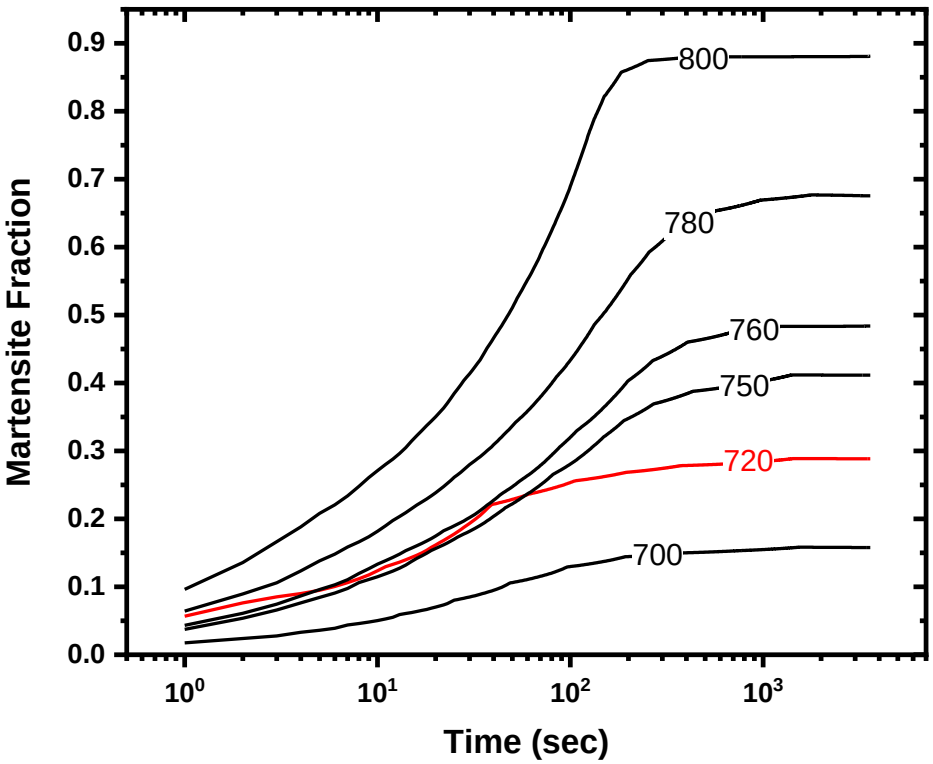

Figure 5.74: Volume fraction of martensite after quenching with respect to IA temperature and IA holding time.

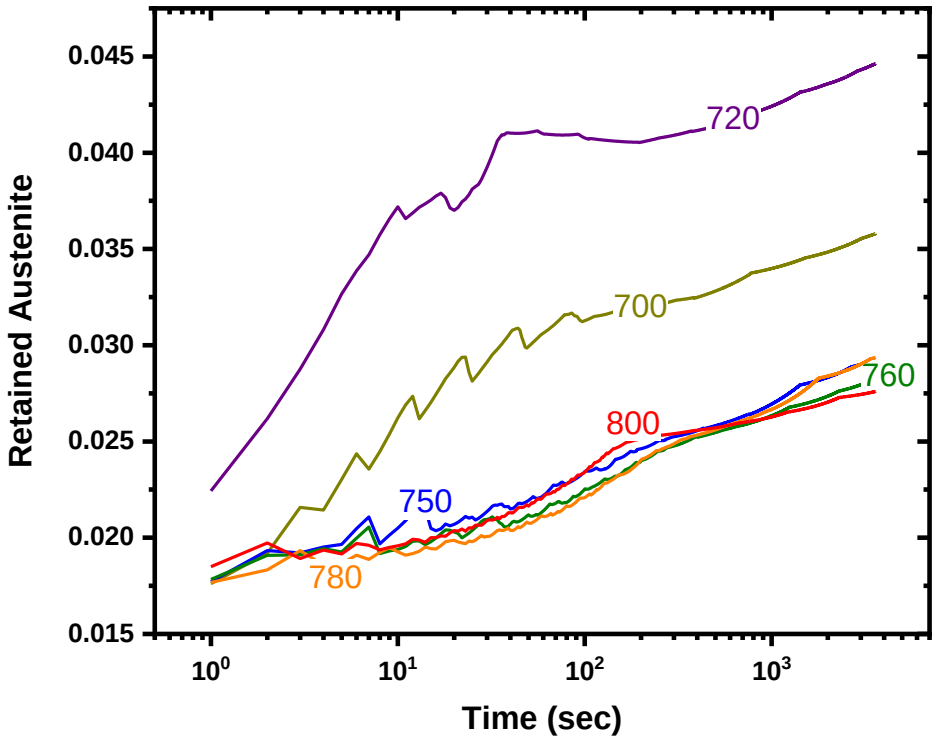

Figure 5.75: Volume fraction of Retained Austenite after quenching with respect to IA temperature and IA holding time.

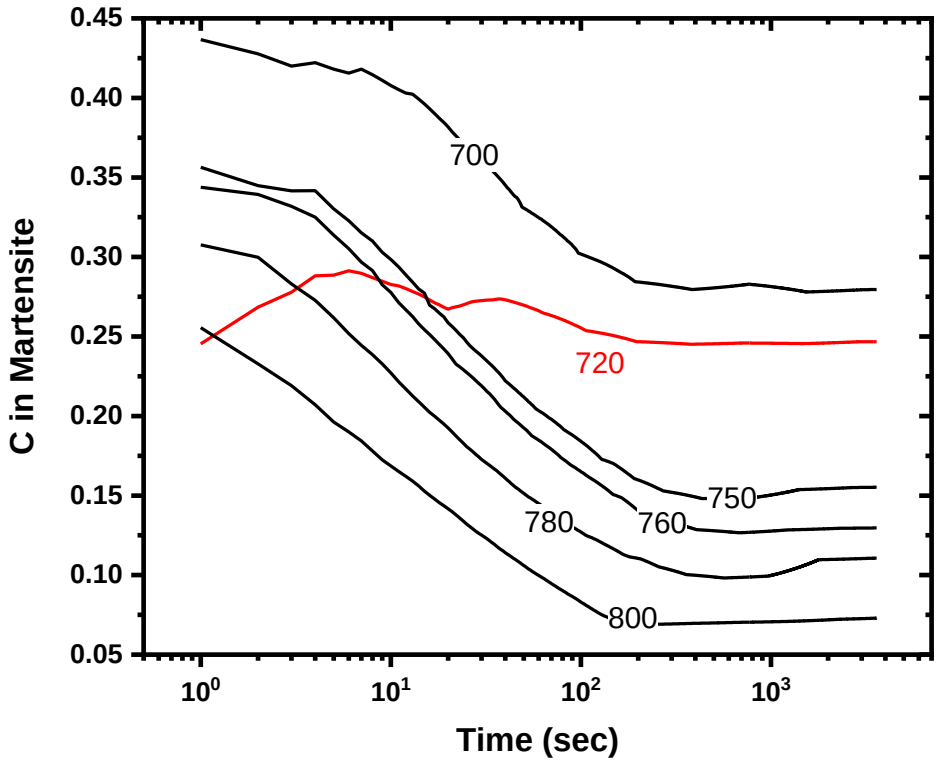

Figure 5.76: Carbon content in martensite with respect to IA time and IA temperature.

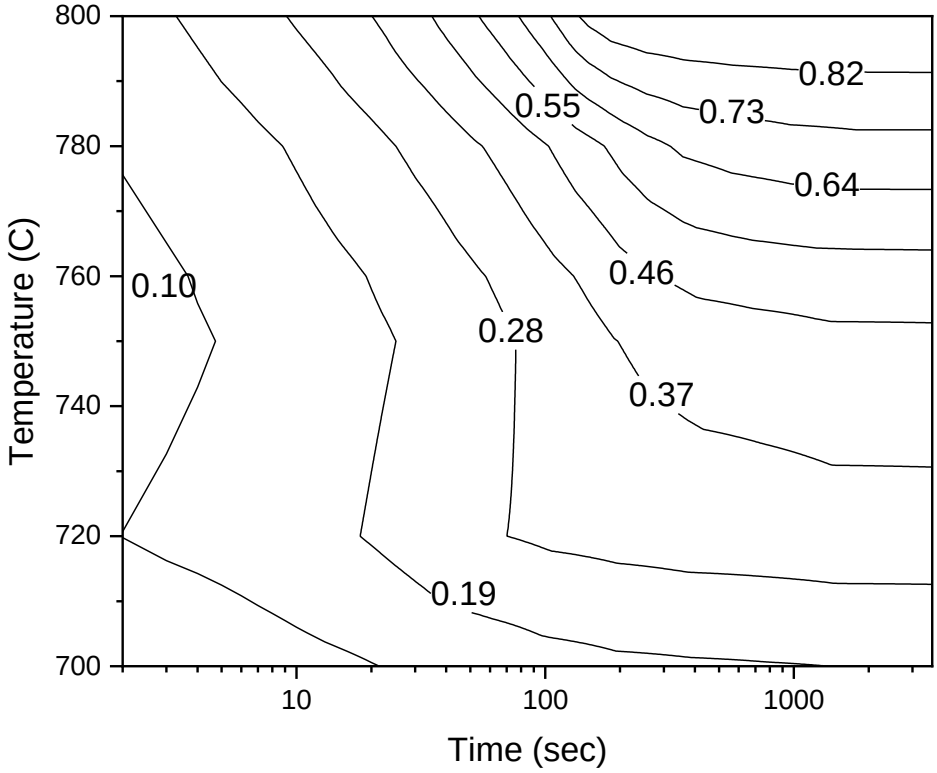

Figure 5.77: Mapping of Austenite volume fraction before cooling with respect to IA temperature and IA holding time

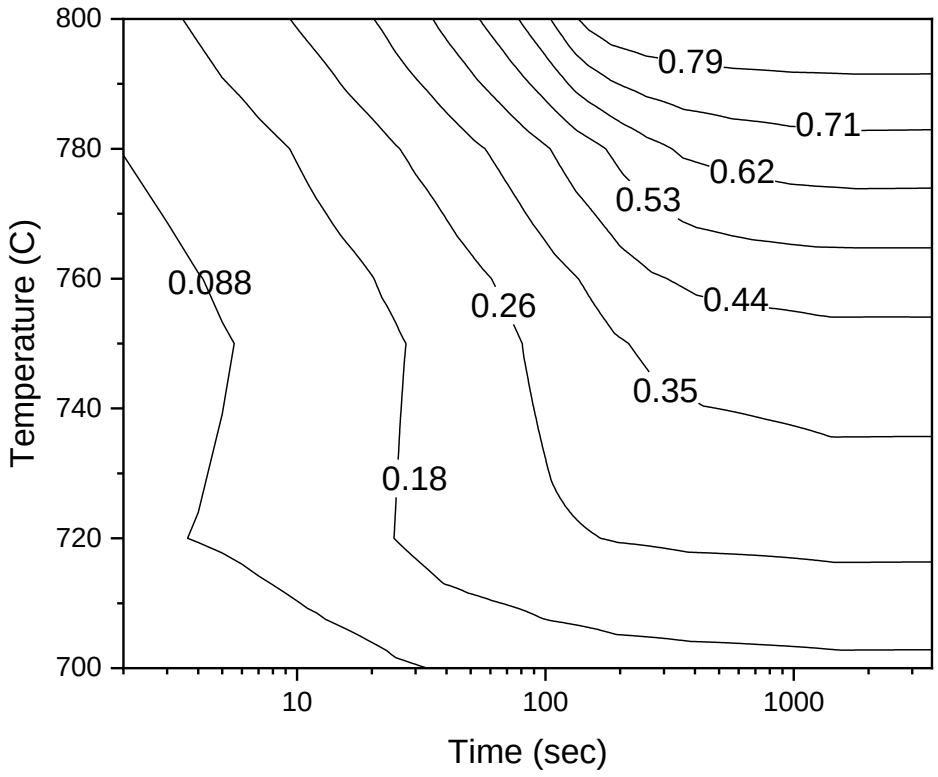

Figure 5.78: Mapping of martensite volume fraction after quenching with respect to IA temperature and IA holding time.

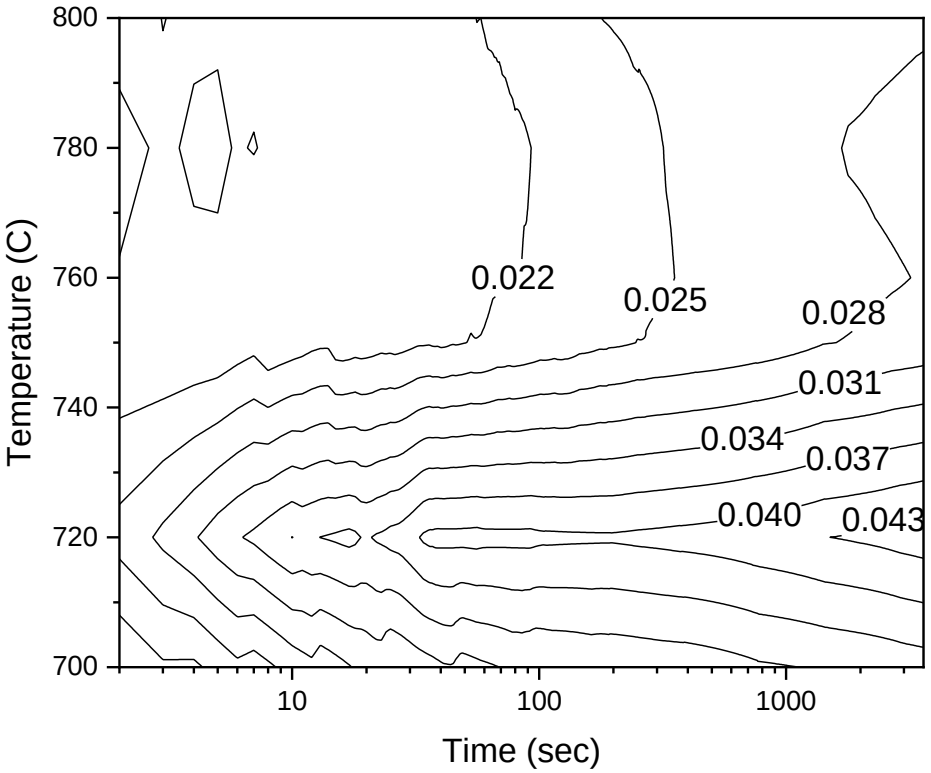

Figure 5.79: Mapping of Retained Austenite volume fraction after quenching with respect to IA temperature and IA holding time.

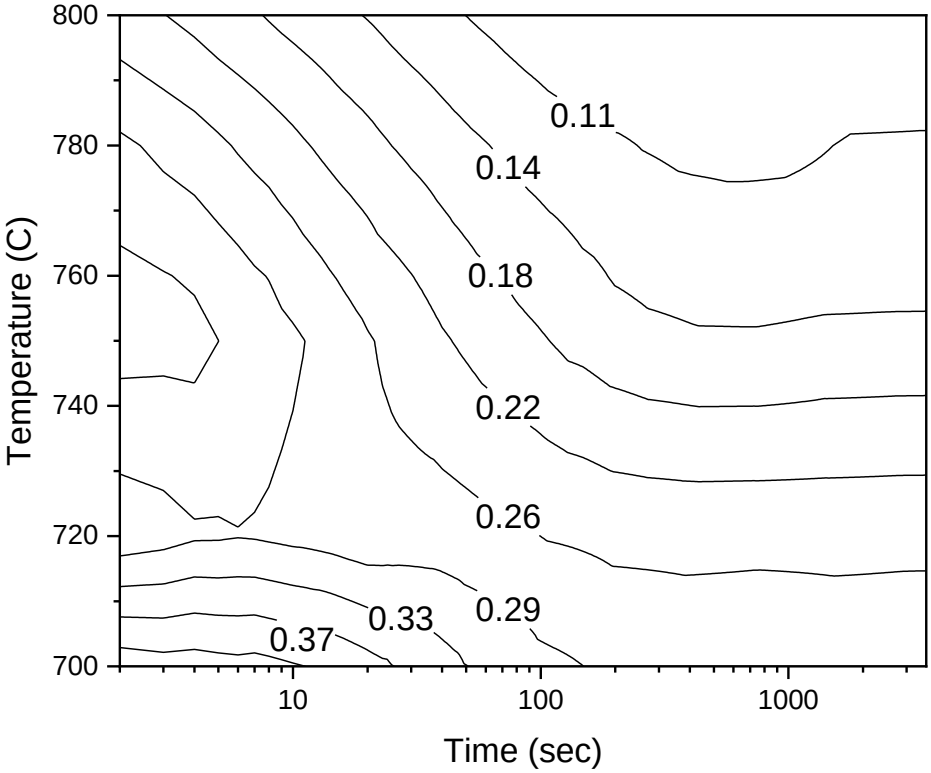

Figure 5.80: Mapping of carbon content in martensite with respect to IA time and IA temperature

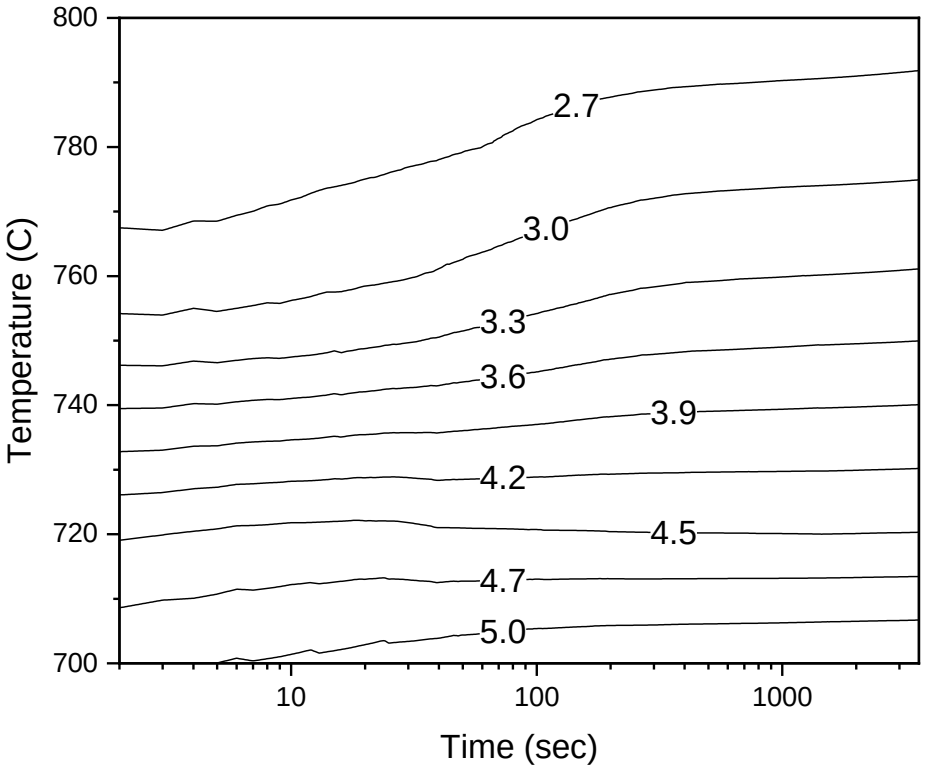

Figure 5.81: Mapping of Manganese content in martensite with respect to IA time and IA temperature

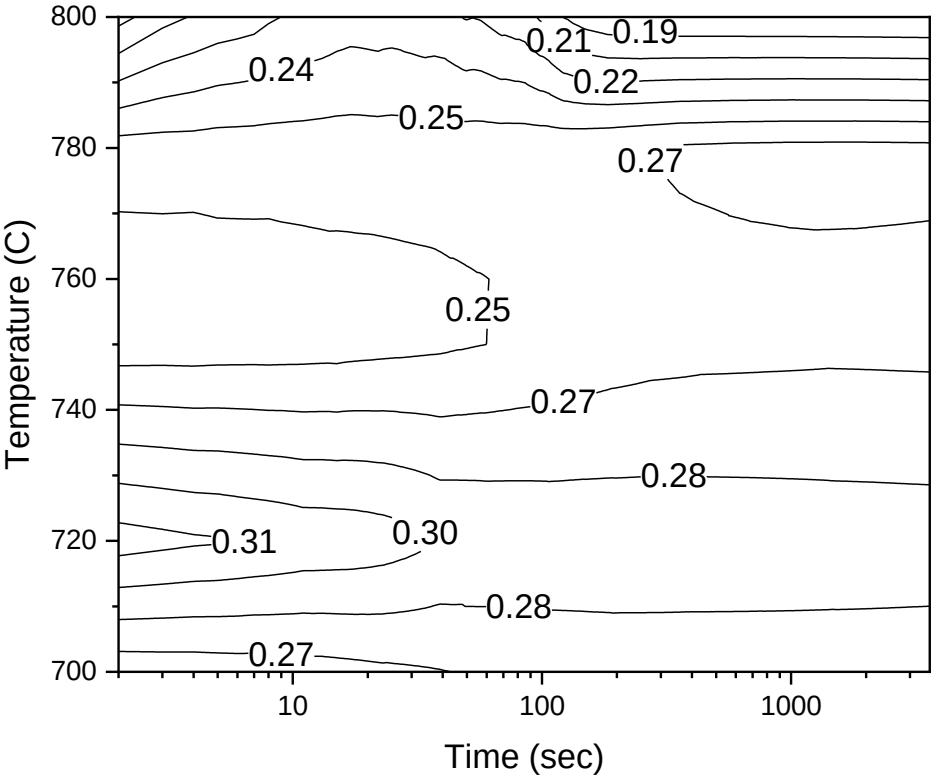

Figure 5.82: Mapping of Silicon content in martensite with respect to IA time and IA temperature

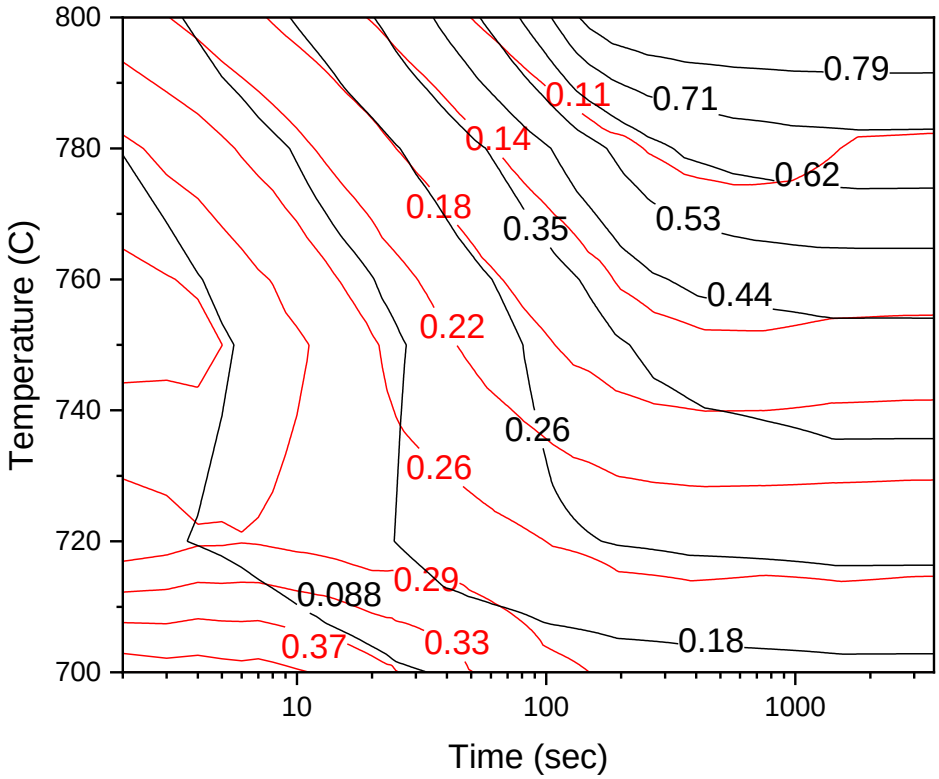

Figure 5.83: Mapping of martensite volume fraction (black lines) and carbon content in martensite (red lines) with respect to IA time and IA temperature for 3600 sec.

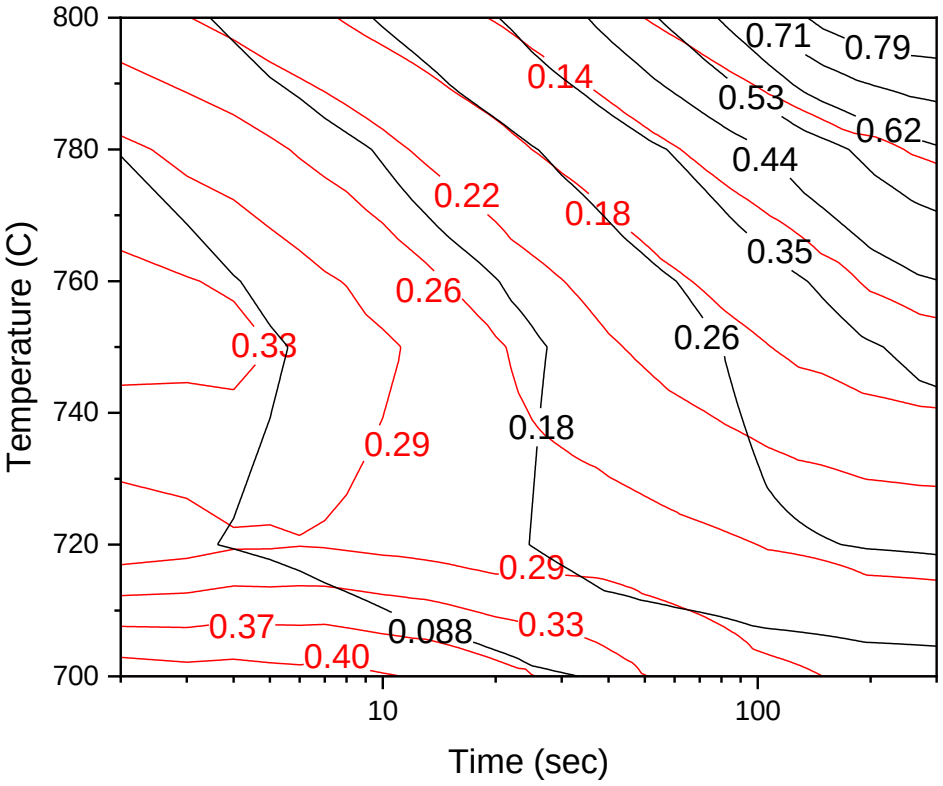

Figure 5.84: Mapping of martensite volume fraction (black lines) and carbon content in martensite (red lines) with respect to IA time and IA temperature for 300 sec.

Chapter 6 Conclusions

The key microstructural parameters, which determine the mechanical properties of DP steels are the martensite volume fraction and martensite hardness, which depends on its carbon content. Those parameters depend on the chemical composition of the steel and the processing parameters, the most important being the intercritical annealing (IA) temperature, time and heating rate to the IA temperature. The present work resulted in the following conclusions:

- Both models implemented in this work yielded very good results for high intercritical annealing temperatures, in relation to the experimental data.
- the 2nd Model ($\gamma_{\gamma+cem}$-α Model), due to the small percentage of initial austenite, resulted in good agreement between experimental and simulation results, not only for long times but also for times of less than 120 seconds.
- Higher intercritical annealing temperatures lead to higher austenite volume fraction and subsequently to higher martensite volume fraction.
- In the case of the 1st Model (γ-α Model) simulation, the volume fraction of retained austenite decreases with increasing IA holding time. On the other hand, for the 2nd Model ($\gamma_{\gamma+cem}$-α Model) simulation, the volume fraction of retained austenite increases with increasing IA holding time.
- The maps illustrated in Figure 5.42 and Figure 5.83 provide the martensite volume fraction and martensite carbon content as a function of IA annealing temperature, through which it is possible to select the appropriate processing variables in order to achieve the required microstructure (phase fractions) and strength (martensite carbon content). the maps presented in this work could serve as the first step towards the integrated process design of dual phase steels.

Chapter 7 References

1. Nanas, G.C., *Study of Intercritical Annealing of DP1000 Steel*, in *Department Of Mechanical Engineering*. 2019, University of Thessaly: Volos, Greece.

2. Bleck, W., S. Papaefthymiou, and A. Frehn, *Microstructure and Tensile Properties in Dual Phase and Trip Steels.* steel research international, 2004. **75**(11): p. 704-710.

3. Terada, D., et al., *Reason for high strength and good ductility in dual phase steels composed of soft ferrite and hard martensite.* IOP Conference Series: Materials Science and Engineering, 2017. **219**: p. 012008.

4. Peranio, N., et al., *Microstructure and texture evolution in dual-phase steels: Competition between recovery, recrystallization, and phase transformation.* Materials Science and Engineering: A, 2010. **527**(16-17): p. 4161-4168.

5. Peranio, N., F. Roters, and D. Raabe, *Microstructure Evolution during Recrystallization in Dual-Phase Steels.* Materials Science Forum, 2012. **715-716**: p. 13-22.

6. Azizi-Alizamini, H., M. Militzer, and W.J. Poole, *A novel technique for developing bimodal grain size distributions in low carbon steels.* Scripta Materialia, 2007. **57**(12): p. 1065-1068.

7. Azizi-Alizamini, H., M. Militzer, and W.J. Poole, *Austenite Formation in Plain Low-Carbon Steels.* Metallurgical and Materials Transactions A, 2010. **42**(6): p. 1544-1557.

8. Azizi-Alizamini, H., M. Militzer, and W.J. Poole, *Formation of Ultrafine Grained Dual Phase Steels through Rapid Heating.* ISIJ International, 2011. **51**(6): p. 958-964.

9. Yang, D.Z., et al., *Ferrite recrystallization and austenite formation in cold-rolled intercritically annealed steel.* Metallurgical Transactions A, 1985. **16**(8): p. 1385-1392.

10. Bos, C., M.G. Mecozzi, and J. Sietsma, *A microstructure model for recrystallisation and phase transformation during the dual-phase steel annealing cycle.* Computational Materials Science, 2010. **48**(3): p. 692-699.

11. Bos, C., et al., *Application of a Three-Dimensional Microstructure Evolution Model to Identify Key Process Settings for the Production of Dual-Phase Steels.* Metallurgical and Materials Transactions A, 2011. **42**(12): p. 3602-3610.

12. Rudnizki, J., et al., *Phase-Field Modeling of Austenite Formation from a Ferrite plus Pearlite Microstructure during Annealing of Cold-Rolled Dual-Phase Steel.* Metallurgical and Materials Transactions A, 2011. **42**(8): p. 2516-2525.

13. Huang, J., W.J. Poole, and M. Militzer, *Austenite formation during intercritical annealing.* Metallurgical and Materials Transactions A, 2004. **35**(11): p. 3363-3375.

14. Li, S.-c., et al., *Austenite formation during intercritical annealing in C-Mn cold-rolled dual phase steel.* Journal of Central South University, 2015. **22**(4): p. 1203-1211.

15. Suh, D.-W., *Dilatometric Analysis of Austenite Formation during Intercritical Annealing.* Metals and Materials International, 2008. **14**(3): p. 275-282.

16. Jeong, W.C. and C.H. Kim, *Formation of austenite from a ferrite-pearlite microstructure during intercritical annealing.* Journal of Materials Science, 1985. **20**(12): p. 4392-4398.

17. Okuda, K., et al., *Preliminary Simulation for Competing Behaviors between Recrystallization and Transformation in Dual Phase Steels.* Materials Science Forum, 2007. **558-559**: p. 1145-1150.

18. Krauss, G., *Heat Treated Martensitic Steels: Microstructural Systems for Advanced Manufacture.* ISIJ International, 1995. **35**(4): p. 349-359.

19. Waterschoot, T., K. Verbeken, and B.C. De Cooman, *Tempering Kinetics of the Martensitic Phase in DP Steel.* ISIJ International, 2006. **46**(1): p. 138-146.

20. Jiang, Z., Z. Guan, and J. Lian, *Effects of microstructural variables on the deformation behaviour of dual-phase steel.* Materials Science and Engineering: A, 1995. **190**(1-2): p. 55-64.

21. Kim, S. and S. Lee, *Effects of martensite morphology and volume fraction on quasi-static and dynamic deformation behavior of dual-phase steels.* Metallurgical and Materials Transactions A, 2000. **31**(7): p. 1753-1760.

22. Speich, G.R., V.A. Demarest, and R.L. Miller, *Formation of Austenite During Intercritical Annealing of Dual-Phase Steels.* Metallurgical and Materials Transactions A, 1981. **12**(8): p. 1419-1428.

23. Krielaart, G.P., J. Sietsma, and S. van der Zwaag, *Ferrite formation in Fe-C alloys during austenite decomposition under non-equilibrium interface conditions.* Materials Science and Engineering: A, 1997. **237**(2): p. 216-223.

24. Zheng, C. and D. Raabe, *Interaction between recrystallization and phase transformation during intercritical annealing in a cold-rolled dual-phase steel: A cellular automaton model.* Acta Materialia, 2013. **61**(14): p. 5504-5517.

25. Raabe, D., *Multiscale recrystallization models for the prediction of crystallographic textures with respect to process simulation.* The Journal of Strain Analysis for Engineering Design, 2007. **42**(4): p. 253-268.

26. Zhu, B. and M. Militzer, *Phase-Field Modeling for Intercritical Annealing of a Dual-Phase Steel.* Metallurgical and Materials Transactions A, 2014. **46**(3): p. 1073-1084.

27. Li, X., et al., *The effect of manganese content on mechanical properties of high titanium microalloyed steels.* Materials Science and Engineering: A, 2016. **677**: p. 340-348.

28. Drumond, J., et al., *Effect of Silicon Content on the Microstructure and Mechanical Properties of Dual-Phase Steels.* Metallography, Microstructure, and Analysis, 2012. **1**(5): p. 217-223.

29. Toolkit for the design of damage tolerant microstructures, *Research Programme of the Research Fund for Coal and Steel, Grant Agreement Number: 709711,.* 2016.

30. Suwanpinij, P., *Multi-scale Modelling of Hot Rolled Dual-phase Steels for Process Design*. 2012, RWTH: Aachen.

31. Bocharova, E., et al., *Dual-phase steel, flat product made of such dual-phase steel and method for manufacturing a flat product* E.P. Office, Editor. 2007: Germany.

32. Haidemenopoulos, G.N., *Physical metallurgy: principles and design*. 2018, Boca Raton: CRC Press, Taylor & Francis Group.

33. Andersson, J.O., et al., *Thermo-Calc & DICTRA, computational tools for materials science.* Calphad, 2002. **26**(2): p. 273-312.

34. Barbier, D., *Extension of the Martensite Transformation Temperature Relation to Larger Alloying Elements and Contents.* Advanced Engineering Materials, 2014. **16**(1): p. 122-127.

35. Koistinen, D.P. and R.E. Marburger, *A general equation prescribing the extent of the austenite-martensite transformation in pure iron-carbon alloys and plain carbon steels.* Acta Metallurgica, 1959. **7**(1): p. 59-60.